Identifying the Origins of Bone Loss Induced by Transient Muscle Paralysis Using Novel MicroCT Image Registration Techniques

Brandon James Ausk

A dissertation
submitted in partial fulfillment of the
requirements for the degree of

Doctor of Philosophy

University of Washington

2013

Reading Committee:
Ted S. Gross, Chair
Cecilia M. Giachelli
Marta Scatena

Program Authorized to Offer Degree:
Department of Bioengineering

University of Washington

Abstract

Identifying the Origins of Bone Loss Induced by Transient Muscle Paralysis
Using Novel MicroCT Image Registration Techniques

Chair of the Supervisory Committee:
Ted S. Gross, Ph.D.
Professor in the Department of Orthopaedics and Sports Medicine
Adjunct Professor in the Department of Bioengineering

The co-dependency of bone and muscle is exemplified by concomitant catabolic and/or anabolic tissue adaptations, as induced by respective decreases or increases in mechanical loading. Given that muscular contraction is responsible for skeletal loading during normal locomotion, this co-dependency has been attributed to an indirect consequence of muscle function. However, recent data from our group and others now indicate that direct communication between muscles, nerves and bone can significantly alter bone homeostasis independent of mechanical loading. In this dissertation, three independent studies explored the relation between impaired muscle function and bone homeostasis using our murine model in which rapid and profound bone loss is induced in the tibia following transient paralysis of the calf muscles. In the first study, we quantified endocortical expansion in the tibial diaphysis following transient muscle paralysis using a novel μCT image registration approach. This approach identified a complex, but highly repeatable, resorptive response implicating osteoclast recruitment and focal activation of osteoclastic resorption underlies the spatially consistent endocortical resorption induced by transient muscle paralysis. Importantly, this study also validated the use of serial μCT image registration to track focal bone alterations. In the second

study, we characterized the spatiotemporal parameters of bone resorption in our model, which revealed that tibia metaphyseal and diaphyseal bone loss induced by transient calf paralysis are spatially and temporally discrete events. By expanding our image registration approach, we determined that the initiating event in acute bone loss (within 3 days of paralysis) occurs in the proximal tibia metaphysis as a result of enhanced activity of resident osteoclasts adjacent to the growth plate. In contrast to the focal activation of osteoclasts in the proximal metaphysis, bone loss occurs throughout the diaphysis between 6 and 13 days post-paralysis; an observation that is temporally consistent with *de novo* osteoclastogenesis as a mediator of the diaphyseal resorption. These findings clarified the timing and origins of discrete resorptive events and allowed for investigation of the upstream cellular mechanisms responsible for their initiation. In the final study, we sought to determine if bone loss induced by transient muscle paralysis is a result of neurogenic inflammation of the bone marrow, which leads to enhanced osteoclastogenesis. Though attempts to suppress inflammatory mechanisms were unable to block bone loss following paralysis, we were able to demonstrate that inflammatory cell infiltration, pro-osteoclastogenic inflammatory gene expression and an alterations in bone marrow osteoclastogenic permissiveness occurred in a manner temporally consistent with observed bone loss. Further, we identified giant osteoclast formation, implicating enhanced osteoclast fusion as a potential mechanism for the extensive bone resorption. Taken together, these studies defined the spatiotemporal origins and potential mechanisms (enhanced osteoclast function in the metaphysis and *de novo* giant cell osteoclastogenesis in the diaphysis) of bone loss following transient muscle paralysis. More broadly, by characterizing the rapid and spatially distinct bone loss precipitated by transient muscle paralysis, we have provided evidence that muscle and bone

are directly coupled and that altered muscle function can activate cellular events that profoundly alter bone homeostasis.

Acknowledgement

This dissertation was made possible by the vast generosity that others have shown me over the past five years. I am incredible blessed to have been surrounded by such great colleagues, friends and family during this time and would like to take this space to thank those who have inspired and assisted me during this process.

First, and foremost, I need to thank everyone at the Orthopaedic Science Laboratories. I am not sure I would have been able to do this without you, but I am positive I would not have wanted to. Each and every one of you has shared your time and expertise with me in a way that I can only hope to one-day repay. DeWayne, Edith, Leah, Ron, Sandy, Steve, and Sundar, thanks for your patience, your assistance and all the laughs we have had along the way. I want to specifically thank Phil Huber for being my coconspirator in getting the image registration up and running. Your help was invaluable. I couldn't think of a better place to come to work, which is probably why you can't seem to get rid of me.

To my advisor and friend, Ted Gross, I owe my deepest gratitude. Thank you for your persistence in talking me into getting my PhD. Though I am sure it was lost on me during the process, this has been an incredibly important growing experience for me in so many ways and I'm very glad I was given this opportunity. I cherish all the conversations that this experience has afforded us, scientific and otherwise. Thank you!

To my committee, Cecilia Giachelli, Marta Scatena and Daniel Campbell, thank you all for your time and guidance. Each and every one of you has your fingerprints on this work and because of that it is so much better than I could have hoped for.

Most importantly, I need to thank my family. To my children, Perrie and Isaac, you truly are my inspiration each and every day. You two are, and always will be, my greatest

accomplishment. I could not be more proud to be your father. My sincere hope is that you will stumble upon this document many years from now and it will remind you just how much I love you both. And to my wife, Karlee, this dissertation has only been made possible through your selflessness and support. Thank you for sharing your life with me. I love you and I hope I have made you proud.

Table of Contents

List of Figures

List of Tables

List of Abbreviations

BMU: Bone multicellular unit

BTxA: Botulinum neurotoxin A (or Botox)

BRR: Bone resorption rate

BRR_{BS}: Bone resorption rate normalized to initial bone surface

BRR_{BV}: Bone resorption rate normalized to initial bone volume

BS: Bone surface

BV: Bone volume

BV/TV: Bone volume fraction

CD: Cluster of differentiation

Ct.Ar: Cortical area

Ct.Vol: Cortical volume

DC-STAMP: Dendritic cell-specific transmembrane protein

e.MS: Endocortical mineralizing surface

Ec.Ar: Endocortical area

Ec.Vol: Endocortical volume

FACS: Fluorescence activated cell sorting

HA: Hydroxyapatite

HPRT: Hypoxanthine-guanine phosphoribosyltransferase

IL: Interleukin

IRV: Image registration volume

kVp: Peak kilovoltage

MAPE: Mean absolute percent error

M-CSF: Macrophage-colony stimulating factor

OC-STAMP: Osteoclast stimulatory transmembrane protein

OPC: Osteoclast precursor cells

OPG: Osteoprotegerin

OVX: Ovariectomized

PDB: Paget's disease of bone

Ps.Ar: Periosteal area

Ps.Vol: Periosteal volume

RANK: Receptor activator of nuclear factor kappa-B

RANKL: Receptor activator of nuclear factor kappa-B ligand

ROI: Region of interest

Tb.N: Trabecular number

Tb.Sp: Trabecular spacing or separation

Tb.Th: Trabecular thickness

TCR: T cell receptor

TNF or **TNFα**: Tumor necrosis factor alpha

TRAP: Tartrate-resistant acid phosphatase

TV: Total volume

µA: Microamps

µCT: Micro-computed tomography

Chapter 1: Introduction

1.1 Bone Physiology and Osteopenia

Bone, the osseous tissue that comprises the skeleton, serves three primary functions. The first is as a metabolic reserve for essential ions such as calcium and phosphate. Bone also functions as a protective tissue for internal organs (e.g., the ribs and skull) and marrow cavities vital for hematopoiesis (e.g., femur and tibia). Finally, the skeleton provides mechanical functionality, allowing not only structural support of body mass, but also muscular connections needed for rigid body motion. This mechanical function of the long bones of the appendicular skeleton (specifically the tibia), and more explicitly its altered interaction with adjacent muscles, makes up the thrust of this dissertation.

Like most long bones, the tibia is composed mainly of two distinct skeletal tissues (Fig. 1.1). Cortical bone (or compact bone) is a densely calcified tissue that makes up the shell (i.e., cortex) of the tibia. For this reason, cortical bone acts as the structural framework of the skeleton, as well as a protective envelope for bone marrow housed within the medullary cavity. Trabecular (or cancellous or spongy) bone, generally found in regions near the articular surface, consists of thin plate and rod like structures. Compared with cortical bone, trabecular bone is a highly vascularized and innervated tissue that is generally surrounded by bone marrow. Trabecular bone is much less dense with a higher surface to volume ratio than cortical bone. It is for this reason that trabecular bone mainly functions as a highly responsive metabolic reserve, and not a structural material.

Both trabecular and cortical bone tissues possess the ability to actively adapt to a number of exogenous and endogenous stimuli [1-4]. The most well know example of this was observed as far back as 1870 in a work published by Julius Wolff that is known today as *Wolff's Law of*

Functional Adaptation [5]. Simply put, Wolff's Law states that the structure of bone (both trabecular and cortical) will adapt to meet its functional demands while also minimizing its mass. For instance, an increase in skeletal loads through exercise will induce bone formation, while a decrease in habitual loads is known to result in bone resorption. For this reason a sedentary lifestyle of elderly is often of concern in leading to their increased rates of osteopenia (i.e., low bone mineral density) and the resulting increased risk of fracture and mortality [6, 7].

However, many other factors can lead to, or exacerbate, an osteopenic phenotype. Estrogen deficiency in women and testosterone deficiency in men, which commonly occurs with aging, is known to have a detrimental effect on bone mass [8, 9]. Hyperparathyroidism is another hormone imbalance known to weaken the structural integrity of bone [10]. Exogenous factors such a diet (e.g., lack of calcium and/or vitamin D) and smoking can also affect bone mineral density [11-13]. More recently, many inflammatory conditions have been connected to low bone mass phenotypes [14-16]. This has led to the emerging field of Osteoimmunology in which the concurrent control of immune responses and bone metabolism is investigated.

No matter the cause, osteopenia results from an imbalance of activity between the two bone cells responsible for the structural and morphological characteristics of bone tissues, osteoblasts and osteoclasts. The bone forming cells, osteoblasts, are mononucleated cells from the mesenchymal stem cell lineage. Osteoblasts form new bone tissue through the secretion and mineralization of osteoid, an unmineralized bone matrix formed primarily of type 1 collagen. Opposing this action, osteoclasts are the cells responsible for resorbing bone tissue. From the hematopoietic cell linage, osteoclasts are multinucleated members of the monocyte/macrophage family that resorb existing bone tissue through enzymatic reactions. The actions of osteoclasts are often functionally coupled with the action of osteoblasts in what is known as a bone

multicellular unit (BMU) in a process known as bone remodeling. In a BMU, osteoclasts first remove old bone tissue and are closely followed by osteoblasts forming new bone tissue. Not only does this process help maintain the structural integrity of bone through the removal of minor defects, but also bone mass homeostasis as well. However, it is the imbalance in the individual actions of these cell types that lead to osteoporotic bone phenotypes. Germane to this dissertation, this imbalance is often caused by RANKL mediated increases in both osteoclast formation (osteoclastogenesis) and function outpacing normal osteoblastic bone formation.

1.2 Osteoclastogenesis and RANKL

Osteoclasts are specialized bone resorbing cells formed by fusion of monocytic/macrophage precursors. Monocytes and macrophages are abundant in bone marrow and are guided to differentiate into osteoclast precursor cells (OPC) through signaling of macrophage-colony stimulating factor (M-CSF), an essential cytokine of osteoclastogenesis [17]. M-CSF controls OPC survival and proliferation as well [18, 19]. OPCs fuse together to form multinucleated osteoclastic cells; a process controlled by the master osteoclast fusogen dendritic cell-specific transmembrane protein (DC-STAMP) [20]. DC-STAMP is expressed in high levels on both OPCs and osteoclasts [20, 21]. Finally, multinucleated osteoclasts attach to bone surface and begin resorbing bone tissue through enzymatic degradation of bone mineral. At this point, osteoclasts are known as 'active osteoclasts.' The induction of osteoclast fusion and activation is regulated by the second of two essential osteoclastogenic cytokines, Receptor Activator for Nuclear Factor κ B Ligand (RANKL) (Fig. 1.2).

RANKL, a member of the Tumor Necrosis Factor (TNF) superfamily [22, 23], is a potent and necessary cytokine for osteoclastogenesis [24, 25]. Specifically, RANKL facilitates

differentiation of osteoclast precursors into active osteoclasts. This is accomplished through RANKL binding to RANK receptors on osteoclast precursors, resulting in a signaling cascade that leads to increased levels of intracellular C-Fos expression and ultimately triggers the transcription of osteoclastogenic genes [26]. RANKL induced osteoclastogenesis is inhibited by Osteoprotegerin (OPG), a RANK homolog [25, 27]. OPG binds to RANKL with high affinity and blocks its ability to initiate osteoclastogenesis (Fig. 1.2). For this reason, RANKL/OPG ratio is a main correlate of bone mass [28, 29]. Additionally, it has been shown that cytokines that up-regulate RANKL production tend to down-regulate OPG production, in turn amplifying the RANKL induced osteoclastogenic pathway [30, 31].

Not surprisingly given the mechanism of action, RANKL has been shown to play an important role in maintaining normal bone homeostasis. A disruption of RANKL signaling in mice causes severe osteopetrosis resulting from a complete lack of osteoclasts [32, 33]. Conversely, mice lacking OPG suppression of RANKL signaling have severe osteoporosis due to unmitigated osteoclastogenesis [34, 35]. More recently, *in vitro* studies have determined that RANKL signaling is functionally different depending on whether it is in its membrane bound or soluble form. Membrane bound RANKL has been shown to be more efficient at increasing osteoclastogenesis than its soluble RANKL counterpart [30, 36, 37].

RANKL signaling from osteoblasts are commonly credited for controlling normal bone homeostatic levels through functionally coupling the BMU. However, RANKL is produced by a myriad of cells including many involved in the immune response (e.g., T cells and B cells, Fig. 1.2). As well, other inflammatory cytokines such as TNFα, IL-1, and IL-6 have been shown to regulate the production of RANKL and enhance its osteoclastogenic potential [28, 38-40]. At

present, immune cell control of bone resorption is most well characterized in T cell mediated osteoclastogenesis.

The ability of T cells to produce RANKL has led to examination of their role in many bone loss pathologies. For example, adjuvant-induced arthritis, a model of rheumatoid arthritis, induces severe inflammation within the bone marrow and soft tissues surrounding joints and is accompanied by local bone destruction [41]. Synovial T cells isolated at the clinical onset of arthritis have shown expression of surface bound RANKL [24]. Additionally, OPG treatment prevents the accumulation of osteoclasts and resulting bone loss seen in this model, suggesting that the induced bone destruction was RANKL mediated [24]. Bone loss induced by estrogen deficiency is also modulated through T cell signaling. Ovariectomy up-regulates T cell production of tumor necrosis factor alpha (TNFα) to levels that augment RANKL-induced osteoclastogenesis and may itself stimulate T cell RANKL production [42, 43]. Though many other inflammatory cells of been implicated in this process, these examples highlight how inflammatory alterations in RANKL signaling can lead to devastating bone loss pathologies and may also suggest a mechanism in which the profound RANKL-mediated bone loss is achieved in our model of transient muscle paralysis.

1.3 Transient Muscle Paralysis Induced Bone Loss

1.3.1 Model Origins

A common model system for studying the effects of disuse osteopenia in rodents is hindlimb unloading. In this model originally created by NASA, caged mice are suspended by their tail at an angle of approximately 30 degrees [44]. This results in functional gait unloading of both hindlimbs (analogous to what occurs to astronauts during microgravity). Though this

model has been used extensively to study the mechanoresponsiveness of bone tissue, challenges remain that limit its utility. For example, hindlimb suspension is known to induce cephalic fluid shifts, which may be causal to the increases observed in skull and mandible bone volumes [45]. Hindlimb suspended mice must also be housed individually, dramatically limiting the throughput and cost of this model. Most importantly, prolonged suspension can induce profound systemic stress responses in rodents as observed through an increase in glucocorticoid levels and adrenal mass of mice, as well as a decrease in body mass compared to ad libitum fed controls [46, 47]. Given that enhanced glucocorticoid production has been shown to have deleterious effects on bone in the absence of mechanical disuse, clarifying the role of disuse on bone loss in this model is difficult.

During the summer of 2004, Blaire Becker and David Sanford, then undergraduate summer students at the Orthopaedic Science Laboratories, conceptualized a disuse model that would minimize the confounding and restrictive factors of traditional hindlimb unloading. Their idea was to inject the extensor muscles in a single mouse hindlimb with the powerful paralytic agent, botulinum toxin A (BTxA or Botox). BTxA, the most acutely toxic substance known, is a purified protein produced by the bacterium *Clostridium botulinum*. When injected, BTxA enters the nerve terminal and paralyzes skeletal muscle by blocking acetylcholine release at the neuromuscular junction. The original expectation of this model was that the BTxA injected limb (right limb) would naturally tuck under the body, removing functional gait loading from that limb. However, observations during pilot studies showed mice with paralyzed right quadriceps and calf muscle groups were still able to lift and place the right foot while walking and partially bear body weight while standing and climbing [48]. As such, this model represented only a mild disuse of the right mouse hindlimb causing us to anticipate a modest level of bone resorption.

1.3.2 Time Course of Bone Loss Following Transient Muscle Paralysis

In an initial study in mice, transient muscle paralysis produced via intramuscular injection of BTxA (2 units/100g) into the quadriceps and calf muscles induced rapid and profound bone loss in the femur and tibia [48]. Following a series of pilot studies, BTxA dosing was modified to eliminate systemic weight loss in the mice, and in subsequent studies a single injection of BTxA (2U/100g) in the calf muscles was used and bone loss examined in the trabecular and cortical compartments of the adjacent tibia. We observed a greater than 75% degradation of trabecular bone volume in the proximal tibia metaphysis, as well as an 8.3% increase in endocortical bone volume at the tibia mid-diaphysis within 12 days [49]. The bone loss was achieved through profound endocortical osteoclastic resorption [48], with significant trabecular bone changes lasting more than 12 weeks beyond the initiation of transient muscle paralysis [50]. Recently, other groups have explored transient muscle paralysis induced bone loss in rats and rabbits with similar results [51, 52]. The profound and lasting bone loss in this model is surprising when considering that normal ambulation is recovered within three weeks of BTxA injection and the primary gait forces are not significantly altered [53]. Also, the acute and profound response in this model varies from other disuse models (e.g. hindlimb suspension, cast immobilization, etc.) where osteoclast-driven bone loss proceeds much less rapidly (Fig. 1.3) [54-56]. These results suggest muscle and bone interaction is more complex than the paradigm that muscle contraction induced mechanical loading is a determinant of bone homeostasis - rather the data suggests that muscle and bone interaction may involve direct signaling between the adjacent organs.

1.3.3 Muscle Paralysis Degrades Bone Via RANKL Mediated Osteoclastogenesis

Further follow-up experiments began to define how muscle paralysis induced bone loss was achieved. Transient muscle paralysis stimulates elevated levels of RANKL in the adjacent marrow within 7 days [57]. However, levels of OPG are minimally altered through 7 days suggesting osteoclastogenesis may be mediating muscle paralysis induced bone loss [57]. Supporting this finding, bone loss was found to be completely mitigated by both conditional deletion of Nuclear Factor of Activated T cells c1 (NFATc1) and systemic treatment with recombinant human Osteoprotegerin (hrOPG). As both these pathways block RANKL mediated osteoclastogenesis, these data confirm transient muscle paralysis induces rapid osteoclastogenesis via local RANKL signaling resulting in profound focal bone resorption [57].

Subsequent studies have identified a potentially important role for neuronal signaling in this pathway. Given that BTxA induces paralysis through blocking of acetylcholine release from motor nerves and that bone marrow environments are themselves highly innervated, we hypothesized that bone loss in our model may be a result of neuromuscular communication between adjacent bone and muscle organs. In this context, our findings that mice with hindlimb proprioceptive defects arising from muscle spindle agenesis have dramatically muted bone loss responses following muscle paralysis supported this hypothesis [58]. Besides blocking the RANKL mediated pathways, this proprioceptive defect model is the only other model to date in which we have been able to profoundly alter bone resorption following paralysis. This suggests that both neuronal and RANKL signaling are critical to the induction of bone loss following paralysis (Fig 1.4). Our ability to detect these profound focal bone alterations and efficiently test novel hypotheses within this model of transient muscle paralysis has been made possible by the recent commercial availability of high-resolution micro-computed tomography systems.

1.4 Micro-Computed Tomography (μCT) Assessment of Bone Microstructure

Until the recent past, bone phenotyping and quantitative assessment of bone morphologic alterations required laborious and costly histomorphometric analysis. For instance, to perform standard histomorphometric analysis, the study animal had to be sacrificed. This meant that each investigation timepoint required a separate group of mice, leading to extensive animal use. Additionally, assessment of bone microarchitecture was generally completed at a limited amount of 2D sections. To estimate bone's 3D properties, stereologic analysis was performed, requiring assumptions about the distribution of the microstructure under investigation. Given the expense and the inherent difficulty of traditional histomorphometric studies, high-resolution micro-computed tomography (μCT) has now become the standard imaging technique for assessing trabecular and cortical bone morphology *in vivo* and *ex vivo.*

The development of commercially available μCT imaging systems capable of small animal *in vivo* scanning has enabled precise and accurate quantification of bone alterations in a variety of *in vivo* models. In the simplest sense, μCT constructs a three-dimensional map of bone through obtaining numerous two-dimensional X-ray images of the volume of interest. With available resolution approaching one-tenth the width of mouse trabeculae, μCT analysis is perfectly suited for quantifying morphologic alterations in even the smallest rodent bone microstructures. Unlike traditional histomorphometric techniques, *in vivo* μCT scanners allow for multiple investigation timepoints within a single animal, thus limiting the amount of animals needed for a study. However, as μCT analysis is generally suited for gross measures of bone alterations (i.e., average changes that occur through a volume of interest), its current application lacks the ability to track the cell level dynamics that result in changes in bone phenotype

(currently still accomplished through standard histomorphometric analysis). One focus of this dissertation is to create techniques that would, for the first time, allow μCT-scanning studies to track focal osteoclastic resorption activity.

As μCT analysis has become the 'gold standard' for studying bone morphology, minimum guidelines for assessment of bone microstructure in rodents using μCT have been adopted [59]. Though much of μCT imaging is automated, user defined variables such as scan location, scanner settings and data thresholding can greatly affect the study outcomes. For this reason, these guidelines define standard μCT analysis, both pre and post data acquisition, required to interpret and compare findings across different studies. For maximum transparency in the μCT analysis performed herein, this dissertation has adopted these guidelines as a minimum framework for all μCT analysis performed.

1.5 Dissertation Design

Our initial investigation into bone loss induced by transient muscle paralysis identified bone resorption disproportional to the mild gait defect induced in this model. This counterintuitive result challenged our understanding of the mechanisms that control bone homeostasis. As bone loss in our model occurred exclusively within the medullary cavity of the affected tibia, we hypothesized that calf paralysis induces profound osteoclastic alterations in the tibia marrow. Three specific objectives were designed to address this overarching hypothesis. Our first objective was to quantify focal osteoclastic resorption following muscle paralysis. Once this was achieved, we next defined the spatiotemporal dynamics of bone resorption in our model. Finally, we leveraged the information contained within the spatiotemporal osteoclastic dynamics to identify and test biologic mechanism that control bone loss following transient muscle paralysis.

This dissertation contains three primary investigations, based on these objectives, which advance the understanding of the origins of bone loss induced by transient muscle paralysis (Fig 1.5). Chapter 2 was based upon a manuscript published in the journal *Bone* in which we describe the complex endocortical resorption pattern 21 days following muscle paralysis using a novel μCT image registration technique [60]. Chapter 3 contains another manuscript published in the journal *Bone* in which we performed multiple novel μCT imaging studies to identify the compartmental differences in bone loss following paralysis, including spatiotemporal tracking of bone resorption dynamics and trabecular image registration [61]. The findings within Chapters 2 and 3 informed a testable hypothesis explored in Chapter 4. Chapter 4 contains a manuscript in preparation in which we investigated whether bone loss induced by transient muscle paralysis is a result of inflammatory cell mediated alterations in the osteoclastogenic potential of bone marrow. Chapter 5 describes the overall conclusions of the investigations within this dissertation, as well as future work (both planned and in progress) that stem both from the direct findings of our research and the image registration techniques created to facilitate this investigation.

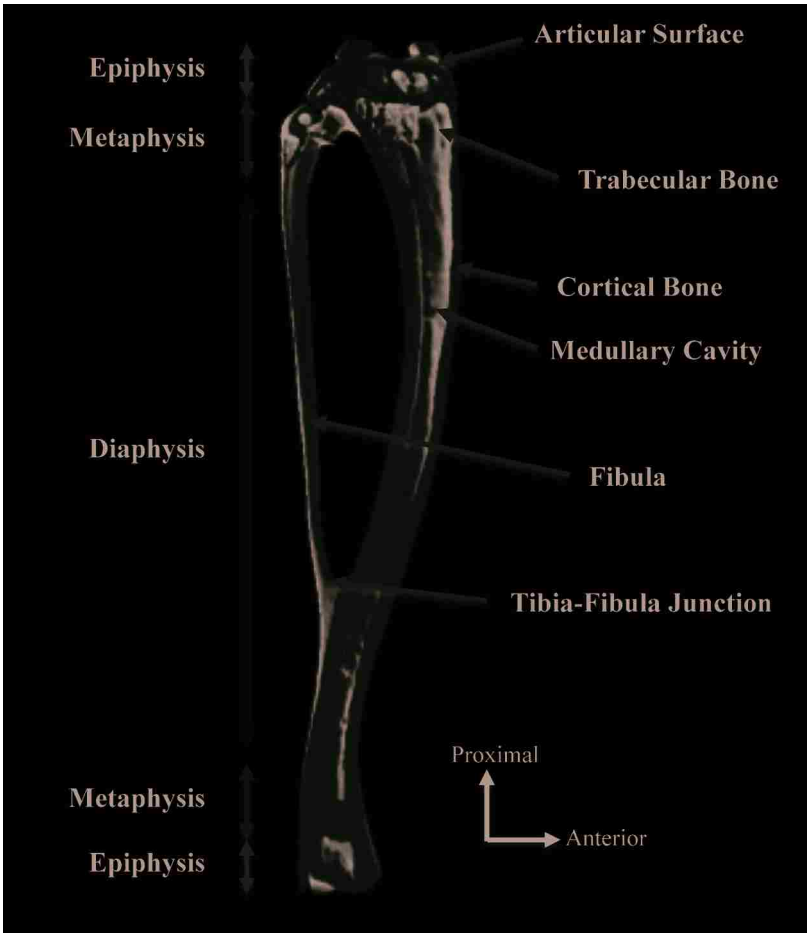

Figure 1.1: Anatomy of the Mouse Tibia
Sagittal μCT section of a mouse tibia (with fibula) highlighting the anatomy and bone structures. Throughout this dissertation, bone alterations were generally investigated in the trabecular bone compartment of the proximal tibia metaphysis and in the cortical bone compartment of the tibia mid-diaphysis.

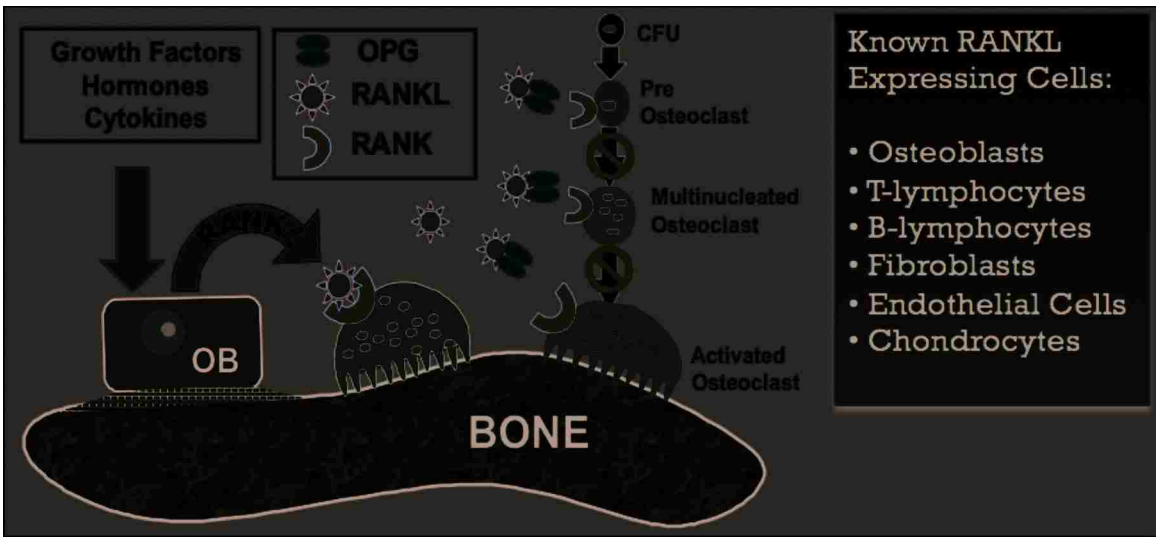

Figure 1.2: RANKL and Osteoclast Activation
Schematic of functional coupling of osteoclast and osteoblast activity through the RANK/RANKL/OPG pathway. RANKL expression controls fusion and activation of osteoclasts by binding to the RANK receptor on osteoclastic cells. This pathway is functionally blocked by OPG binding RANKL. Many cells types (right inset), other than osteoblasts, express RANKL and can lead to an imbalance of osteoclast activity. Original schematic courtesy of P. Kostenuik, Ph.D., Amgen Inc.

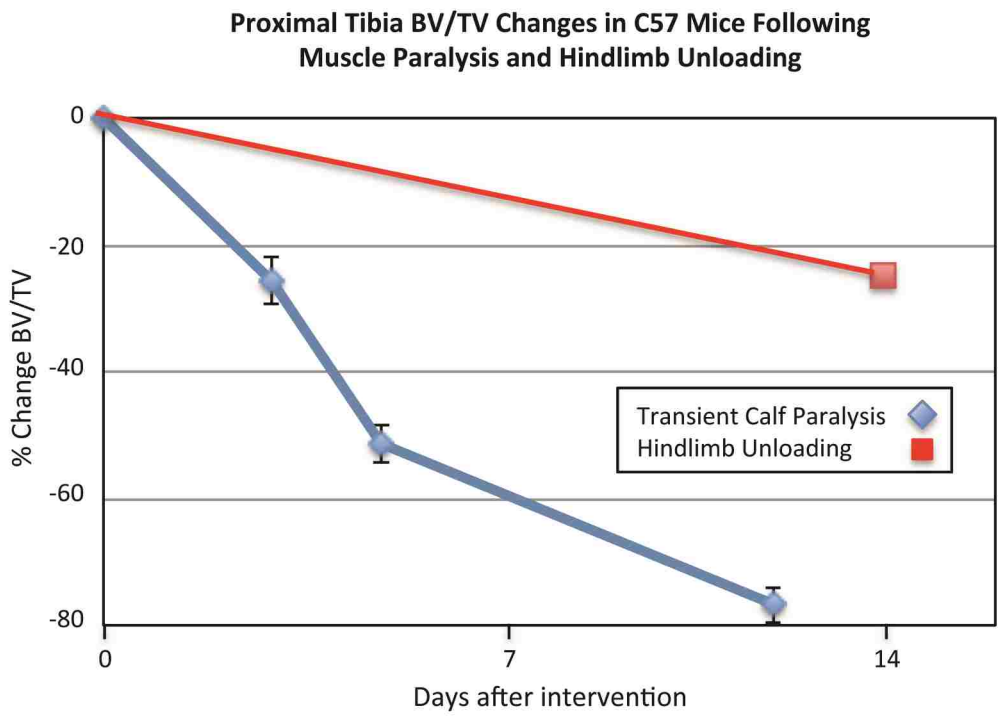

Figure 1.3: Transient Muscle Paralysis vs. Hindlimb Unloading
Bone loss following transient muscle paralysis is substantially greater than that observed following hindlimb unloading in like aged C57 mice. BV/TV is significantly diminished within three days of paralysis and by twelve days is nearly 4 times greater than that observed after 14 days of hindlimb unloading [49, 62].

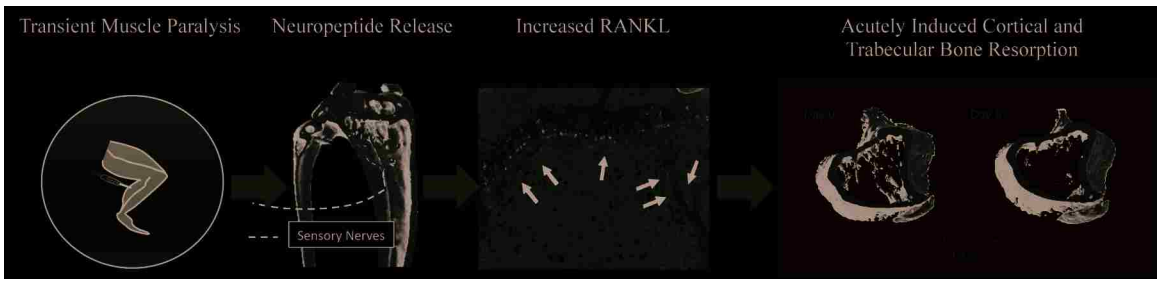

Figure 1.4: Initial Understanding of Transient Muscle Paralysis Induced Bone Loss
Preliminary studies with our model identified the necessity of intact neuronal and RANKL pathways in order to induce acute bone resorption following muscle paralysis. This schematic represents our simplistic view of transient muscle paralysis induced bone loss at the time when this dissertations research began. Our belief that transient muscle paralysis induced neuronal mediated RANKL production represents the initial framework of the investigations contained in Chapters 2-4. A major goal of this dissertation was to identify and clarify intermediate pathways in this process as to better understand muscle/nerve/bone interactions.

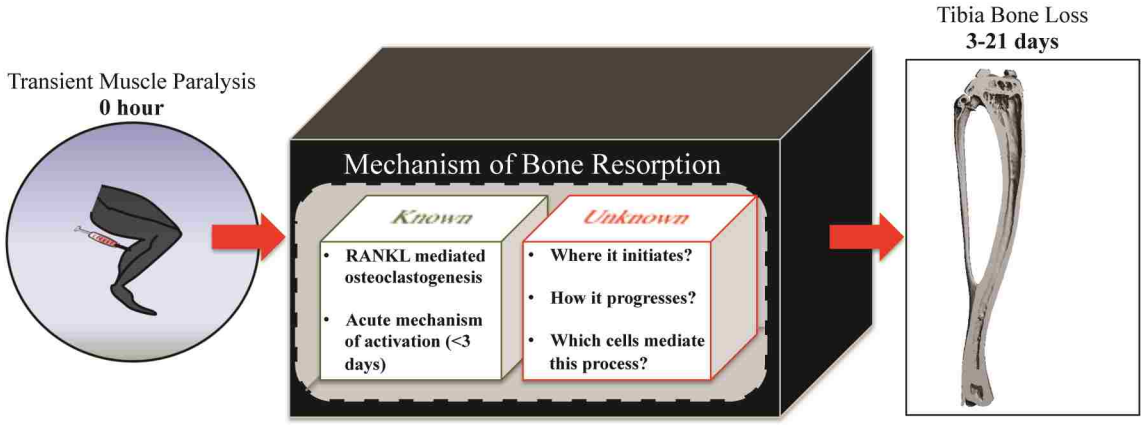

Figure 1.5: Gray Box Model of Muscle Paralysis Engendered Bone Loss
To clarify the mechanisms responsible for acute RANKL-mediated osteoclast activation following muscle paralysis, we focused on three previously unknown aspects of bone resorption in this model. Specifically, we aimed to identify where the bone loss initiates, how bone loss progresses and what cell(s) modulate this process. The studies contained with Chapters 2-4 are based on these overarching questions.

Chapter 2: Cortical Bone Resorption Following Muscle Paralysis is Spatially Heterogeneous

2.1 Abstract

Mechanical loading of the skeleton, as induced by muscle function during activity, plays a critical role in maintaining bone homeostasis. It is not understood, however, whether diminished loading (and thus diminished mechanical stimuli) directly mediates the bone resorption that is associated with disuse. Our group has recently developed a murine model in which we have observed rapid and profound bone loss in the tibia following transient paralysis of the calf muscles. As cortical bone loss is achieved via rapid endocortical expansion without alterations in periosteal morphology, we believe this model holds unique potential to explore the spatial relation between altered mechanical stimuli and subsequent bone resorption. Given the available literature, we hypothesized that endocortical resorption following transient muscle paralysis would be spatially homogeneous. To test this hypothesis, we first validated an image registration algorithm that quantified site-specific cortical bone alterations with high precision and accuracy. We then quantified endocortical expansion in the tibial diaphysis within 21 days following transient muscle paralysis and found that, within the analyzed mid-diaphyseal region (3.15 mm), site-specific bone loss was focused on the anterior surface in the proximal region but shifted to the posterior surface at the distal end of the analyzed volume. This site-specific, but highly repeatable biologic response suggests active osteoclast chemotaxis or focal activation of osteoclastic resorption underlies the spatially consistent endocortical resorption induced by transient muscle paralysis. Clarifying this relation holds potential to yield unique insight into how the removal of factors critical for bone homeostasis acutely precipitates local modulation of cellular responses within bone.

2.2 Introduction

Deficits in the skeleton's physiologic loading environment have potential to rapidly degrade bone mass and architecture presumably as a consequence of diminished mechanical stimuli [48, 49, 54, 56, 63]. Just as the anabolic response of bone to mechanical loading is focal and not systemic, the catabolic response of bone to disuse is also highly localized [64-67]. However, the biological processes mediating these highly localized bone alterations remain unclear.

Previous investigations into the site-specificity of cortical bone resorption in models of bone loss are limited and have produced contrasting results. For example, in murine models of postmenopausal bone loss, highly heterogeneous alterations in cortical bone morphology were observed following OVX surgery [68, 69]. In contrast, complete functional deprivation via surgical osteotomies resulted in uniform bone resorption on the endocortical diaphyseal surface [70]. These findings suggest that the spatial pattern of bone loss may vary as a function of the stimulus for bone loss. If so, clarifying this spatial relation holds potential to yield unique insight into how the removal of factors critical for bone homeostasis acutely precipitates local modulation of cellular responses within bone.

In this context, the development of high-resolution micro-computed tomography (μCT) imaging systems capable of small animal *in vivo* scanning has enabled precise and accurate quantification of bone alterations in a variety of *in vivo* models [71, 72]. However, the ability to quantify site-specific bone alterations (e.g., a specific surface or portions of a surface within a volume of interest) across time requires the capability to accurately register serial *in vivo* images from the same bone. Initial attempts to identify locations of site-specific bone loss have used

either mutual information strategies and/or relied upon user-defined landmarks for registration [68, 73]. However, the accuracy of such approaches will be compromised if the bone microarchitecture and associated landmarks used to register serial μCT volumes are themselves altered by the adaptive response. These challenges are amplified in models of trabecular bone adaptation, which demonstrate adaptive responses on all trabecular surfaces [48, 74, 75].

Alternatively, *in vivo* models of cortical bone adaptation have been observed to demonstrate surface specific adaptation in some experimental conditions. For example, we have reported that hindlimb muscle paralysis via injection of botulinum neurotoxin A (BTxA) induces profound cortical bone loss in the tibia [48, 49]. Morphologically, this loss of cortical bone emerges via acute osteoclast driven endocortical expansion, while the adjacent periosteal surface remains unchanged [48, 49, 76]. As such, we anticipated that this model would be amenable to serial *in vivo* image registration.

Based on the magnitude of acute bone resorption following transient muscle paralysis, which greatly exceeds disuse models that completely inhibit gait induced skeletal loading [77, 78], we hypothesized that cortical resorption following transient muscle paralysis would be spatially uniform around the endocortical surface. In order to test this hypothesis, we developed and validated an image registration paradigm that, when applied to our muscle paralysis model, accurately quantified site-specific cortical bone alterations without requiring user intervention. As this approach relied upon an assumption of a quiescent periosteal surface, we first assessed the precision and accuracy of our image registration method by quantifying the reproducibility of bone morphology parameters at increasing levels of detail in mice that were imaged twice, separated by 24 hours. Once validated, we then used this approach to quantify site-specific endocortical resorption following transient muscle paralysis.

2.3 Methods

2.3.1 Transient Muscle Paralysis Model

All animal studies were performed in accordance with protocols approved by the Institutional Animal Care and Use Committee, University of Washington. Transient muscle paralysis was induced in the right calf muscle group of mice via a single injection of BTxA (2U/100 g body weight, Allergan Inc.) [49]. Mice received BTxA treatment on day 0 and were allowed free cage activity for the remainder of the experiment. This intervention induces rapid and significant degradation of both trabecular and cortical bone compartments in the tibia [48, 49].

2.3.2 Experimental Design

Female C57Bl/6 mice were obtained from Jackson Laboratories with studies initiated when the mice reached 16 weeks of age. Three experiments were undertaken. The purpose of the first experiment was to validate the precision of the image registration approach. For this experiment, a group of untreated mice (Validation Group, n=6) were imaged on day 0 and again 24 hours later, a time interval in which no change in bone morphology could occur at the implemented imaging resolution. By eliminating potential morphology alterations, this analysis enabled volumetric registration of serial bone scans with only two sources of variability; that associated with the repeated positioning of the mice in the μCT scanner and the image acquisition variability native to the μCT scanner. The second experiment assessed our hypothesis that cortical resorption following transient muscle paralysis was spatially homogeneous. In this study, a group of mice did not receive BTxA and served as age-matched

controls (Age-Matched Controls, n=6). A second group received BTxA injection in the right calf on day 0 (BTxA Group, n=14). Both groups were imaged on day 0 and again on day 21. The third and final experiment sought to establish an initial biological framework for the spatial pattern of osteoclastic resorption by comparing it to the patterns of osteoblastic activity at the endocortical surface. In this study, a group of untreated mice were injected with two calcein labels (day 0 and day 9; 15 mg/kg i.p.) and standard dynamic histomorphometry was used to determine endocortical mineralizing surface (e.MS; Histomorphometry Group, n = 5).

2.3.3 μCT Imaging

High-resolution μCT images of the right tibia midshaft were obtained for all mice on day 0 (Scanco μCT 40; 10.5 μm voxel size, 55 kVp, 145 μA). While anesthetized with isoflurane, the right hindlimb of each mouse was secured in a custom apparatus in order to maximize the reproducibility of leg orientation and stability during the scan process. The imaged region spanned a 4.15 mm section of the tibia mid-diaphysis centered 2.75 mm proximal to the tibia-fibula junction (Fig. 2.1A). A second scan of the same region was performed on the Validation Group 24 hours following the first imaging, and on day 21 for the Age-Matched Control and the BTxA Groups.

2.3.4 Image Registration

Prior to registration, all raw μCT image data was preprocessed using a Gaussian Filter algorithm to remove image noise (Sigma = 1.2, Support = 2.0), followed by cortical bone segmentation within the scan volume using standard image thresholding techniques [79]. Specifically, image data were binarized using a manufacturer recommended threshold for

cortical bone identification (705.97 mg HA/cm^3) where dataset values greater than or equal to the threshold were considered calcified tissue.

Pilot studies examining cortical bone loss three weeks following calf paralysis indicated that the periosteal volume remained unchanged within the distal 50% of the scan volume (i.e., distal 2.1 mm) utilized in this study. We therefore used this region of the imaged bone as a registration landmark (i.e., registration volume) to register the entire secondary scan volume onto the primary scan volume obtained on day 0.

The endocortical volume of the binarized cortical bone scan was digitally filled using custom image editing software (Matlab). The edited primary and secondary scans of individual mice (i.e., filled periosteal volumes) were registered using a vendor supplied 3-D image registration program (Scanco IPL Registration Command). Alignment of filled μCT volumes occurred through iterative identification of optimal translational and rotational parameters (Fig. 2.1). Image registration was achieved via stepwise trial translations and rotations (using a combination of simplex and Powell's search methods) that minimized the function 'f=1-r' (with 'r' being the correlation coefficient and 'r=1' representing a perfect correlation) [80, 81]. To avoid approaching 'local minima' solutions, image registration was performed initially on a courser resolution than the original scan volume (1/16 of original scan resolution). As the search neared a global minimum, the resolution increased to that of the original scan resolution in order to enable voxel accurate results. The procedure was iteratively performed until no further improvement in image registration was obtained (i.e., changes in '1-r' less than 1.0E-5). Thus, a secondary imaged volume of bone that was both translationally and rotationally out of alignment with the primary imaged volume was sequentially and progressively re-aligned with the primary imaged volume (Fig. 2.1). Once image rotational and translational parameters were identified

that optimally registered the filled periosteal volumes, these parameters were then reapplied to the raw datasets (i.e., original scan datasets), allowing for image registration that did not rely on endocortical morphology.

2.3.5 Assessment of Cortical Bone Morphology

Following alignment, spatially-registered, raw serial μCT scans were exported to custom image processing software (in Matlab) for evaluation of bone morphology. The center 3.15 mm of each scan volume was used for analysis in all studies (the literature indicated that a ± 0.5 mm z-dimension variation in scan origins of serial μCT scans was sufficient to account for variability in z-dimension positioning of tibia; [82]). Cortical bone measures were quantified by summing the non-zero voxels in the thresholded binary data sets. To quantify periosteal measures, the endocortical volume within the cortical bone data sets was digitally filled using custom imaging software and non-zero voxels quantified. Endocortical measures were determined as the difference between periosteal and cortical datasets. Cortical porosities were treated as endocortical volume as it was assumed that they would be similarly affected by osteoclastic activity. As these porosities on average (± s.e.) account for only 0.6 ± 0.1% of the total endocortical volume, the total contribution of the cortical porosities to overall bone loss was minimal.

Cortical bone morphology was characterized at three levels of scale: 1) the entire analyzed scan volume (whole bone), 2) at seven transverse cross-sections equally spaced along the analyzed volume (cross-section), and 3) eight circumferential sectors within each of three cross-sections equally spaced along the analyzed volume (site-specific). The three equally

spaced cross-sections examined in the site-specific analysis bracketed the analyzed volume and were labeled Proximal, Midshaft and Distal, respectively.

The morphologic parameters quantified at the whole bone level included periosteal volume (Ps.Vol), cortical volume (Ct.Vol) and endocortical volume (Ec.Vol). For cross-sectional and site-specific analyses, periosteal area (Ps.Ar), cortical area (Ct.Ar), and endocortical area (Ec.Ar) were quantified. To identify site-specific (i.e., circumferential) bone morphology, each primary and registered secondary 2-D cross-section was partitioned circumferentially into 8 equal angled sectors originating from the center of mass of the cortical bone cross-section of the primary (Day 0) scans. Eight sectors per cross-section were chosen based on pilot data indicating that further increasing sectors per cross-section did not improve the ability of this technique to identify focal circumferential bone changes [83].

2.3.6 Outcome Measures

Bone morphology measures were determined at all three levels of scale and were used to assess the accuracy of the image registration approach (Validation Group) and the tissue location of cortical bone alterations (Age-Matched and BTxA Groups). Differences were determined by comparing the primary and registered secondary scans. Whole bone analysis quantified the percent difference of entire scan volumes. Cross-sectional analysis was used to assess bone alterations along the long-axis of the scan volume at each of seven equally spaced 2-D transverse cross-sections. Finally, site-specific circumferential bone morphology alterations within the Proximal, Midshaft and Distal cross-sections were quantified on a per sector basis.

Image Registration Accuracy

To quantify image registration accuracy, secondary (Day 1) scans were superimposed on primary (Day 0) scans for the Validation Group. The mean absolute percent error (MAPE) between the bone volume measures in the primary and registered secondary scan volumes were then calculated at the whole bone, cross-section and site-specific levels (i.e., perfectly aligned, volumetrically-identical serial scans would produce mean absolute percent errors of 0% for all measures at all scales).

To determine at which level of scale image registration became necessary to accurately reproduce morphologic measures, the MAPE calculated for registered secondary volumes was compared to the MAPE calculated for unregistered secondary volumes. To accomplish this, unregistered secondary images were assumed to have identical global coordinates as the primary images (e.g., the most distal cross-section in the unregistered secondary image corresponded with the most distal cross-section in the primary image).

Finally, we assessed the accuracy of the image registration technique (which relied on the assumption of a quiescent periosteal volume) in the presence of simulated endocortical bone resorption (i.e., mimicking the anticipated effect of BTxA). For this simulation, we digitally imposed homogeneous endocortical resorption onto the Day 1 scans. Specifically, a 31.5 micron thick volume of cortical bone was digitally removed homogeneously from the entire endocortical surface (altered Day 1 scans). Day 1 scans before and after simulated endocortical bone removal were identically oriented. Comparison of the altered and unaltered Day 1 scans did not require image registration and site-specific bone loss identified in this comparison therefore serve as the benchmark pattern of bone loss. We then registered altered Day 1 scans onto the Day 0 scans as described above, calculated site-specific endocortical bone loss at the Midshaft cross-section,

and contrasted those data with the benchmark pattern of bone loss. This comparison enabled us to assess the accuracy of the image registration approach in the presence of significant, albeit digitally imposed, homogeneous endocortical expansion.

Bone Loss Induced by Muscle Paralysis

Changes in bone morphology induced by transient muscle paralysis were determined by assessing alterations in bone morphology (expressed as percent difference from Day 0) at each of the three levels of scale for Age-Matched Control and BTxA treated mice. A comparison of periosteal volumes was first performed to confirm that no significant alterations of the periosteal volume occurred within 21 days of BTxA treatment. Given our hypothesis and previous data demonstrating that cortical bone loss arises due to endocortical expansion, the site-specific analysis was confined to assessing alterations in endocortical area (Ec.Ar) at three equally spaced cross-sections along the scan volume.

Comparison of Endocortical Bone Formation and Bone Resorption

Endocortical mineralizing surface (e.MS) was quantified in the right tibia of Histomorphometry mice using standard dynamic histomorphometry [84, 85]. To assess focal osteoblast function, e.MS was calculated within each of eight sectors (identical to the sector morphology analysis above) for both the Proximal and Distal cross-sections. Circumferential e.MS in the Histomorphometry mice (which were untreated) was then contrasted with locations of endocortical expansion induced in mice following transient muscle paralysis. To facilitate comparison of focally induced osteoclast activity versus baseline osteoblast activity, the endocortical expansion (BTxA Group) and e.MS (Histomorphometry Group) datasets were

normalized by quantifying the contribution of each sector to the overall cross-section total (either total endocortical expansion or total e.MS).

2.3.7 Statistics

Paired T-tests were used to compare precision of the image registration algorithm to reproduce bone morphologic measures at all three scales investigated. Treatment effects of BTxA were determined by comparing differences in Age-Matched Control versus BTxA Groups using unpaired T-tests (at the whole bone level) and MANOVA with a Bonferroni post-hoc analysis (at the cross-section level). One-way ANOVA with a Bonferroni post-hoc analysis were used to determine circumferential non-uniformity of bone loss at the three individual cross-sections examined. The circumferential difference between e.MS in the Proximal and Distal cross-sections in untreated Histomorphometry mice were determined using unpaired T-tests. A focused ANOVA with a Bonferroni post-hoc analysis comparing sector differences in normalized e.MS and normalized endocortical expansion was used to contrast areas of baseline osteoblastic activity with focal areas of endocortical resorption induced by transient muscle paralysis. Statistical significance was determined at $p<0.05$ in all assessments.

2.4 Results

2.4.1 Image Registration Accuracy

Using the periosteal volume as the registration landmark, our image registration approach produced highly correlated registered images in the Validation Group ($r=0.995 \pm 0.001$) requiring an average (± s.e.) of 282 ± 18 iterations per specimen to reach optimal registration parameter values. At the whole bone level, the MAPEs in both registered and unregistered scans

were less than 0.5% regardless of morphologic outcome measure (Table 2.1). Similarly, the MAPEs for all morphology parameters in the transverse cross-section analysis were small (less than 1.0%) and not significantly different between registered and unregistered scans (Table 2.1). Image registration substantially improved the reproducibility with which bone morphology parameters could be measured at specific sites within a given cross-section. On a per sector basis, the MAPEs in registered scans were significantly reduced compared to unregistered scans for Ps.Ar ($p<0.02$), Ct.Ar ($p<0.03$) and Ec.Ar ($p<0.02$; Table 2.1).

Image registration did not affect the ability to accurately quantify a known simulated endocortical bone loss in the digitally altered Day 1 scans at any of the three levels of scale. At the whole bone level, there was no significant difference in the percent Ec.Vol alterations quantified in the benchmark and registered Day 1 scans (26.3 ± 0.4% vs. 26.2 ± 0.5%, $p=0.73$). Similarly, endocortical expansions quantified at the cross-sectional level was similar in benchmark and registered Day 1 scans (26.4 ± 0.4% vs. 26.3 ± 0.4%, $p=0.77$). Finally, a comparison of site-specific endocortical expansion at the Midshaft cross-section showed no significant difference between the quantified per sector bone loss in the benchmark and registered Day 1 scans for any sector (Fig. 2.2).

2.4.2 Cortical Bone Loss Induced by Transient Muscle Paralysis

At the whole bone level, muscle paralysis did not alter Ps.Vol compared to Age-Matched Control mice (-0.7 ± 0.3% versus –0.6 ± 0.3 %, respectively; $p>0.78$). As expected, muscle paralysis significantly decreased Ct.Vol over 3 weeks compared with Age-Matched Controls (-6.9 ± 1.1% versus 1.6 ± 0.9%, respectively; $p<0.001$), due to a significant expansion of Ec.Vol (9.4 ± 1.6% vs. -3.5 ± 1.7%, $p<0.001$).

At the cross-sectional level, changes in periosteal volume were small and non-significant in BTxA treated mice (ranging from 0.4% to -1.4%) and did not differ from Age-Matched Controls at any cross-section examined (Fig. 2.3). Within the distal region used to register the bone, where the assumption of unchanged periosteal volume was made, alterations in Ps.Ar were particularly small (between 0.4% to -0.5%). Muscle paralysis decreased Ct.Ar compared with Age-Matched Controls, with six of seven cross-sections demonstrating statistical significance (Fig. 2.3). Identical to the bone loss pattern identified at the whole bone level, decreased Ct.Ar arose via a significant increase in Ec.Ar in the BTxA treated group compared to Age-Matched Controls in all seven cross-sections (Fig. 2.3).

At the site-specific level, observed patterns of bone loss were in sharp contrast to our hypothesis that transient paralysis would induce uniform endocortical resorption. Specifically, the assessment of endocortical expansion in the three analyzed cross-sections spanning the mid-diaphysis region of interest revealed heterogeneous, but reproducible, patterns of bone resorption. At the Proximal location, mean endocortical expansion due to muscle paralysis was most heterogeneous (range: 36.4 to -3.9%) and focused primarily in the anterior sectors of the cross-section (Fig. 2.4). At the Midshaft, endocortical expansion was the most uniform, but still demonstrated regions of profound and minimal bone loss (19.9 to 5.2%; Fig. 2.4). Endocortical resorption in the Distal cross-section was also site-specific (28.1 to 4.9%, Fig. 2.4), but, in contrast with the Proximal cross-section, maximal bone resorption was focused within the posterior aspect of the cross-section.

2.4.3 Comparison of Endocortical Bone Formation and Bone Resorption

The spatial distribution of osteoblast activity varied between the Proximal and Distal cross-sections in untreated Histomorphometry mice (Table 2.2). For the Proximal cross-section, e.MS was significantly greater on the posterior/medial cortex (Sector 6, $p<0.05$), while at the Distal cross-section e.MS was significantly greater on the anterior/medial cortex (Sector 4, $p<0.02$; Table 2.2). Qualitatively, the sites of baseline endocortical osteoblast activity did not spatially correspond with sites of focal osteoclast activity (Fig. 2.5A&B). At the Proximal cross-section, the normalized baseline e.MS was significantly different from the normalized endocortical expansion induced in sector 6 ($p<0.03$, Fig. 2.5C). At the Distal cross-section, baseline normalized e.MS was significantly different from sites of induced osteoclast activity in sectors 3, 4, 6 and 7 ($p>0.04$, Fig. 2.5C).

2.5 Discussion

Contrary to our hypothesis, we found that endocortical expansion induced by transient muscle paralysis of the calf was remarkably site-specific within the tibia mid-diaphysis of all mice. We identified this spatial pattern of bone resorption by developing and validating an automated image registration procedure that was capable of defining focal *in vivo* bone loss if the periosteal volume was unchanged during the experimental intervention. The reproducibility of sites of focal endocortical expansion across animals suggests a locally mediated process in which specific regions of the endocortical surface actively enhanced or inhibited osteoclastic attachment and/or resorption.

The literature describing site-specific bone loss has primarily focused upon the varied sensitivity of different skeletal regions to disuse [64, 86-88]. A single previous study reported

uniform diaphyseal endocortical expansion following functional isolation of the turkey radius, though activation of intracortical resorption in this model was distinctly non-uniform [70]. Though these previous results, in part, led to our hypothesis, two differences between that study and the present study are likely to underlie the distinct results. First, the previous study used a best-fit strategy to align cross-sectional images that is likely to have biased assessment of focal endocortical resorption. Second, from a mechanical perspective, complete isolation from functional loading via osteotomies is likely to induce a much more profound deprivation of mechanical stimuli than transient calf paralysis.

We first determined the scale (whole bone, cross-section, or site-specific) at which our image registration approach was required to accurately identify biological adaptation given the variability inherent with repeatedly imaging the same region of cortical bone. This variability arises from a combination of the actual image acquisition by the μCT scanner and the reproducibility of aligning the specimen within the μCT scanner. We found that image registration produced no significant improvement in the ability to detect alterations that occur across or along the entire scan volume (i.e., no improvement on whole bone or transverse cross-section comparisons in Validation Group mice). This finding is consistent with recent published data showing that whole bone metric parameters are reproducible across scans [89]. However, image registration did significantly improve the ability to align bones circumferentially (as represented at the site-specific level). These results demonstrate that accurate *ex post facto* image registration is required in order for *in vivo* quantifications of site-specific bone alterations. Critically, it is this level of detail that is needed to explore focal cellular activity that is responsible for achieving acute bone adaptation.

In this study, we used the periosteal volume of the tibia mid-shaft as an unchanged landmark capable of registering serial images. This assumption requires that the periosteal volume (i.e., the filled volume) remains quiescent through the study duration (i.e., unchanged volume not a result of an equilibrium between bone resorption and apposition). We have previously published dynamic histomorphometric data indicating that osteoblast activity on the periosteal surface of the tibia mid-diaphysis was not altered when the calf was paralyzed by BTxA [48]. These data, taken with unchanged μCT periosteal volume measures identified both in this study and in previous studies [48], confirms that the tibia mid-shaft periosteal volume remained quiescent for up to 3 weeks following transient calf muscle paralysis.

Identification of an invariant registration landmark within *in vivo* models that also demonstrate profound alterations in bone morphology has been a primary impediment to using serial high-resolution μCT imaging to accurately quantify site-specific bone adaptation. To circumvent this problem, previous studies have used operator-defined regions of interest (ROI) to enable alignment of μCT images across time via mutual information registration [68, 73]. The implicit assumption is that the bone morphology within the user identified ROI is unvarying through the experiment or that bone apposition/resorption is uniform on all surfaces. Our image registration methodology differs in that we defined the absence of periosteal adaptation through the mid-diaphysis and thus avoided manual identification of registration landmarks or the assumption of uniform bone apposition/resorption. Given the unchanged periosteal volume, we were then able to assess the accuracy of our image registration approach in animals with substantial cortical bone loss. This advancement has allowed us to use serial μCT images to quantify the morphologic result of osteoclast activity, while previous image registration techniques were limited in use to qualitative assessment of bone alterations [73]. As the novelty

of our approach lies with the application of the image registration algorithm (rather than its development), the accuracy and precision of superpositioning unaltered whole bone volumes in our study is similar to those described in other image registration studies [68, 89]. We also assessed our ability to accurately quantify endocortical bone alterations by digitally manipulating the endocortical surface in the Validation Group's Day 1 scans. By comparing this known bone loss (i.e., benchmark bone loss pattern) to that quantified when the altered Day 1 scans were registered on the Day 0 scans, we demonstrated that the image registration approach itself did not affect our ability to accurately quantify focal endocortical bone resorption.

Conceptually, our image registration methodology could be implemented in any animal model in which one cortical surface remains constant through the experiment (i.e., resulting in a constant endocortical or periosteal scan volume). Thus, under anabolic conditions, the strategy could be extended to quantify periosteal adaption should the endocortical surface remain unchanged [85, 90]. However, a clear limitation of our approach is the inability to serially register μCT images of bone regions in which both surfaces are modified during the experiment. Given this limitation, our registration strategy would be best implemented in models that demonstrate rapid, surface-specific bone resorption or formation, as longer time course experiments in rodents will inevitably be confounded by surface modeling [91, 92].

While it is not possible to directly apply our current approach to explore *in vivo* alterations in trabecular morphology (in the absence of a quiescent surface our approach regresses to a best-fit algorithm), it is conceptually possible to extend the strategy to study focal trabecular adaptation. The primary challenge is that acute trabecular adaptation to mechanical loading, disuse, or alterations in systemic hormones is not confined to a single surface [64, 69, 93]. One possible solution would be to simply use our present registration technique on an

expanded scan volume that encompassed the entire bone length in order to identify an unchanged surface. However, such an extended scan volume would greatly increase radiation exposure and time under anesthesia, both of which may be deleterious for normal skeletal health in mice [94]. Instead, we anticipate that accurate trabecular registration could be accomplished by scanning two distinct but smaller volumes (e.g., an unchanged registration volume within the mid-diaphysis and a spatially non-contiguous region spanning the epiphysis and metaphysis). Translational and rotational parameters for the accurate superpositioning of the mid-diaphysis could be applied to the region of interest by using global μCT image coordinates that reference the relative position of non-contiguous bone scans obtained within a single scanning session. This extension would allow for mapping of bone alterations at any skeletal location as long as an unchanged bone volume (periosteal or endocortical) was available within the same μCT scanning session and was part of the same bone 'rigid-body.' Ongoing preliminary studies support further investigation of this strategy [95].

In the current study, we were able to generate a 3-D map of endocortical bone resorption at the tibia mid-shaft following transient paralysis of the calf muscles (Fig. 2.6). In contrast with our hypothesis, regions of focal endocortical resorption were clearly activated along the long axis of the tibia, even within the relatively small analyzed portion of the mid-diaphysis (20% of total diaphyseal length). The consistency of the asymmetric spatial pattern of bone resorption following muscle paralysis suggests that osteoclasts were not homogeneously distributed along the endocortical bone surface, but rather directly recruited to specific surface locations. Resorption in the proximal analysis region was focused on the anterior endocortical surface but resorption in the distal analyzed region was focused on the posterior endocortical surface. As the calf muscle group spans the entire diaphyseal region of study, this result implied that direct

spatial association with the paralyzed muscle is not likely to be the primary mediator of acute focal bone resorption in this model.

Alternatively, given the relation between mechanical stimuli and bone morphology [96-98], it might be suggested that the regions of focal resorption correspond with regions of maximally decreased bone strain. As the gait defect induced by calf paralysis is mild and transient [48], it would be reasonable to assume that the regions of peak tension and compression during gait would be the sites of greatest change in locomotion-induced strain. However, we have recently quantified peak normal strains in the mouse tibia during locomotion, and neither the location of peak tension (anterior/lateral cortex) or peak compression (posterior/medial cortex) corresponds with the regions of focal bone resorption [99].

Given the apparent lack of relation between maximal endocortical resorption and diminished mechanical stimuli, we attempted to determine if normal endocortical osteoblastic activity was spatially associated with focal activation of resorption in the model (or the lack of resorption). We found that regions with significant osteoblastic activity (as defined by calcein labeling) were spatially associated with minimal osteoclastic resorption following muscle paralysis. While preliminary, these data suggest that muscle paralysis induced endocortical resorption was minimally initiated in regions normally undergoing endocortical modeling. Instead, endocortical expansion appeared focused upon surfaces quiescent in naïve mice (or, potentially, accelerated at sites already undergoing modeling associated resorption). These data are consistent with an accentuation of the resorptive aspect of normal cortical bone modeling drift in which accumulated endocortical resorption tends to proceed on the opposite part of the cross-section from accumulated bone formation [100]. A clear limitation of these observations is that quantification of focal endocortical osteoblast and osteoclast activity where performed on

separate groups of mice. However, if these preliminary data were substantiated with more extensive histomorphometry, it would suggest that specific cortical regions are more predisposed to acute bone resorption following muscle paralysis. As such, this type of focal loss could disproportionately diminish bone strength, depending on the plane of bending of the bone.

In summary, we quantified focal areas of acute endocortical resorption within the tibia mid-diaphysis following transient calf paralysis via a single injection of BTxA. To accomplish this goal, we developed and validated a novel approach capable of automated quantification of spatial osteoclastic activity in a model of acute bone resorption. Surprisingly, we found that even within a small volume of the diaphysis, maximal endocortical resorption consistently shifted from the anterior to posterior surface while moving proximally to distally through a relatively small volume of interest. Given the consistent spatial recruitment of osteoclasts following muscle paralysis, we anticipate that future studies hold the potential to clarify the cellular signaling underlying this locally mediated process and thereby identify new strategies for intervening in a variety of bone loss pathologies.

2.6 Spatiotemporal Mapping of Osteoclastic Activity Following Muscle Paralysis

The serial μCT image registration technique described in the above studies allowed for accurate quantification of focal osteoclast activity in the tibia mid-diaphysis up to 21 days following transient muscle paralysis. Given that the vast majority of osteoclastic resorption induced by muscle paralysis occurs within this timespan, we believe this technique is robust enough to define the entire spatiotemporal osteoclastic dynamics (both initiation and progression) in this model. In Chapter 3, we expand our image registration technique to determine the focal initiation of bone loss in the metabolically active trabecular bone of the

proximal tibia metaphysis. As well, we define the spatiotemporal dynamics of osteoclastic resorption in our model with the goal of further understanding the mechanisms involved in mediating bone loss following transient muscle paralysis.

Table 2.1 Mean Absolute Percentage Error in Registered Versus Unregistered Validation Controls [mean ± s.e.][a]

		Periosteal	Cortical	Endocortical
Whole Bone (n=6)	Registered	0.31 ± 0.08%	0.37 ± 0.10%	0.46 ± 0.15%
	Unregistered	0.33 ± 0.05%	0.36 ± 0.10%	0.41 ± 0.20%
Cross-Section (n=6[b])	Registered	0.36 ± 0.07%	0.60 ± 0.08%	0.89 ± 0.11%
	Unregistered	0.42 ± 0.05%	0.66 ± 0.07%	0.93 ± 0.20%
Site-Specific (n=6[b])	Registered	1.95 ± 0.27% *	1.94 ± 0.24% *	3.52 ± 0.31% *
	Unregistered	15.41 ± 3.77%	11.40 ± 2.92%	23.6 ± 5.66%

[a] Perfect spatial reproduction of the Day 0 scan would result in 0% mean absolute error.

[b] Individual animal means for all possible comparisons (Cross-Section: 300; Site-Specific: 1800) were used for this analysis.

* Significantly reduced vs Unregistered ($p<0.05$).

Table 2.2 e.MS Per Sector at Distal and Proximal Cross Sections [mean ± s.e.]

		Proximal	Distal
Sector	**1**	17.1 ± 12.8%	10.8 ± 5.8%
	2	30.5 ± 16.0%	24.9 ± 9.2%
	3	14.7 ± 6.0%	46.3 ± 14.6%
	4	5.7 ± 2.1%	41.6 ± 11.9% *
	5	35.2 ± 8.4%	24.6 ± 10.5%
	6	54.2 ± 15.5% *	14.9 ± 4.7%
	7	34.3 ± 18.8%	11.4 ± 3.5%
	8	10.6 ± 6.2%	2.5 ± 2.1%

* Significant difference between Proximal and Distal cross-sections ($p<0.05$)

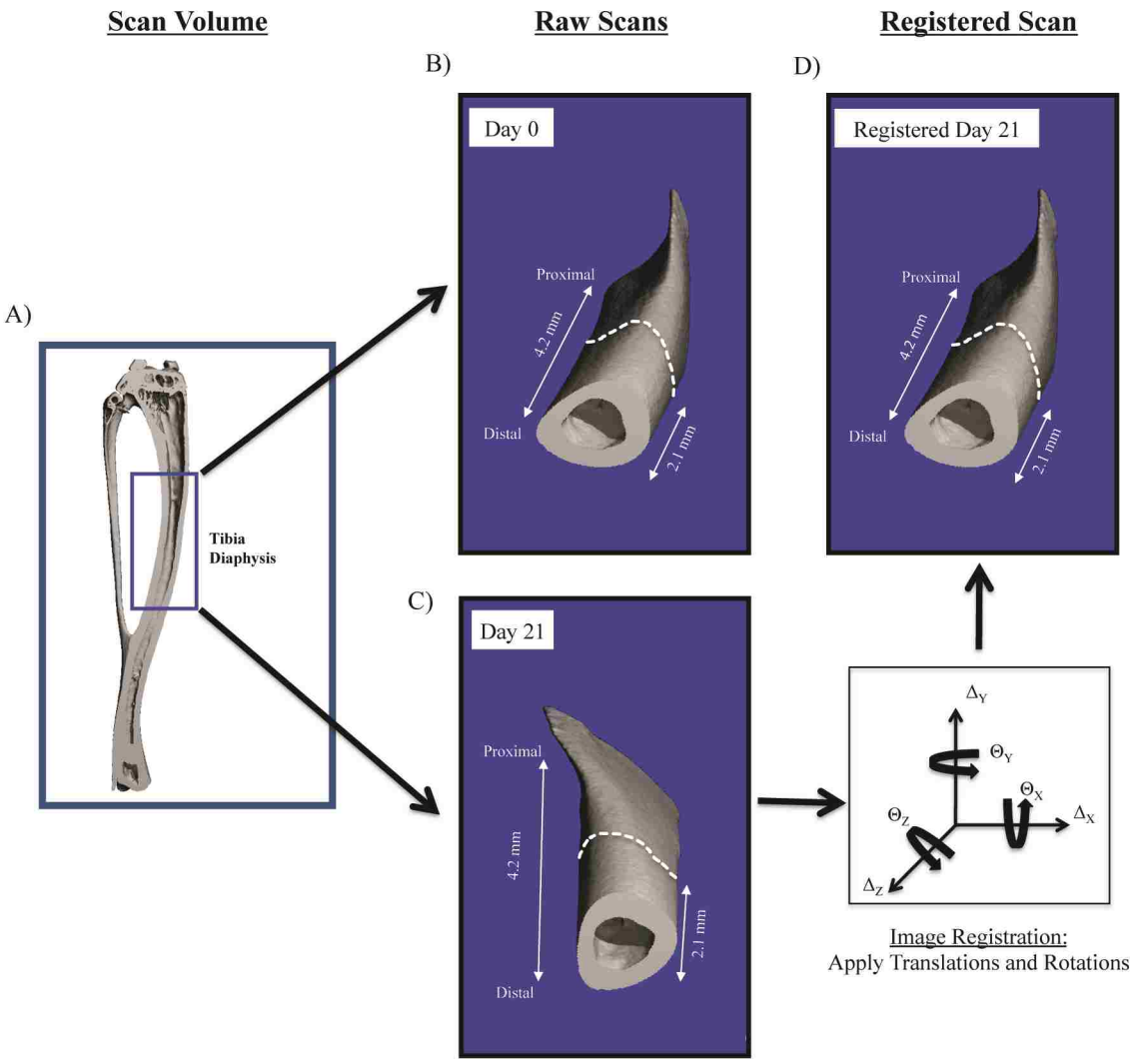

Figure 2.1: Serial µCT Image Registration of the Tibia Diaphysis
Serial µCT scans of 4.15 mm of the tibia diaphysis (A, inset box) were obtained prior to BTxA injection (B, Day 0) with a secondary scan obtained 3 weeks later (C, or 1 day later in the Validation Group). The secondary scan was then registered onto the primary scan (D) using the periosteal volume of the distal 2.1 mm of the imaged region as the registration landmark.

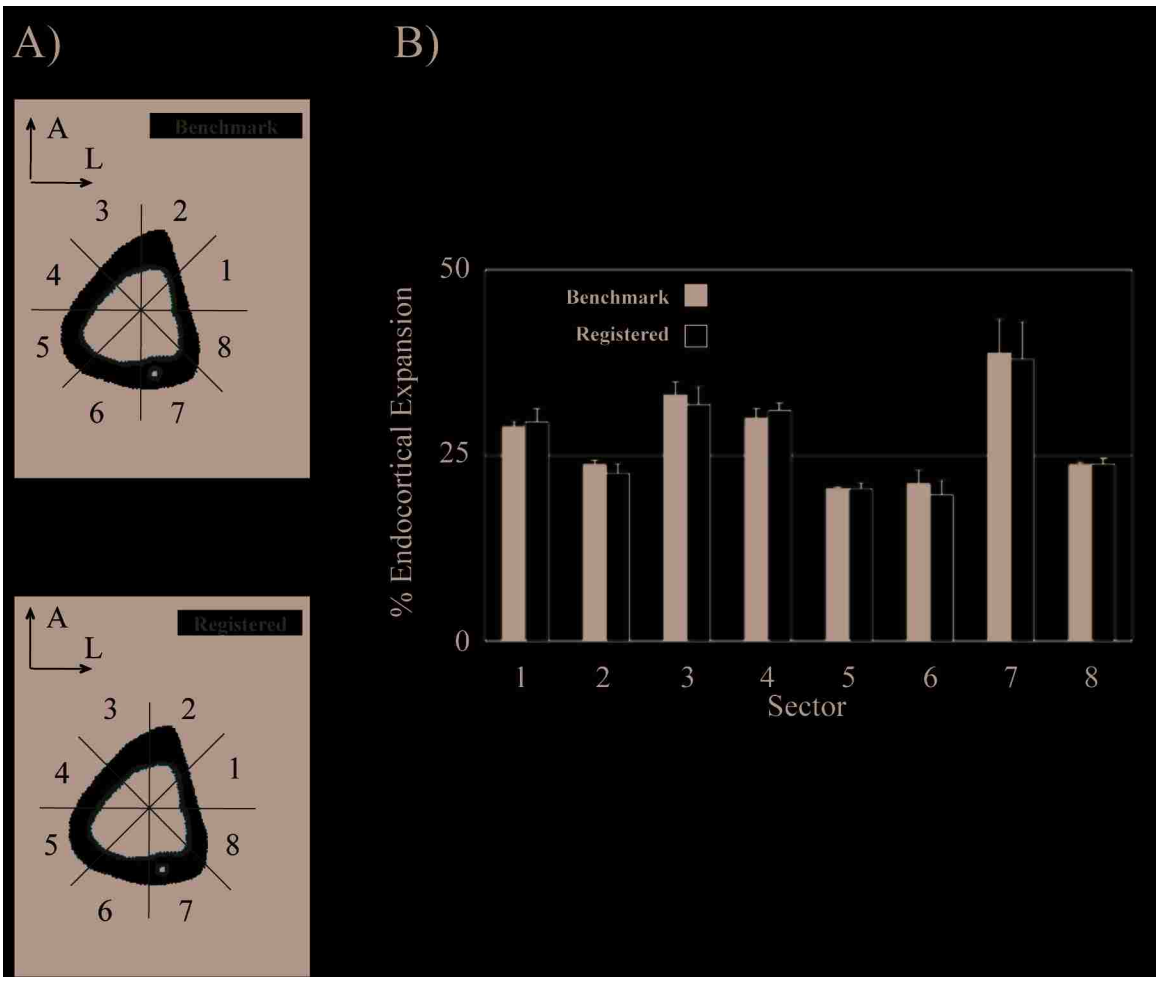

Figure 2.2: Accuracy of Image Registration in Quantifying Known Endocortical Resorption

To measure the ability of our image registration approach to accurately quantify a known bone loss pattern, homogeneous endocortical resorption was digitally applied to each Day 1 scan volume in the Validation Group (-17.9 ± 0.2% induced cortical bone loss). Comparing the digitally altered Day 1 scans to the unaltered Day 1 scans allowed for quantification of a known bone loss pattern (Benchmark; A). The benchmark was than compared to the bone loss pattern observed when the altered Day 1 scans were registered onto the Day 0 scans (Registered, with resorption in red). No significant differences were identified in the circumferential bone loss calculated at any sector (B; $p>0.95$).

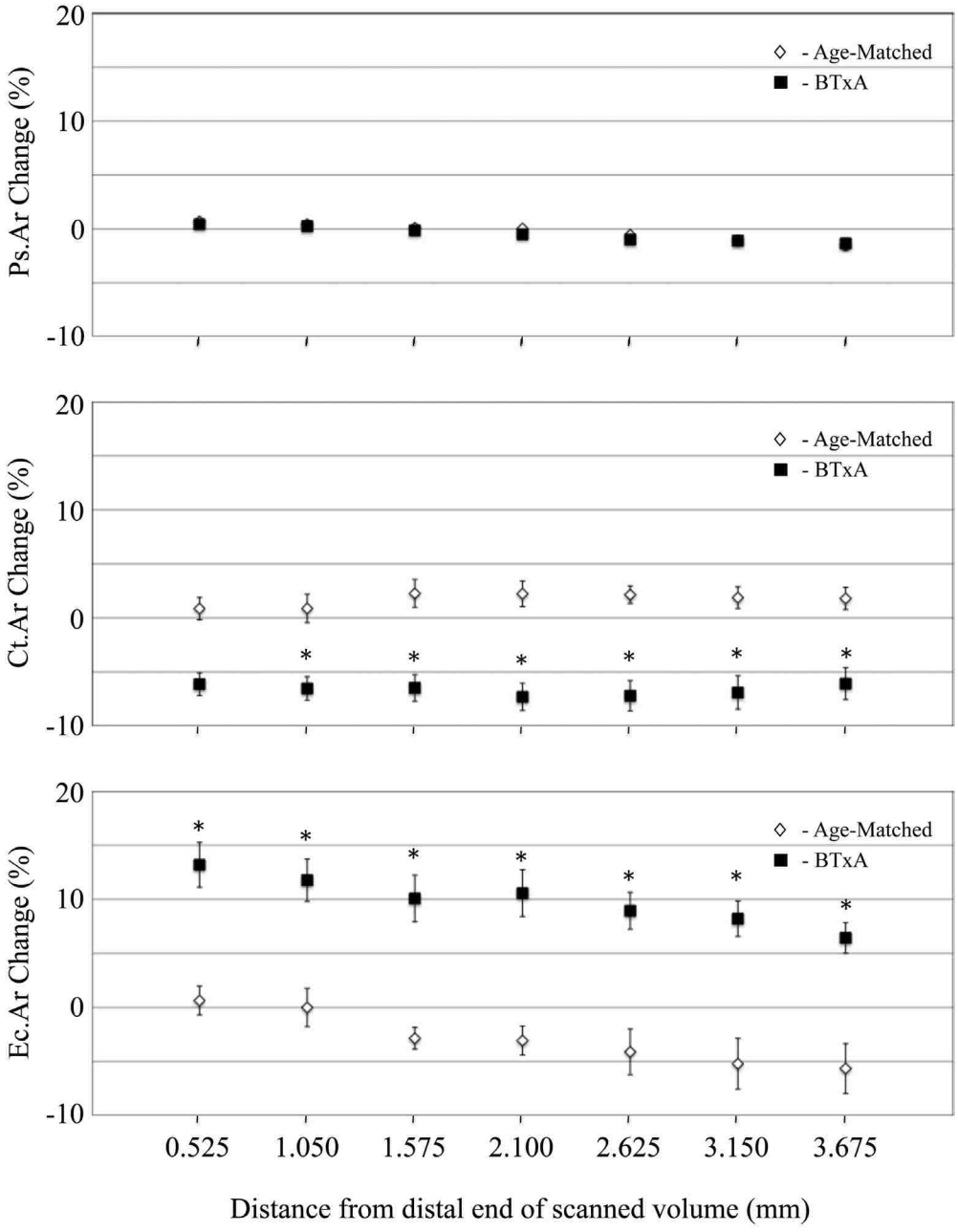

Figure 2.3: Cortical Alterations Along the Scan Volume
Transient muscle paralysis did not alter periosteal surface changes (A; Ps.Ar) at the analyzed 2-D transverse cross-sections in Age-Matched (white diamond, partially obscured by overlying BTxA data) vs. BTxA mice (black square, mean ± s.e.). In contrast, significant differences in cortical (Ct.Ar) and endocortical morphology (Ec.Ar) were identified at all but one cross-section examined in BTxA vs. Age-Matched Control mice (*, significantly differences vs. BTxA, $p<0.05$).

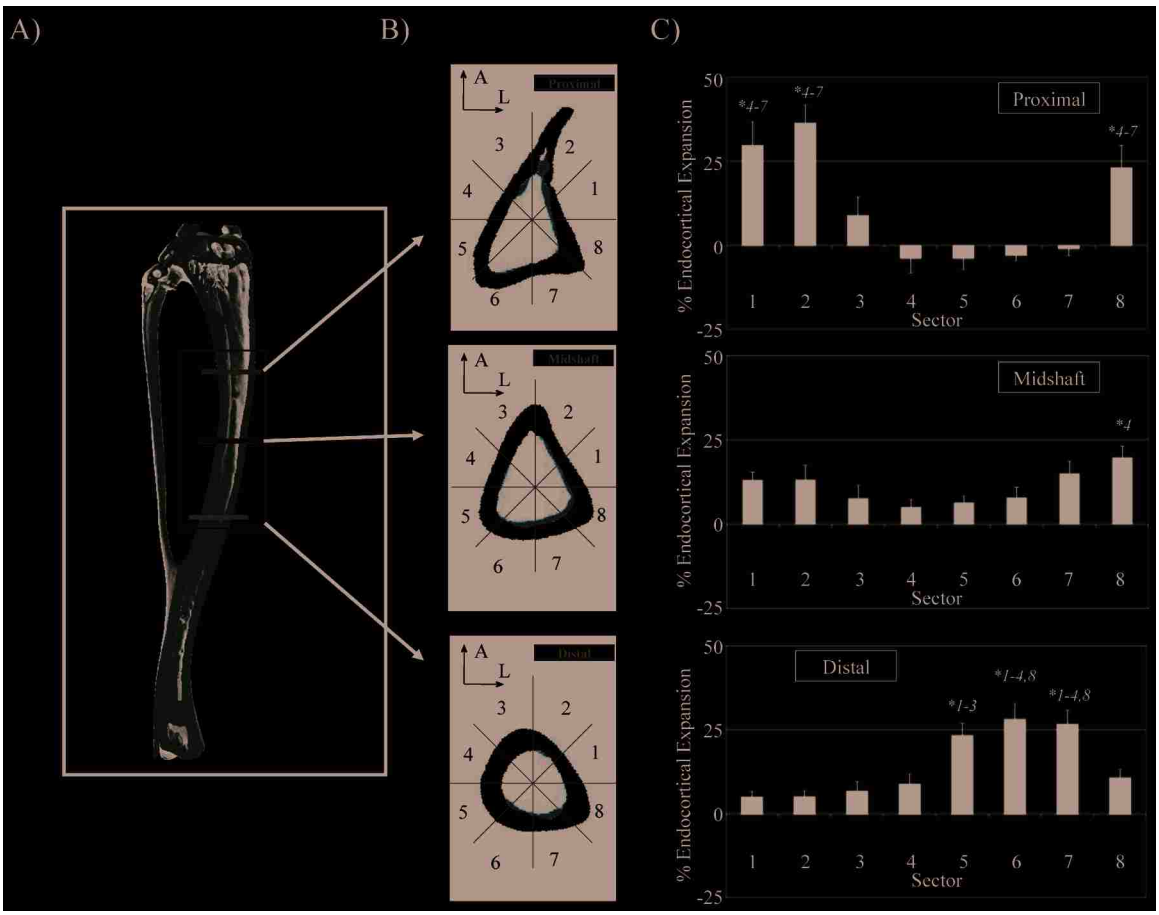

Figure 2.4: Focal Patterns of Endocortical Resorption
Bone loss investigated at three locations equally spaced and flanking the analyzed tibia diaphysis volume (A) showed focal patterns of endocortical expansions that differ along the long axis of the bone (B, bone resorption in red). Bone loss in the proximal cross-section was greatest in the Anterior/Lateral surface (C- Proximal), while bone loss in the distal cross-section was greatest in the Posterior/Medial surface (C- Distal). Endocortical expansion at the tibia midshaft was the most uniform around the circumference of the bone cross-section, yet still varied significantly (C- Midshaft). Significant increases in endocortical expansion across sectors are denoted by an asterisk followed by the sector number(s) in which a significant difference was determined ($p<0.05$).

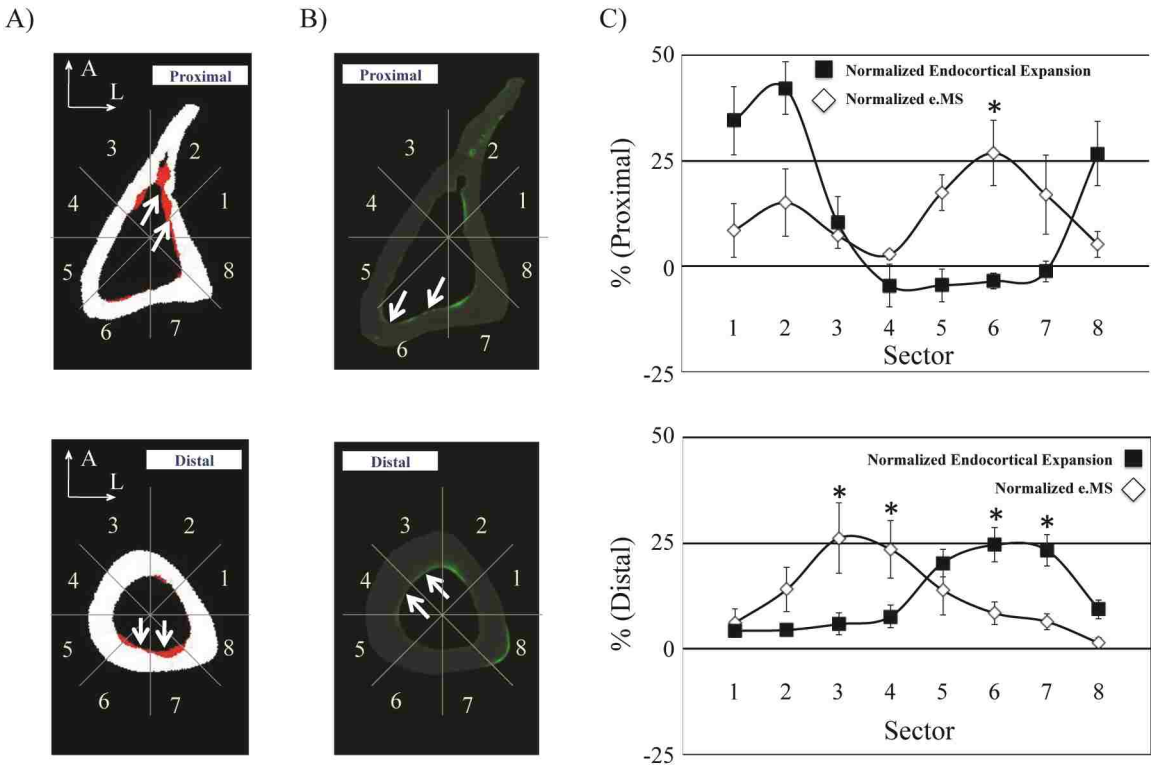

Figure 2.5: Focal Endocortical Resorption Versus Basal Osteoblast Activity
At the Proximal cross-section, osteoclast activity was greatest in the Anterior/Lateral cortex (A-Proximal, white arrows highlighting resorption in red), while the contribution of osteoblast activity was highest on the Posterior/Lateral surface (B-Proximal, white arrows highlighting calcein labeling in green). Conversely, at the Distal cross-section, endocortical expansion occurred primarily in the Posterior cortex (A-Distal, white arrows) while osteoblast activity was greatest on the Anterior/Medial surface (B-Distal, white arrows). Sectors with significant differences between normalized endocortical expansion and normalized e.MS are noted (C; *, $p<0.05$).

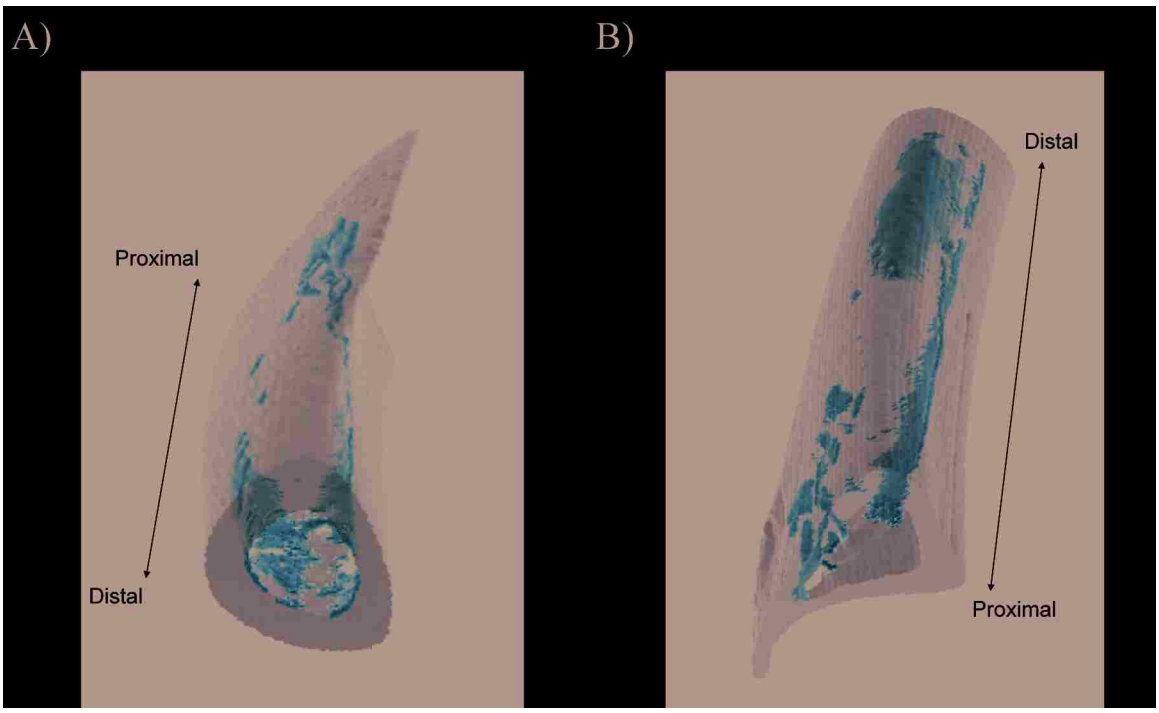

Figure 2.6: Three-dimensional Map of Endocortical Expansion in ROI
three-dimensional representation of transient muscle paralysis induced bone loss (red) as seen from an anterior (A) and posterior (B) view of the same bone. Osteoclastic bone resorption in this model is spatially complex, but highly consistent between animals.

Chapter 3: Metaphyseal and Diaphyseal Bone Loss in the Tibia Following Transient Muscle Paralysis are Spatiotemporally Distinct Resorption Events

3.1 Abstract

When the skeleton is catabolically challenged, there is great variability in the timing and extent of bone resorption observed at cancellous and cortical bone sites. It remains unclear whether this resorptive heterogeneity, which is often evident within a single bone, arises from increased permissiveness of specific sites to bone resorption or localized resorptive events of varied robustness. To explore this question, we used the mouse model of calf paralysis induced bone loss, which results in metaphyseal and diaphyseal bone resorption of different timing and magnitude. Given this phenotypic pattern of resorption, we hypothesized that bone loss in the proximal tibia metaphysis and diaphysis occurs through resorption events that are spatially and temporally distinct. To test this hypothesis, we undertook three complimentary *in vivo*/μCT imaging studies. Specifically, we defined spatiotemporal variations in endocortical bone resorption during the 3 weeks following calf paralysis, applied a novel image registration approach to determine the location where bone resorption initiates within the proximal tibia metaphysis, and explored the role of varied basal osteoclast activity on the magnitude of bone loss initiation in the metaphysis using μCT based bone resorption parameters. A differential response of metaphyseal and diaphyseal bone resorption was observed throughout each study. Acute endocortical bone loss following muscle paralysis occurred almost exclusively within the metaphyseal compartment (96.5% of total endocortical bone loss within 6 days). Using our trabecular image registration approach, we further resolved the initiation of metaphyseal bone loss to a focused region of significant basal osteoclast function (0.03 mm^3) adjacent to the growth plate. This correlative observation of paralysis induced tibial bone loss mediated by

basal growth plate cell dynamics was supported by the acute metaphyseal osteoclastic response of 5-week vs. 13- month-old mice. Specifically, μCT based bone resorption rates normalized to initial trabecular surface (BRR_{BS}) were 3.7-fold greater in young vs. aged mice (2.27 ± 0.27 $\mu m^3/\mu m^2$/day vs. 0.60 ± 0.44 $\mu m^3/\mu m^2$/day). In contrast to the focused bone loss initiation in the metaphysis, diaphyseal bone loss initiated homogeneously throughout the long axis of the tibia predominantly in the second week following paralysis (81.3% of diaphyseal endocortical expansion between days 6 and 13). The timing and homogenous nature are consistent with *de novo* osteoclastogenesis mediating the diaphyseal resorption. Taken together, our data suggests that tibial metaphyseal and diaphyseal bone loss induced by transient calf paralysis are spatially and temporally discrete events. In a broader context, these findings are an essential first step toward clarifying the timing and origins of multiple resorptive events that would require targeting to fully inhibit bone loss following neuromuscular trauma.

3.2 Introduction

Profound catabolic alterations in skeletal morphology are induced by numerous exogenous and endogenous stimuli [1-3, 101-103]. Induced bone loss ranges in extent from focal bone resorption caused by localized deficits in the skeletal loading environment [104, 105] to broad or systemic osteopenia, such as what occurs following ovariectomy [70, 106], bed-rest [107, 108], or as a complication of chronic inflammatory diseases [109, 110]. Given this variability and the differing permissiveness to resorption of trabecular and cortical bone, it has proven difficult to identify common cellular mechanisms that account for such a wide range of resorptive outcomes.

In this context, heterogeneous bone resorption (both between and within individual bones) has been identified in a variety of induced bone loss models [86, 111]. In these models, trabecular bone has been observed to be more susceptible to osteoclastic resorption than cortical bone [86, 88, 112, 113]. However, both genetic (e.g., gender and genetic background) and non-genetic (age and skeletal location/time period investigated) factors can alter, and in some cases transpose, this generality [54, 64, 114, 115]. Cancellous and cortical bone alterations have, as a result, predominantly been studied as independent outcomes. A more complete understanding of how bone loss initiates, propagates and interacts among and between distinct skeletal structures would be an important first step toward understanding the variability of cellular dynamics that may underlie the range of tissue-level resorption in these models.

We have previously demonstrated that transient muscle paralysis of the murine calf muscles induces rapid and profound osteoclastic bone resorption in both trabecular and cortical compartments within the tibia adjacent to the paralyzed muscles [48]. Furthermore, we have partially characterized the temporal nature of this bone loss through acute time course μCT imaging of trabecular bone (proximal tibia metaphysis) and cortical bone (tibia diaphysis) resorption and have found that the timing and magnitude of bone resorption differ greatly in these compartmental tissues [49]. Specifically, significant trabecular resorption in the metaphysis is first observed 3 days following muscle paralysis [49]. Cortical resorption within the tibia diaphysis was slower to occur, with endocortical expansion (as a surrogate for endocortical resorption) first identified 9 days later [49]. While these μCT measures may suggest that temporally distinct bone loss occurred between trabecular and cortical compartments in the model, the experimental design does not allow for the determination of whether this arose through distinct cellular events of varying robustness in the spatially disparate metaphyseal and

diaphyseal compartments or whether this was due to a single continuum of osteoclast resorption initiating in the metaphysis and migrating between compartments. The distinction between a single prolonged or multiple temporally and spatially separate resorptive responses following acute muscle paralysis would be an essential first step toward clarifying the signaling pathway(s) underlying such rapid and profound osteoclastogenesis. Specifically, multiple resorptive responses would be indicative of multiple signaling pathways that would each require individual targeting to completely inhibit bone loss.

In part due to our limited understanding of resorption kinetics in our model, we recently developed a novel μCT image registration approach capable of identifying focal osteoclastic resorption in the tibia diaphysis following muscle paralysis [60]. This goal was achieved by identifying a temporally unaltered image registration landmark in the tibia that enabled accurate superpositioning of serial μCT diaphyseal volumes obtained up to 21 days apart. Utilizing this approach, we were able to quantify, with high precision, the complex spatial dynamics of endocortical osteoclast activity within the diaphyseal region. As this technique is amenable to use in any bone compartment in which a consistent image registration volume can be identified, we anticipated that with modifications to facilitate trabecular alignment this approach could be used to detect the initiating site(s) and progression of focal bone loss (if any) between the metaphysis and diaphysis of the tibia following muscle paralysis.

Given the differences in timing and magnitude of acute bone resorption in the tibia metaphysis and diaphysis following muscle paralysis and the spatial distance between these compartments, we hypothesized that bone loss in the proximal tibia metaphysis and diaphysis occur through spatially and temporally distinct resorption events. To test this hypothesis, we first implemented an imaging strategy that allowed for spatiotemporal assessment of bone loss

following muscle paralysis throughout the metaphyseal and diaphyseal compartments. These data indicated that focal endocortical bone loss initiation occurred immediately adjacent to the proximal growth plate and that metaphyseal and diaphyseal bone loss were likely to occur through distinct osteoclastic events. Two follow-up *in vivo* studies were used to clarify these observations. In the first, we were able to co-localize metaphyseal bone loss initiation to the location of high basal osteoclast activity within the trabecular bone of the proximal metaphysis. The final study then examined whether the level of basal osteoclastic activity influenced the magnitude of acute bone resorption following muscle paralysis.

3.3 Methods

3.3.1 Transient Muscle Paralysis Model

Studies were performed in accordance with protocols approved by the Institutional Animal Care and Use Committee, University of Washington. All mice were female C57Bl/6 obtained from Jackson Laboratories. Transient muscle paralysis was induced in the right calf muscle group of mice via a single injection of botulinum neurotoxin A (BTxA; 2U/100 g body weight, Allergan Inc.) [49]. This intervention induces temporally distinct degradation of trabecular bone tissue in the metaphyseal and cortical bone tissue in the diaphyseal compartments [48, 49]. Mice received BTxA treatment on day 0 and were allowed free cage activity for the remainder of each experiment. Calf paralysis was confirmed 24 hours post-injection by visual examination of reduced toe extension and ankle plantarflexion in the affected limb [48].

3.3.2 Study Design

Study 1: Spatiotemporal Tracking of Bone Loss

The purpose of this study was two-fold. The first was to determine if the acute bone loss initiation previously identified in the trabecular bone of the proximal tibia metaphysis [48, 49] was due to trabecular permissiveness to osteoclast resorption or due to a more acute osteoclastic response in the metaphysis compared to the diaphysis. The second was to determine whether a continuum of osteoclastic resorption temporally and spatially migrates from the metaphysis to the diaphysis or occurs in two distinct events as hypothesized. For this experiment, a group of 16 week old mice (n=6) received BTxA injection in the right calf immediately following a single μCT scan that encompassed both the proximal tibia metaphyseal and diaphyseal envelopes (day 0). Mice in this group were subsequently imaged on days 6, 13 and 20, and euthanized immediately following the last scan.

Study 2: Spatial Initiation of Trabecular Bone Loss

The second study investigated the timing and location of bone loss initiation identified within the metaphyseal compartment in the previous experiment. Based on preliminary data we specifically sought to define the spatial location of bone resorption initiation in the highly metabolically active trabecular tissue within the proximal tibia metaphysis. Prior to the experiment, we first assessed the accuracy and precision of our image registration approach. For this, untreated mice (Registration Control, n=6, 16 weeks) received a set of non-contiguous μCT scans of the proximal tibia metaphysis and the tibia mid-diaphysis. Mice were then removed and re-inserted into the μCT scanner and a second identical set of scans was obtained. This group of mice was used to determine the resolution at which focal bone loss initiation can be identified in

the trabecular compartment of the metaphysis. Next, two groups of mice (n=6/group, 16 weeks) received intramuscular injections of either BTxA (BTxA Registration group) or an equal volume of saline (Saline Registration group) in the right calf on day 0 followed directly by metaphyseal and diaphyseal μCT scans. As we have previously shown that a saline injection in the calf does not alter muscle, trabecular or cortical bone morphology as assessed by μCT [48], saline injected mice were used as controls to maintain consistency vs. BTxA groups (e.g., stress of injections and mouse handling). Mice were subsequently scanned on day 2 and day 3.

Study 3: Basal Cell Activity Modulates Bone Loss Initiation

The final study sought to determine if baseline growth plate cellular dynamics alters the magnitude of acute bone loss initiation following muscle paralysis. A group of 5-week old (Young, n=6) and 13-month old (Aged, n=6) mice received a BTxA injection in their right calf followed immediately by a μCT scan of their right proximal tibia metaphysis on day 0 and a follow-up scan on day 3. The end point of this experiment was chosen based on previous studies with this model [49].

3.3.3 μCT Imaging and Segmentation

High-resolution μCT images of the right tibia were obtained from all mice on day 0 (Scanco μCT 40; 10.5 μm voxel size, 55 kVp, 145 μA). While anesthetized with isoflurane, the right hindlimb of each mouse was secured in a custom apparatus in order to provide reproducible leg orientation and stability during the scan process. The imaged region(s) varied for each experiment. In Study 1, a single scan of 6.3 mm beginning at the distal end of the proximal growth plate and continuing through the midshaft of the tibia was obtained. The scanning

location and time points were designed to detect the occurrence, or lack thereof, of osteoclast migration between compartments. In Study 2, a set of scans encompassed 0.85 mm of the proximal tibia metaphysis immediately distal to the growth plate (Region of Interest, ROI; Fig. 3.1A) and 4.45 mm of the tibia midshaft (starting 0.65 mm proximal from the tib-fib junction; Image Registration Volume, IRV; Fig. 3.1A). The midshaft scan region was identical to that used previously for image registration in this model [60]. In Study 3, a metaphyseal scan region was obtained identically to that described in Study 2.

All raw μCT image data were preprocessed using a Gaussian Filter algorithm to remove image noise (Sigma=1.2, Support=2.0) followed by bone segmentation within the scan volume using standard image thresholding techniques [79]. Two different μCT thresholds were used for bone tissue identification. In scan regions in which trabecular bone tissue was analyzed and/or segmented from the cortical shell, a threshold of 441.23 mg HA/cm^3 was used as to provide the best comparisons between 2-D binarized images and the original gray-scale images across all ages of mice [59]. When cortical bone was exclusively quantified, a manufacturer recommended threshold for cortical bone identification was used (705.97 mg HA/cm^3). All thresholds were verified through manual investigation.

3.3.4 Image Registration

In Study 2, image registration of serial scans was performed to spatially define bone loss within metabolically active trabecular tissue. Image registration was achieved by leveraging phenotypic patterns of bone loss induced by transient muscle paralysis. Specifically, within the timespan investigated (up to 3 days following muscle paralysis) cortical morphology remains unaltered [49]. As such, all IRV scans obtained over this time period were presumed

volumetrically identical. Multiple μCT scans obtained within a single scanning session (e.g. paired metaphyseal and diaphyseal scans) were mapped onto a global coordinate system within the Scanco μCT 40 scanner. This allowed for the relative position of the non-contiguous scans to be identified and thereby rotated and translated as a single rigid body. For all mice in Study 2, spatial superposition of the ROI scans (i.e., trabecular scan volume) was achieved by first registering the volumetrically identical IRV in the primary (day 0) and secondary scans (all subsequent scans) as previously described (Scanco IPL Registration Command: Fig. 3.1B) [60]. Given the acute timespan of this study, we improved the accuracy of our image registration technique by using both the periosteal and endocortical surfaces as image registration landmarks (previous long term studies used only the unchanged periosteum). The rotational and translational parameters determined during IRV image registration were then applied to the ROI scan volumes producing spatially aligned trabecular volumes (Fig. 3.1B).

3.3.5 Study Specific Image Analysis

Study 1: Spatiotemporal Tracking of Bone Loss

We assessed endocortical bone loss across 6.3 mm of the tibia distal to the growth plate, as to avoid the confounding influence of the enhanced resorbable surface to volume ratio of trabecular versus cortical tissue. Though initial endocortical surface varied along the scan volume, our previous data showed that generally less than 50% of the available surface (i.e., endocortical surface) undergoes significant resorption in the 3 weeks following muscle paralysis [60]. As the resorptive 'carrying capacity' of the endocortical surface is not approached, we chose raw endocortical expansion data and not percent change in endocortical surface as the least biased approach available to examine spatiotemporal bone alterations. We therefore assessed

endocortical volume (Ec.Vol) expansion as the primary outcome measure to simultaneously define the onset of osteoclast activity in both metaphyseal and diaphyseal compartments. To accomplish this, all trabecular bone was digitally segmented from the surrounding cortical shell using automated custom software (MATLAB). The scan volume (minus trabecular architecture) was discretized into six bins (each 1.05 mm) beginning at the growth plate. Endocortical volume (Ec.Vol) within bins was individually determined, and alterations occurring between each μCT scan were integrated to assess the spatiotemporal nature of endocortical resorption over the length of the tibia from just below the growth plate to the mid-diaphysis.

Study 2: Spatial Initiation of Trabecular Bone Loss

As the translational and rotational parameters used to superimpose the trabecular ROI are based on cortical bone registration (i.e., IRV registration), the accuracy of the IRV registration was first determined in all groups. This was achieved by calculating the percent misalignment (i.e., the percent of non-overlapping scan volume to the average scan volume of the IRV scans) of the center 3.4 mm of the IRV scan. Given that trabecular registration (i.e., ROI registration) occurs through rigid body rotations and translations, accuracy of IRV registration was assumed to be proportional to accuracy of ROI registration allowing for quantification of alterations of trabecular bone architecture within the highly metabolically active metaphyseal compartment.

Prior to determining the location(s) where bone loss initiates in the trabecular compartment following muscle paralysis, we examined whole tissue changes in the experimental animal groups using standard trabecular μCT analysis measures [59]. This analysis included quantification of endocortical volume (Ec.Vol or TV), trabecular fraction (BV/TV), trabecular number (Tb.N), trabecular thickness (Tb.Th) and trabecular spacing (Tb.Sp).

To determine focal alterations in trabecular morphology, trabecular bone in the registered proximal tibia metaphysis (i.e., ROI) was segmented from the surrounding cortical shell using custom software (MATLAB). Unlike the analysis of whole tissue changes in which separate user-defined ROI's were determined for primary and secondary scan volumes of varied spatial orientation, this technique allowed for a single automated ROI to be defined for both primary and registered secondary scans reducing the amount of variation in the data acquisition. The trabecular compartment of the ROI was then discretized into five equally spaced volumetric elements in each anatomical dimension based on the anatomical extremes of the primary volume (125 total elements). Element locations were identified numerically from medial to lateral, posterior to anterior, and proximal to distal, in that order (e.g., $Element^{1,1,1}$ representing the most medial, posterior and proximal element). To quantify bone loss as a function of the proximity to the growth plate, elements within the same transverse plane were grouped (proximally to distally) into Stacks (e.g., $Elements^{1\text{-}5,1\text{-}5,1} = Stack^{1}$).

The precision of the trabecular image registration was determined in the Registration Control group in order to quantify the resolution at which focal bone resorption could be identified. Specifically, the average difference and standard deviation of bone volume between corresponding non-zero Elements in the primary and registered secondary images were calculated. The average difference and standard deviation of the Registration Control group were then used to identify significant alterations in the experimental groups (i.e., BTxA and Saline Registration groups).

Study 3: Basal Cell Activity Modulates Bone Loss Initiation

During the course of Study 3 we attempted to implement trabecular image registration in Young and Aged animals using simultaneously obtained IRV scans. However, the rapid bone

alterations in the diaphysis of Young animals made accurate image registration impossible and we therefore did not include image registration data in this study. Thus we first performed standard trabecular μCT based analysis on all metaphyseal scans [48]. Given the baseline morphological differences in the trabecular bone of Young and Aged animals and its potentially confounding effect on interpreting standard bone loss metrics, μCT based dynamic bone morphometry parameters normalized to initial trabecular structure were also determined. Bone resorption rates (BRR) were quantified and then normalized either to day 0 trabecular bone volume (BRR_{BV}) or day 0 trabecular bone surface (BRR_{BS}), as previously described [116]. Prior to data analysis in this study, one Young mouse was removed due to a failed physical examination of a positive BTxA injection.

3.3.6 Statistics

In all studies, $p < 0.05$ was considered to be statistically significant unless otherwise stated.

Study 1: Spatiotemporal Tracking of Bone Loss

For Study 1, we first determined the longitudinal location of acute endocortical bone loss initiation by performing a one-way ANOVA with Tukey post-hoc analysis with bin location as the independent factor and day 0 to day 6 endocortical expansion as the dependent variable. Once the endocortical bone loss initiation was identified in the metaphysis, we next analyzed if osteoclast activity migrated to the diaphysis. For this, we performed a univariate analysis of variance with diaphyseal bin location (Bins C-F) and scanning time periods as independent

factors and endocortical expansion as the dependent variable. TUKEY post-hoc analysis was performed where main effects achieved significance without significant main effect interactions.

Study 2: Spatial Initiation of Trabecular Bone Loss

For whole bone changes, a multivariate analysis of variance was performed with scanning time point (day following treatment) and treatment (BTxA versus saline) as independent factors and standard trabecular analysis metrics (e.g. BV, BV/TV, etc.) as the dependent variables. For tibial long-axis variations in bone loss in BTxA and saline treated mice, univariate analysis of variance was performed with location (Stack) and treatment (BTxA versus saline) as main effects and loss of trabecular bone volume as the dependent variable. To analyze focal changes in trabecular architecture, the calculated accuracy and precision of our image registration technique were used. Significant differences in percent misalignment within the IRV were determined using unpaired T-tests. Significant alterations in Element bone volume in the experimental groups were required to be greater than 3 standard deviations from the mean difference calculated in the Registration Control animals ($p<0.003$). This stringent threshold was used to minimize the potential for Type 1 error within the large number of comparisons between Elements (125 total Elements × 2 time points=250 total comparisons).

Study 3: Basal Cell Activity Modulates Bone Loss Initiation

To compare the baseline trabecular structure (day 0) in Young and Aged animals, a multivariate analysis of variance was performed with mouse age (Young vs. Aged) as the independent factor and standard trabecular analysis metrics (e.g. BV, BV/TV, etc.) as the dependent variables. To compare the osteoclast dynamics induced with the first 3 days

following muscle paralysis in Young and Aged animals, a multivariate analysis of variance was performed with mouse age (Young vs. Aged) as the independent factor and dynamic bone morphometry measures (BRR_{BV} and BRR_{BS}) as the dependent variables.

3.4 Results

3.4.1 Study 1: Spatiotemporal Tracking of Bone Loss

Following transient muscle paralysis, endocortical bone resorption in the proximal tibia metaphysis was distinct in both spatial distribution and timing compared to endocortical resorption in the diaphysis. During the first 6 days, 96.5% of observed endocortical bone loss occurred in the metaphyseal region of the scan volume (Fig. 3.2B). Specifically, post-hoc analysis determined that endocortical bone resorption focally initiated in the metaphysis nearest the growth plate, as endocortical expansion was significantly elevated in Bin A versus all other bins during the day 0 to day 6 time period (Fig. 3.2B, $p<0.001$).

Migration of the initial endocortical osteoclast response in the metaphysis was not supported by spatiotemporal analysis of endocortical expansion in the diaphysis. In contrast to the endocortical resorption in the metaphyseal region, diaphyseal bone loss was homogenously distributed across bins and occurred almost entirely between days 6 and 13 (81.3% of diaphyseal bone loss occurred within day 6 to day 13; Fig. 3.2C). Analysis of variance revealed a significant timepoint main effect on diaphyseal endocortical expansion following transient muscle paralysis, while location and location:timepoint interaction were not significant (Fig. 3.2C). Post-hoc analysis confirmed that endocortical bone loss in the diaphyseal bins (Bins C-F) was significantly elevated during the day 6 to day 13 period versus day 0 to day 6 and day 13 to day 20 periods (Fig. 3.2C, $p<0.01$).

3.4.2 Study 2: Spatial Initiation of Trabecular Bone Loss

Image registration was highly accurate within both the cortical IRV and the trabecular ROI (Fig. 3.3). The mean (± s.d.) percent misalignment within the IRV of Registration Controls was 2.0 ± 0.3%. Within the ROI, the average volumetric difference between Elements in the primary and registered secondary scan volumes of the Registration Controls was 2.3e3 ± 1.4e5 μm^3 (0.01 ± 0.44% when normalized to total Element volume). In the experimental groups, percent misalignment of the IRV was not significantly different in BTxA treated animals on day 2 or day 3 compared to Registration Controls (1.8 ± 0.1% and 2.1 ± 0.2%, respectively; $p>0.23$).

In BTxA treated animals, image registration allowed for detection of focal bone loss initiation at time points where bone resorption was undetectable using standard μCT analysis. Standard μCT analysis of un-registered whole trabecular morphology indicated that muscle paralysis did not alter any bone measurement within the analyzed trabecular bone volume of BTxA treated mice compared to Saline controls within 3 days of treatment (Table 3.1). When registered serial trabecular images were analyzed in longitudinal stacks (Fig. 3.4A), no significant bone volume differences could be identified on day 2 ($p>0.053$; Fig. 3.4B) or on day 3 ($p>0.132$; Fig. 3.4C). However, bone loss nearest the growth plate ($Stack^1$) in BTxA treated mice was 8.8-fold greater than in any other Stack analyzed (Fig. 3.4C-D).

Further increasing analysis resolution to the level of an individual Element allowed for statistically significant bone alterations to be identified in both BTxA and Saline mice. When quantified in three-dimensions (Fig. 3.5), observed patterns of bone loss in BTxA treated mice reflected an amplification of baseline resorptive events observed in saline treated mice. In saline treated animals, a single discretized element (from 125 total) demonstrated a significant decrease

in bone volume at both day 2 and day 3 when compared to day 0 bone volumes (Fig. 3.5A&C). Specifically, calculated bone volume decreased within Element^{3,4,1} from -8.0% on day 2 to -15.7% on day 3 (mean difference of intra-animals day 0 comparisons). In the BTxA treated group, Element^{3,4,1} was also the only element to demonstrate a significant decrease in bone volume at day 2 (-7.9% mean difference; Fig. 3.5B). Unlike the Saline treated group, the number of elements in which significant bone loss occurred expanded in BTxA treated mice by day 3. Seven discretized elements demonstrated significant bone loss (ranging from -7.2 to -31.4%, Fig. 3.5D) at day 3, of which five elements either included or were adjacent to Element^{3,4,1} (Fig. 3.5D).

3.4.3 Study 3: Basal Cell Activity Modulates Bone Loss Initiation

Osteoclastic resorption was more profound in the metaphysis of Young versus Aged mice following muscle paralysis. Baseline volumetric measures of metaphyseal trabecular bone did not differ between Young and Aged mice (BV: $p>0.98$, BV/TV: $p>0.45$; Table 3.2). However, the structural morphology of the trabecular bone clearly differed between Young and Aged animals. The trabeculae of Young animals were more numerous (Tb.N: $p<0.001$; Table 3.2) and densely packed (Tb.Sp: $p<0.001$; Table 3.2), but were thinner than the trabeculae of Aged mice (Tb.Th: $p<0.001$; Table 3,2). As a result, Young mice demonstrated a nearly two-fold greater bone surface than Aged animals (BS: $p<0.03$; Table 3.2).

μCT based dynamic bone resorption parameters, referent to trabecular morphology, enabled normalized comparison of the effect of acute osteoclastic activity induced following muscle paralysis in Young and Aged mice (Fig. 3.6A). BRR_{BV} in the 3 days following muscle paralysis was greater in Young versus Aged groups (13.05 ± 1.53 %/day vs. 2.15 ± 1.56 %/day,

$p<0.001$; Fig. 3.6B). Bone resorption rate normalized to bone surface (BRR_{BS}) was also significantly increased in Young versus Aged mice (2.27 ± 0.27 $\mu m^3/\mu m^2/day$ vs. 0.60 ± 0.44 $\mu m^3/\mu m^2/day$, $p=0.005$; Fig. 3.6C).

3.5 Discussion

Combining a μCT image registration strategy with an *in vivo* model of acutely induced osteoclastic resorption allowed us to explore, for the first time, the temporal and spatial relation of bone resorption in adjacent metaphyseal and diaphyseal compartments of the tibia. Consistent with our hypothesis, spatiotemporal tracking of compartmental bone loss identified conspicuous differences in both the timing and spatial distribution of osteoclastic resorption between the compartments. Endocortical bone loss was most rapidly initiated in the metaphyseal region following induction of muscle paralysis and, given its location, appeared to occur via amplification of baseline osteoclastic activity nearest to the growth plate. This conclusion was clarified by demonstrating that elevated basal osteoclastic resorption was associated with an enhanced magnitude of initial trabecular resorption. The absence of evidence suggesting osteoclast migration between the metaphysis and diaphysis, when combined with the temporal separation in the onset of resorption, suggests that the initiations of osteoclastic resorption in the two compartments are distinct cellular events.

As with any series of *in vivo* studies, our data should be considered in the context of the general limitations of the approaches we implemented. To determine whether bone loss in the metaphysis and diaphysis were distinct resorption events, we temporally tracked endocortical alterations in a scanned bone volume that encompassed both compartments. This approach differed from our previous studies (which investigated metaphyseal trabecular bone and a non-

contiguous volume of cortical bone in the diaphysis) and therefore allowed simultaneous assessment of osteoclastic activity across both compartments. Due to the large scan lengths (6.3 mm) and scan duration (≈ 1hour) required for Study 1, we were limited to three total *in vivo* scanning sessions to minimize the possible effects of both anesthesia and radiation exposure on bone cell activity [94]. For that reason, we chose equally spaced scanning time points (≈ 1/week) which encapsulated the initiation and peak resorption events previously observed separately in each compartment [49]. If osteoclasts were to have migrated from the location of bone loss initiation in the metaphysis to areas of temporally distinct bone loss in the diaphysis, we would have anticipated a location main effect or a timepoint:location interaction in the spatiotemporal analysis of the diaphysis (Fig. 3.2C). The lack of such findings suggests that metaphyseal and diaphyseal resorption are not connected through an expansive migratory response. As each scan is an individual 'snapshot' of bone resorption at a single moment in time, it is possible that our approach would be insensitive to extremely rapid or complex three-dimensional osteoclast migration. However, the speed at which active osteoclasts have been reported to migrate *in vivo* (≈ 0.28 mm/week; [117, 118]) would produce maximum weekly cell movements that were less than 50% of the bin lengths used in this experiment. Thus, individual osteoclasts would be unlikely to travel between non-adjacent bins within a single scanning time period.

Defining the focal initiation of trabecular resorption required development of a more spatially precise approach capable of separating induced osteoclast activity from baseline bone remodeling. This goal was accomplished through the application of serial μCT image registration, which requires the identification of invariant landmarks capable of defining accurate image superposition. However, such invariant landmarks are commonly lacking in models of

profound bone resorption [119]. For this reason, previous studies in models of bone tissue alteration have used operator-defined regions of interest and/or best-fit algorithms to enable alignment of μCT images across time [4, 68, 73, 120-122]. While these strategies have been successfully applied to qualitatively examine focal bone alterations in a variety of bone loss/bone formation models, quantitative assessment is difficult without a means to simultaneously quantify registration accuracy. By adapting our previous diaphyseal image registration paradigm [60], we created a novel strategy capable of tracking trabecular alterations using the morphologically quiescent (i.e., in acute time periods following muscle paralysis) mid-diaphysis as the registration landmark (Fig. 3.7). This refinement allowed us to quantify the accuracy of our image registration even in the presence of profound trabecular alterations, and thereby enabled identification of focal trabecular alterations in a model of profound osteoclastogenesis. The flexibility of this technique makes it applicable for high-resolution tracking of osteoclast (i.e., resorption) dynamics in any model in which an unaltered registration landmark is identifiable.

To begin to clarify distinctions between metaphyseal and diaphyseal bone resorption following muscle paralysis required mitigation of one potentially confounding difference in the manner these compartments are traditionally analyzed. Previous studies, including ours, generally focus on trabecular alterations within the metaphysis while quantifying cortical alteration at the diaphysis [11, 49, 65, 123]. However, given the relative differences in the surface area available for resorption and mineral density in these distinct bone tissues [124, 125], relating bone resorption (and thus osteoclast activity) between these compartments has been previously interpreted in the context of a perceived permissiveness of trabecular bone to resorption. When using endocortical expansion as a common measure of bone resorption

spanning the compartments, the data indicated that bone resorption was more acute and profound in the proximal metaphyseal compartment than in the adjacent diaphysis. While not contradicting the possibility of trabecular bone hyper-sensitivity to osteoclastic resorption, these data suggested that increased basal metabolic activity in the metaphyseal compartment might underlie why trabecular bone loss occurs more rapidly than cortical bone loss following muscle paralysis.

Subsequent studies identified a role of the basal cellular microenvironment in mediating the acute metaphyseal response following muscle paralysis. The resolution provided by three-dimensional examination of registered trabecular bone allowed for identification of focal bone alterations not identifiable by either traditional imaging based assessment (Table 3.1) or by dividing the metaphysis into five equal thickness stacks (Fig. 3.3). Using our novel image registration approach, we found that trabecular bone loss following calf paralysis was anatomically discrete and first occurred in areas also observed to have high basal levels of osteoclast activity (anterior portion immediately adjacent to the growth plate). As well, given the compatibility in timing and location of metaphyseal endocortical resorption in Study 1 and metaphyseal trabecular resorption in Study 2, it is likely that endocortical and trabecular resorption were a result of a single metaphyseal resorptive event. This finding suggests that the bone microenvironment (e.g., metaphyseal compartment) and not the perceived permissiveness of trabecular bone to resorption, may control the initial response of trabecular bone in many models of bone resorption.

Directly testing the hypothesis that growth plate bone cell dynamics mediates acute trabecular bone loss following muscle paralysis is inherently challenging. Both genetic (e.g., mouse strain; [126]) and epigenetic (e.g., mouse age, physical stimuli gain/loss; [127, 128])

factors alter bone cell activity in the growth plate/proximal metaphyseal region. However, these factors also inevitably alter the basal trabecular environment (as emphasized by our observation of a nearly two fold greater trabecular bone surface in Young vs. Aged animals despite nearly equivalent bone volume). As such, increased bone resorption following muscle paralysis in Young mice might occur either by increased osteoclastic activity or due to increased resorptive potential of the high surface area trabecular bone.

Despite these limitations, our final experiment provides *in vivo* support for the conclusions drawn from the initial experiments. The age of mice in the final experiment was chosen based on their clear differences in growth plate cellular activity [127]. To control for varied surface areas between groups, we utilized direct 3-D quantification of dynamic osteoclast activity via time-lapse μCT imaging [116]. We found that paralyzing the calf muscle of very young mice with high growth plate cellular activity induced a more profound acute trabecular bone loss response (both morphometrically and when osteoclast induced bone resorption was normalized to surface area) than in 13-month old animals in which longitudinal tibial growth had ceased [127]. While a number of additional factors could also contribute to this observation (e.g., osteoclast potential for resorption could differ with age, a role of altered osteoblastic activity), we believe these data clearly extend the data of the initial correlative experiments and represents an initial confirmation of our developing thesis that basal osteoclast activity, in part, mediates the magnitude and rate of acute trabecular bone resorption following transient muscle paralysis.

One explanation for the enhancement of bone resorption nearest the growth plate within just 3 days of muscle paralysis may be enhancement of RANKL signaling. In a previous study, we identified upregulation of RANKL positive cells throughout the growth plate in the week

following muscle paralysis [57]. Given the ability of RANKL signaling to both amplify and initiate osteoclastic activity, focal amplification (or initiation) of osteoclastic activity in these areas would not be surprising [129]. However, determining if this spatially discrete pattern of bone loss in the metaphysis arises solely from the amplification of normal growth plate osteoclast function or is further potentiated by activation of functionally distinct marrow populations within the trabecular microenvironment remains to be explored.

Following calf paralysis, diaphyseal bone resorption differed from metaphyseal resorption in both timing (predominantly between day 6 and day 13) and spatial homogeneity (i.e., does not initiate from a secondary foci and radiate from that point). Specifically, the timing of bone loss initiation in this diaphyseal compartment (day 6 at the earliest) coincides with the amount of time required to form osteoclasts from monocyte/macrophage precursors *in vitro* and *in vivo (*which is too slow to account for the onset of metaphyseal resorption [130, 131]). As such, osteoclastogenesis within the marrow cavity may drive a secondary wave of bone resorption in the diaphysis in a manner distinct from the enhanced basal osteoclast activity observed in the metaphysis.

Though we believe our data suggests that functionally distinct upregulation of osteoclast activity in the metaphysis and the diaphysis are the likely causes of bone resorption following muscle paralysis, the role of altered osteoblast activity in this process was no specifically addressed. Given the role of osteoblast activity in models of disuse [132, 133], it is possible that decreased bone formation has an effect on the magnitude of bone loss in the metaphyseal or diaphyseal compartments. This is especially pertinent when considering that the origins of the paralyzed soleus muscle in our model of calf paralysis spatially correspond to the metaphyseal region in which bone resorption was most profound. However, our own recent studies have

demonstrated that direct inhibition of osteoclastogenesis via induced NFATc deletion completely inhibits bone loss following muscle paralysis [57]. As well, rather than acute loss of osteoblast function in the actively remodeling growth plate region, our registered imaging approach in Study 2 actually suggested a non-significant increase in osteoblast function in the 3 days immediately following paralysis. This coupled with the unchanged diaphyseal bone volume needed to accurately register the bone suggests that within the first 3 days following muscle paralysis osteoblast function is not materially altered in the metaphyseal or diaphyseal compartments. That said, the long term effects of muscle paralysis on osteoblast function, if any, remain to be resolved [49, 134, 135].

Taken together, our data suggests that tibial metaphyseal and diaphyseal bone loss induced by transient calf paralysis are spatially and temporally discrete events whose magnitude and location are influenced by basal bone cell activity. Initial bone resorption following paralysis was likely achieved through an increase in basal osteoclast activity within the proximal tibia metaphysis, while profound *de novo* osteoclastogenesis within the marrow may be the predominant mechanism driving resorption in the diaphysis. In addition, we found that mouse age can affect the dynamics of this induced bone resorption by reducing the magnitude of bone loss initiation in the metaphysis. These results highlight the importance of understanding the basal bone resorption dynamics when the skeleton is catabolically challenged, as the relative susceptibility of a given compartment or bone type (cortical versus trabecular) may be dependent on a variety of external factors. In conclusion, we believe that extension of the imaging approach we have developed and implemented holds potential to clarify the differing signaling mechanisms that may underlie osteoclastogenesis in different bone compartments induced by a variety of neuromuscular trauma.

3.6 Further Defining the Mechanisms of Muscle Paralysis Induced Bone Loss

The above studies furthered our understanding of the mechanisms involved in mediating bone loss following transient paralysis. Specifically, we have now determined that metaphyseal bone loss initiation begins within 3 days of transient muscle paralysis as a result of enhanced activity of native osteoclasts near the growth plate. The location and timing are consistent with our previous hypothesis that neuronal mediated RANKL production observed at the growth plate activates osteoclastic resorption (Fig. 3.8). Further, the identification of a separate osteoclastic resorption event likely a result of *de novo* osteoclastogenesis advanced our hypothesis of osteoclast activation in this model. As such, the main focus of Chapter 4 is to determine if inflammatory mechanisms within the bone marrow modulate osteoclastogenesis and bone resorption following muscle paralysis (Fig. 3.8).

Table 3.1: μCT Outcome Measures for Study 2 [mean ± s.e.]

		Day 0	Day 2	Day 3
Endocortical volume, Ec.Vol or TV (mm^3)	Botox	1.991 ± 0.066	1.992 ± 0.075	2.017 ± 0.073
	Saline	1.999 ± 0.068	2.008 ± 0.075	1.995 ± 0.074
Trabecular fraction. BV/TV (%)	Botox	14.048 ± 0.632	14.045 ± 0.525	13.660 ± 0.536
	Saline	13.203 ± 0.957	13.337 ± 0.992	13.330 ± 0.998
Trabecular number, Tb.N (#/mm)	Botox	3.656 ± 0.122	3.673 ± 0.110	3.654 ± 0.117
	Saline	3.636 ± 0.236	3.527 ± 0.235	3.485 ± 0.237
Trabecular thickness, Tb.Th (mm)	Botox	0.059 ± 0.001	0.059 ± 0.001	0.058 ± 0.001
	Saline	0.059 ± 0.001	0.060 ± 0.001	0.060 ± 0.001
Trabecular spacing, Tb.Sp (mm)	Botox	0.268 ± 0.011	0.266 ± 0.009	0.269 ± 0.010
	Saline	0.274 ± 0.017	0.281 ± 0.017	0.288 ± 0.018

No significant differences in main effects of scanning time points ($p>0.998$), treatment ($p>0.053$) and time point:treatment ($p>0.874$)

Table 3.2: μCT Measures of Initial Trabecular Morphology for Study 3 [mean ± s.e]

		Day 0
Trabecular bone volume, BV (mm^3)	Young	0.163 ± 0.017
	Aged	0.161 ± 0.039
Trabecular fraction. BV/TV (%)	Young	10.650 ± 0.780
	Aged	9.297 ± 1.532
Trabecular number, Tb.N (#/mm)	Young	4.350 ± 0.114 *
	Aged	2.341 ± 0.076
Trabecular thickness, Tb.Th (mm)	Young	0.043 ± 0.001 *
	Aged	0.075 ± 0.003
Trabecular spacing, Tb.Sp (mm)	Young	0.230 ± 0.007 *
	Aged	0.443 ± 0.020
Trabecular bone surface, BS (mm^2)	Young	9.372 ± 0.898 *
	Aged	5.565 ± 5.371

* (all $p<0.03$)

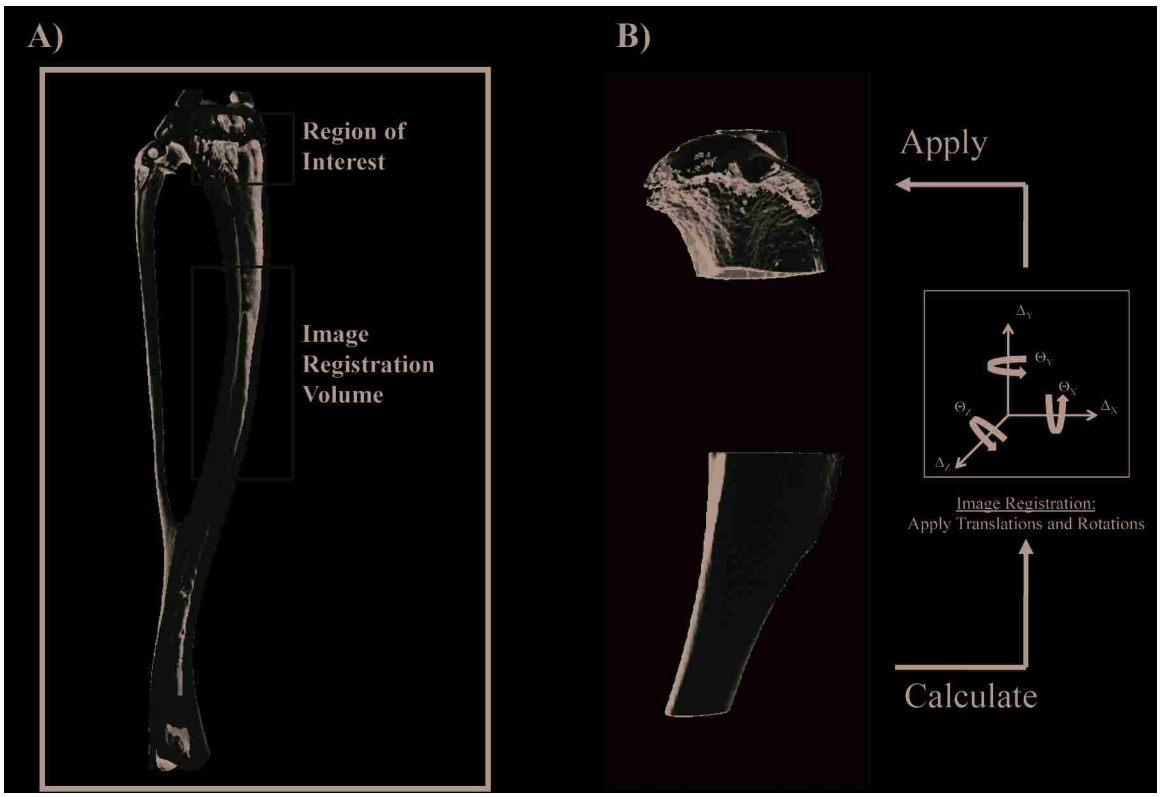

Figure 3.1: Trabecular Image Registration Algorithm
Trabecular image registration within the metabolically active metaphysis was achieved through coupling with image registration in the unchanged diaphysis. After obtaining two non-contiguous scan volumes within a single scanning session (A), rotational and translational parameters were defined by spatially registering the volumetrically identical IRVs and then applied to the ROI volumes. This approach enabled unbiased superimposing of the trabecular compartment despite the potential for morphologic alteration on any bone surfaces (B).

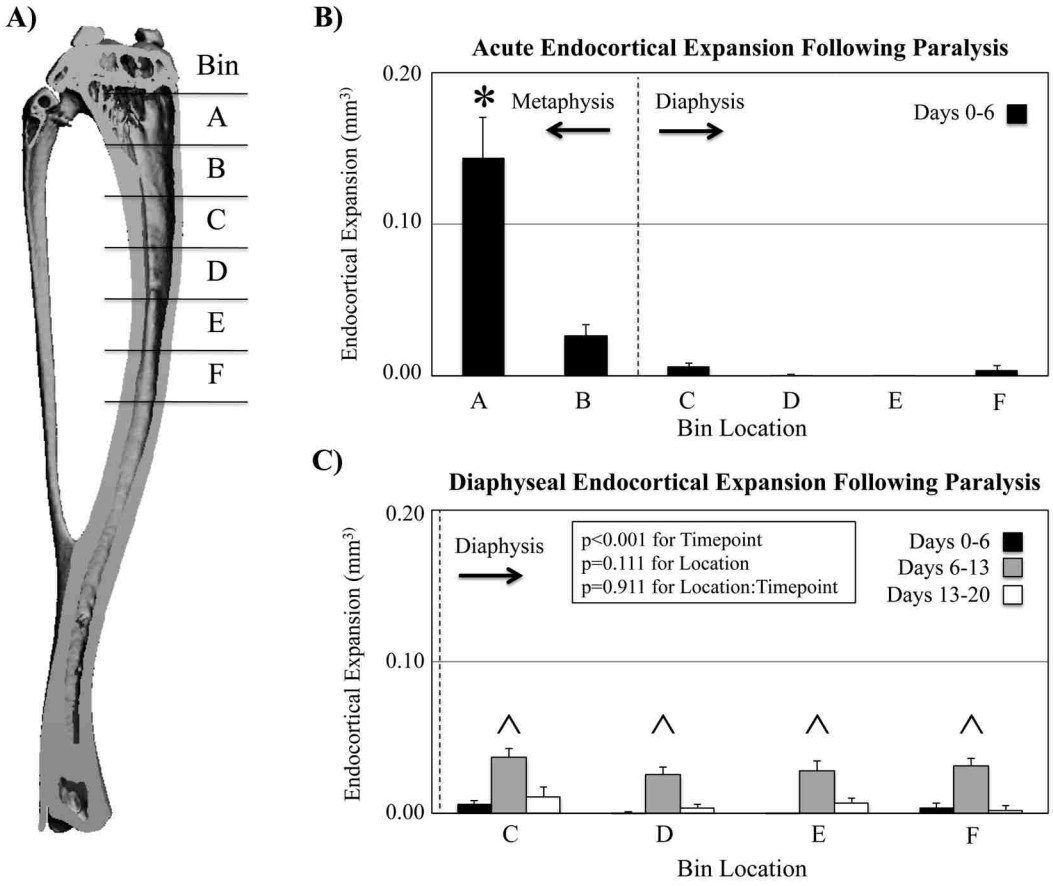

Figure 3.2: Spatiotemporal Tracking of Compartmental Bone Loss
Endocortical bone resorption in the metaphysis and diaphysis following transient muscle paralysis had distinct spatial and temporal patterns. Resorptive activity within the tibia following transient muscle paralysis was quantified in each of six discrete bins (A) over a near three week time period. The initiation of endocortical expansion (mean ± s.e.) occurred exclusively within the metaphysis (B). Within the first 6 days following muscle paralysis, endocortical expansion was focused nearest the growth plate (2B, * significantly different from Bins B-F at same time point, all $p<0.001$). The resorptive initiation in the metaphysis did not migrate to the diaphysis. (C). Instead, diaphyseal expansion occurred homogeneously in the day 6 to 13 time period (C, ^ significantly greater than the day 0 to 6 and day 13 to 20 time periods at each bin location, all $p<0.01$) and lacked a significant main effect of location or significant location:timepoint interaction.

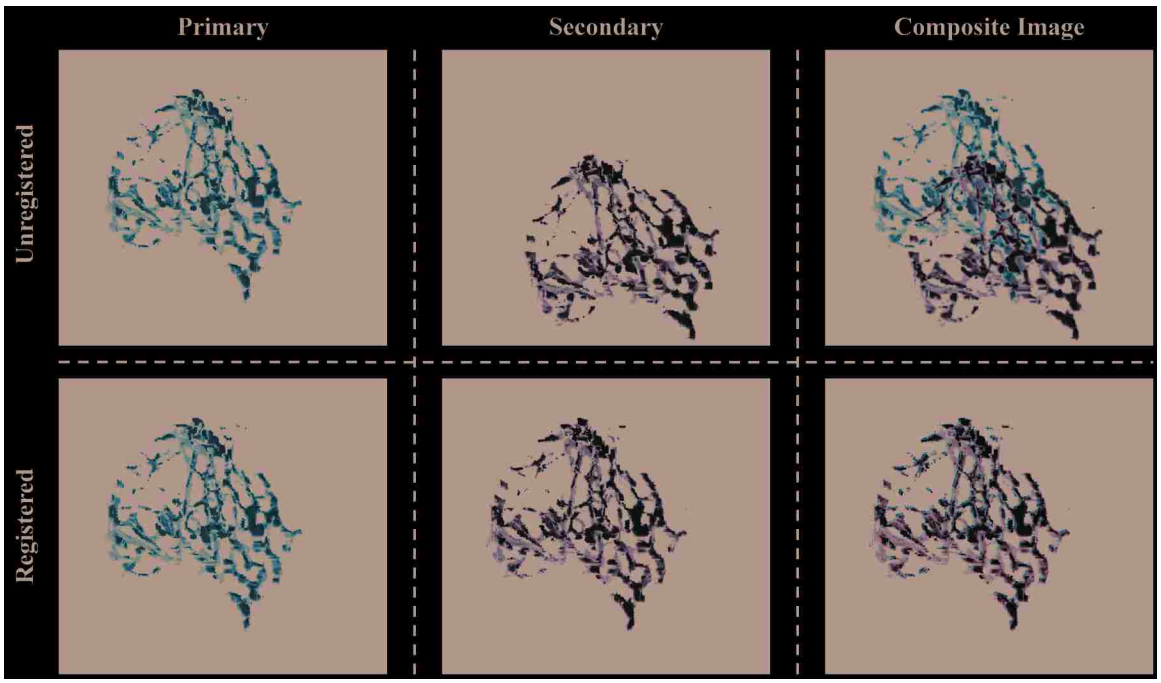

Figure 3.3: Trabecular Image Registration Control
Composite images of volumetrically identical primary (red) and secondary (yellow) ROI scans. Image registration greatly enhances the spatial alignment (green) of serial scans, which is necessary to idenify bone alteration.

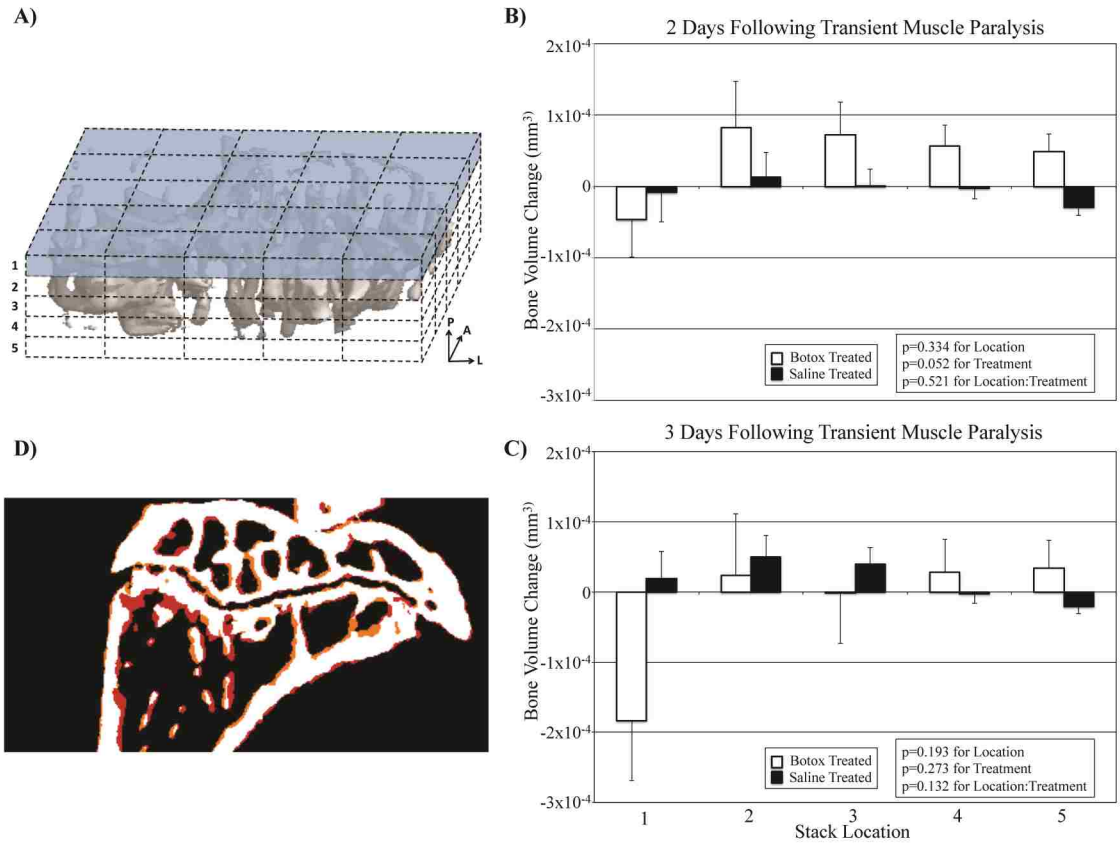

Figure 3.4: Initiation of Bone Loss Adjacent to Proximal Growth Plate
Separating the metaphysis into equal-volume longitudinal stacks does not provide sufficient resolution to identify focal bone loss initiation in the proximal metaphysis. Bone volume alterations in registered and discretized trabecular bone volumes were first analyzed in layers of Elements (i.e., Stacks) perpendicular to the growth plate (A, Stack[1] highlighted in blue). There was no significant difference in bone alterations at any location or across treatment groups within 2 (B) or 3 days (C), though in both cases the greatest bone loss was adjacent to the growth plate in BTxA treated animals. However, a representative coronal composite cross-section 3 days following BTxA treatment suggests that bone loss occurred most predominately nearest the growth plate (D, Red=Bone Loss, Orange=Bone Formation).

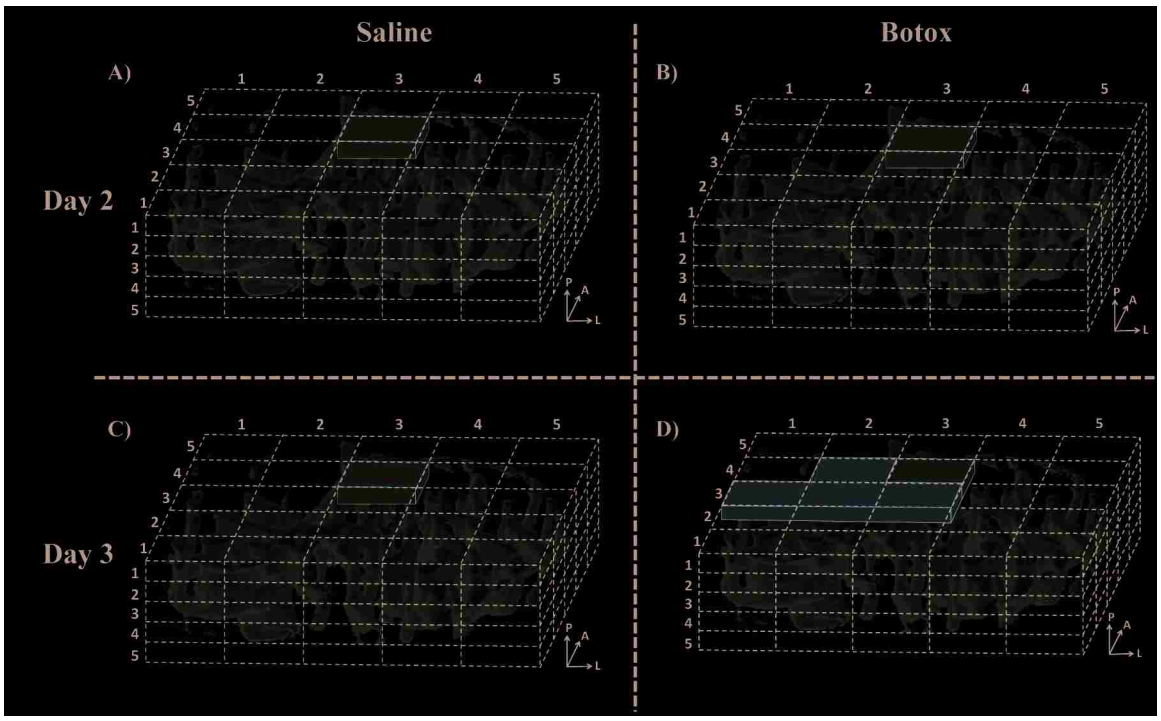

Figure 3.5: Focal Bone Loss Initiation in Areas of High Basal Osteoclast Activity
Metaphyseal trabecular bone resorption following transient muscle paralysis initiated in locations of high basal osteoclast activity nearest the growth plate. In both Saline and BTxA treated mice, significant bone loss occurred in Element[3,4,1] by day 2 (A-B, light red). Unlike the Saline group where the bone loss pattern was consistent across day 2 and day 3 (C), significant bone loss expanded to adjacent bins in BTxA treated mice by day 3 (D, dark red).

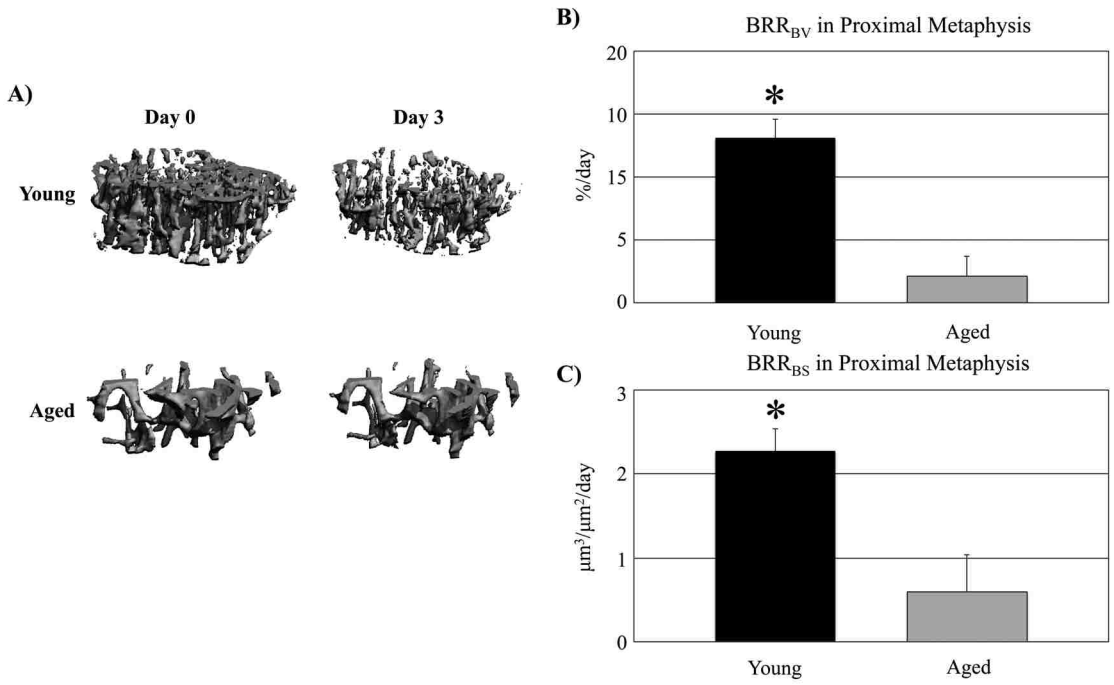

Figure 3.6: Trabecular Bone Loss Initiation in Young and Aged Mice
The rate of acute metaphyseal bone resorption following transient muscle paralysis varied between Young and Aged mice independent of trabecular morphology. Serial μCT imaging of the proximal tibia metaphysis (A) enabled quantification of dynamic bone morphology measures normalized to either bone volume or bone surface. Within the first 3 days following muscle paralysis, the Bone Resorption Rate per initial bone volume (BRR_{BV}) was significantly greater in Young versus Aged mice (B, * $P<0.001$). When normalized to initial bone surface, Bone Resorption Rate (BRR_{BS}) was also significantly elevated in Young versus Aged mice (C, * $P<0.005$).

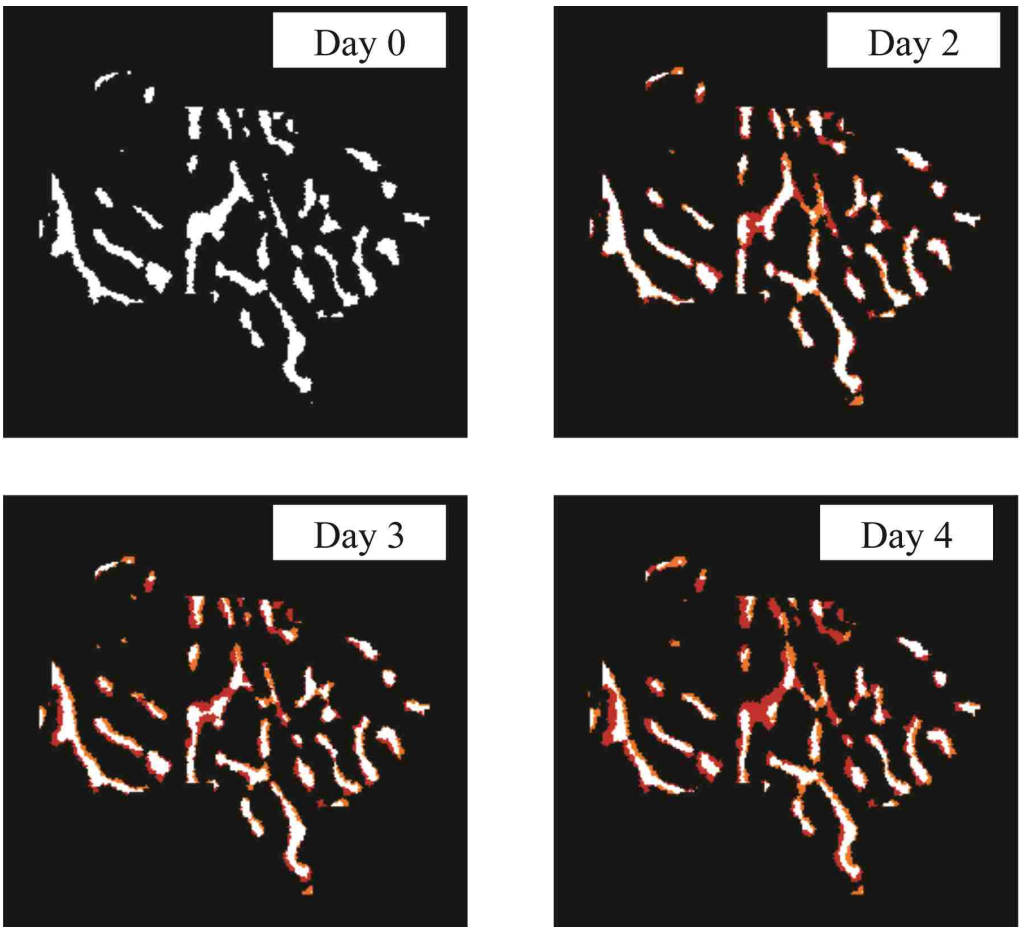

Figure 3.7: Temporal Trabecular Bone Loss in a Single BTxA Treated Mouse
Using the image registration approach, we are able to track animal specific focal trabecular bone loss. The above composite transverse images give a time-lapse picture of the 4 day progression of bone loss (red) near the growth plate in mice treated with BTxA (orange-bone formation).

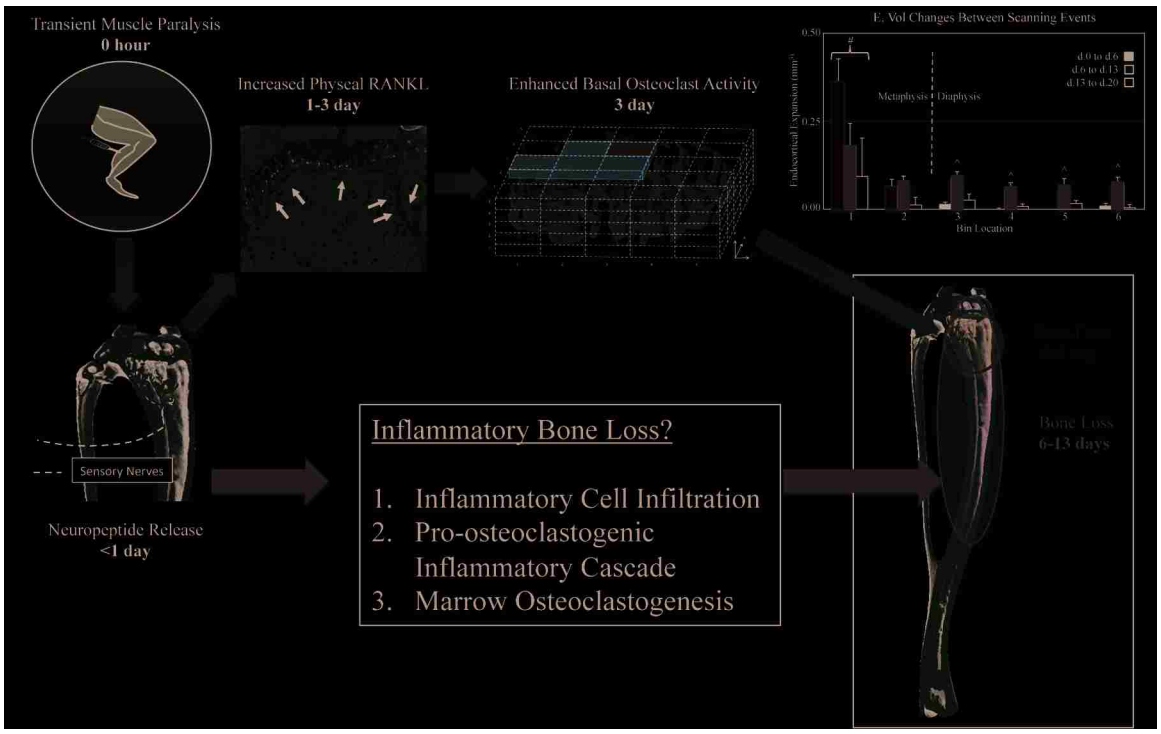

Figure 3.8: Updated Understanding of Transient Muscle Parlysis Induced Bone Loss
The spatiotemporal analysis of bone loss (top right) and trabecular image registration in this chapter have clarified our hypothesis of how bone loss following muscle parlaysis is induced. Specifically, we now believe that acute trabecular bone loss is induced through RANKL mediated enhanced osteoclastic activity at the growth plate (blue arrows). The timing and distribution of bone loss in the diaphysis suggests *de novo* osteoclastogenesis that is potentially driven through neuronal mediated inflammation (green arrows). Chapter 4 aims to identify the temporal progression of inflammatory bone loss in the tibia marrow following paralysis (black box).

Chapter 4: Muscle Paralysis Induces Acute Bone Marrow Inflammation and Predisposition to Formation of Giant Osteoclasts

4.1 Abstract

Inflammatory cascades are capable of profoundly altering bone cell activity. Given that cells of the immune system originate in bone marrow niches adjacent to bone cells, inflammatory activation in marrow holds potential to drive alteration of bone tissue in a variety of bone loss pathologies. Here we explored if bone marrow inflammation mediates the profound bone loss observed in a mouse model of transient muscle paralysis. Specifically, transient paralysis of the murine calf muscles induces rapid bone resorption in the medullary cavity of the adjacent tibia. Given our recent insights into the spatiotemporal bone loss dynamics in this model, we hypothesized that transient muscle paralysis induces tibia bone marrow inflammation resulting in enhanced bone marrow osteoclastogenesis. To test this hypothesis, we determined if inflammatory cell infiltration, pro-osteoclastogenic inflammatory gene expression and permissiveness to osteoclastogenesis in the bone marrow occurred in a manner temporally consistent with mediating bone loss in this model. We next explored if suppression of the inflammatory pathway, through genetic T cell diminishment or pharmacologic TNFα inhibition, could mitigate bone resorption following calf paralysis. Our findings identified inflammatory cell infiltration within 24 hours following muscle paralysis via significant alterations in T cell populations in the marrow of the proximal tibia metaphysis. As well, pro-osteoclastic gene expression throughout the tibia marrow was upregulated within 72 hours. This timing coincided with a shift in bone marrow permissiveness to osteoclastogenesis. Surprisingly, bone marrow obtained 72 hours following muscle paralysis was not predisposed to generate greater numbers of osteoclast, but rather highly fused giant osteoclasts. Though these findings were consistent

with inflammatory mediated bone loss, genetic and pharmacologic suppression of inflammatory pathways were not sufficient to mitigate the bone resorption in this model. Taken together, our data suggests that transient muscle paralysis induces an inflammatory cascade capable of modulating bone cell activity. However, our inability to block bone resorption through disruption of the inflammatory pathway may suggest our treatments lacked the capacity to alter the formation of giant osteoclasts initiated within 3 days following muscle paralysis.

4.2 Introduction

Normal bone homeostasis is maintained through the synchronized action of osteoclasts and osteoblasts in and around bone marrow. The function of bone marrow to facilitate normal bone remodeling derives in part to its adjacency to trabecular and endocortical bone surfaces and its vast reserves of bone cell precursors. However the function of bone marrow is multifaceted and merely includes control of bone cell dynamics. For example, bone marrow actively regulates immune response primarily through production and trafficking of both lymphatic and myeloid cells. Given that these immune cells have also been shown to have regulatory control over osteoclast activity [24, 136-138], inflammatory alterations in the marrow hold potential to create permissive osteoclastogenic environments.

Predisposition to bone loss and osteoporotic fracture is observed in a number of chronic inflammatory diseases such as rheumatoid arthritis, inflammatory bowel disease, chronic obstructive pulmonary disease, and multiple sclerosis [139-142]. Inflammatory pathways have also been implicated in post-menopausal bone loss [43]. When inflammatory disorders occur adjacent to bone surfaces (e.g., periodontitis or adjuvant arthritis), bone resorption is especially destructive [143, 144]. One reason for this is that receptor activator of nuclear factor kappa-B

ligand (RANKL), the essential regulator of osteoclastogenesis, can be highly expressed on activated CD4+ T cells and other inflammatory and inflammatory regulating cells [145-147]. As well, other inflammatory cytokines such as TNFα, IL-1 and IL-6 have been shown to promote osteoclastogenesis in permissive environments [144, 148]. Demonstrating that the immune system also modulates bone resorption, both pharmacologic and genetic disrupting of the immune response through T cell depletion and/or anti-inflammatory treatment has been shown to reduce bone loss in models of OVX and adjuvant arthritis [43, 149, 150].

Given immune control of bone cells, any model in which bone resorption occurs predominately adjacent to the immune cell rich bone marrow holds potential to be inflammatory mediated. One such example is our mouse model in which transient paralysis of the calf muscle group induces profound bone resorption within the medullary cavity of the adjacent tibia. Initially thought to be a model of mechanical unloading engendered bone loss, muscle paralysis induces bone resorption disproportional to the mild gait defect observed in this model [53, 78]. While this finding is inconsistent with a disuse bone loss phenotype, many recent observation of this model are consistent with the hallmarks of inflammatory bone loss. Specifically, bone loss following muscle paralysis is a result of RANKL mediated osteoclastogenesis [57]. Preliminary studies have also observed acute upregulation of the osteoinflammatory cytokines TNFα and IL-1 in the bone marrow following muscle paralysis [151], both of which are known to have a synergistic effect on RANKL induced osteoclastogenesis [38, 152]. In our most recent study, we have identified a secondary resorptive event following paralysis that is both spatially and temporally consistent with our preliminary inflammatory cytokine expression.

Using novel image registration techniques, we have previously determined the temporal and spatial nature of bone loss following muscle paralysis. Specifically, trabecular bone loss in

the proximal tibia metaphysis initiates within three days of muscle paralysis, likely mediated by basal growth plate cell dynamics [61]. A spatiotemporally discrete resorption event occurs on the endocortical surface of the tibia diaphysis predominately with 6 to 13 days following muscle paralysis [61]. The timing of this secondary bone resorption is consistent with *de novo* osteoclastogenesis, as opposed to the initial wave of resorption in the proximal metaphysis, which is too rapid for this process [130, 131]. Given that this osteoclastogenesis is confined to a single bone within a small window of time, we speculated that causal osteoinflammatory bone marrow alterations, if present, could be identified by their temporal signature. Given our preliminary data suggesting upregulation of osteoinflammatory cytokines within the marrow, we hypothesized that transient muscle paralysis induces tibia bone marrow inflammation resulting in enhanced bone marrow osteoclastogenesis.

To test this hypothesis, we first determined if specific T cell subsets, previously identified as mediators of inflammatory bone loss, were expanded in the marrow prior to bone loss initiation. Once this was confirmed, we tested if mice with genetic deficiency in T cells would have a muted bone loss response to transient muscle paralysis. As these data indicated that T cells were not primarily mediating osteoclastogenesis following paralysis, we next performed a broader investigation of inflammatory and osteoclastogenic alteration within the marrow. Specifically, we tested the temporal nature of osteoinflammatory gene expression within the tibia marrow along with the temporal alterations of the marrow permissiveness to osteoclastogenesis. Given these data, we performed a final experiment in which we attempted to block bone resorption following muscle paralysis with a pharmacologic inhibitor of TNFα, a master regulator of inflammation.

4.3 Methods

This study was comprised of five complementary *in vivo/in vitro* experiments. With the exception of the T cell knockout study, as noted below, all mice were 16-wk-old female C57Bl/6 obtained from Jackson Laboratories. Each experiment utilized a single injection of botulinum toxin A (BTxA; 2U/100 g body weight; Allergan, Irvine, CA, USA) into the right calf muscle group to induce transient muscle paralysis [49]. Mice receiving BTxA treatment were allowed free cage activity for the remainder of each experiment. Calf paralysis was confirmed 24 hours post-injection by visual examination of reduced toe extension and ankle plantarflexion in the affected limb. All experiments were performed in accordance with protocols approved by the Institutional Animal Care and Use Committee, University of Washington.

4.3.1 Flow Cytometric Analysis of Bone Marrow

Mice (n=5) received a BTxA injection in their right calf and were euthanized 24 hours later. Marrow within the proximal metaphysis of the right tibia was flushed with RPMI, centrifuged and the supernatant removed. The cell population was then lysed of red blood cells by incubation in 750 µl of ACK lysing buffer for 2 minutes. Once the lysing buffer was removed, cells were resuspended in RPMI and aliquoted into FACS tubes ($5X10^6$ cells per sample). FACS samples were centrifuged, the supernatant removed and resuspended in 100 µl surface antibody dilution (1:200 ratio of surface antibody to FACS buffer consisting of HBSS with 2% FBS) for 20 minutes at 4 degrees. Marrow cell populations were stained for T cell markers using anti-TCRβ, -CD4 and -CD8 antibodies (Biolegend). Finally, samples were washed twice with FACS buffer and resuspended in 200 µl FACS buffer for flow cytometry analysis. Individual sample data were acquired on LSRII flow cytometers (BD Biosciences) and

analyzed using FlowJo software (Treestar). Marrow from naïve mice (n=5) was identically collected and served as baseline controls. Prior to analysis, one mouse from the BTxA group was removed due to a failed physical examination for muscle paralysis.

4.3.2 Muscle Paralysis Induced Bone Loss in TCRβδKO Mice.

A group of female TCRβδKO mice deficient of αβ+ and ϒδ+ T cells (B6.129P2-Tcrbtm1Mom Tcrdtm1Mom/J purchased from Jackson Laboratories, n=7; [153]) and WT counterparts (C57Bl6/J, n=5) received a BTxA injection in the right calf on day 0. High-resolution μCT images of the right tibia metaphysis (encompassing 0.85 mm of the proximal tibia metaphysis immediately distal to the growth plate) were obtained on day 0, 5, 12 and upon sacrifice on day 22 (Scanco μCT 40; 10.5 μm voxel size, 55 kVp, 145 μA). To limit radiation exposure, *ex vivo* diaphyseal scans (1.00 mm of the tibia midshaft starting 1.25 mm proximal of tib-fib junction) of the right (Experimental) and left (Contralateral) tibias were obtained post-sacrifice in the TCRβδKO mice.

Image analysis was performed as in previous studies [49]. All raw μCT image data were preprocessed using a Gaussian Filter algorithm to remove image noise (Sigma = 1.2, Support = 2.0) followed by bone segmentation within the scan volume using standard image thresholding techniques. A threshold of 705.97 mg HA/cm^3 was used for bone tissue identification and was verified through manual investigation of grayscale images. Trabecular alterations in the metaphyseal scans and cortical alterations in the diaphyseal scans were analyzed using standard μCT analysis measures. Metaphyseal analysis included quantification of endocortical volume (Ec.Vol or TV), trabecular bone volume (BV), trabecular fraction (BV/TV), trabecular number (Tb.N), trabecular thickness (Tb.Th) and trabecular separation

(Tb.Sp), while diaphyseal analysis included periosteal volume (Ps.Vol), cortical volume (Ct.Vol) and endocortical volume (Ec.Vol).

4.3.3 Quantitative RT-PCR

Mice in this study were sacrificed on day 1, 3 or 7 post BTxA injection (n=6/group). Post sacrifice, whole marrow was flushed from the right tibiae. For quantitative RT-PCR, total RNA was extracted using the RNeasy Mini Kit (Qiagen) according to manufacturer's protocol and cDNA synthesized using Super Script III reverse transcriptase (Invitrogen). cDNA from marrow of treatment Naïve mice (n=6) was prepared identically and served as controls. We analyzed inflammatory and osteoclastogenic gene expression with quantitative real-time PCR using SYBR green and the Applied Biosystems 7900 HT sequence detection system (Table 4.1). Gene expression levels were quantified using the 2-(2DDCT) method relative to the inflammatory specific housekeeping gene HPRT [154].

4.3.4 Primary Osteoclast Culture

Tissue culture medium and supplements were purchased from Invitrogen (Life Technologies. Media was supplemented with heat inactivated FBS (HyClone, Thermo Scientific). Marrow was collected from mouse tibiae at 1, 3 and 7 days post BTxA injection (n=2group). Marrow was flushed in culture medium (α-MEM with 10% FBS) and red blood cells lysed as previously described. Cells were seeded at 1.5 x $10^4/cm^2$ in chamber well slides (Thermo Scientific Inc.), supplemented with 50 ng/ml M-CSF and 10 ng/ml RANKL and incubated at 37°C and 5% CO_2. Cell media was refreshed on day 3 of culture and cells fixed and stained for tartrate resistant acid phosphatase (TRAP) on day 8 of culture using the Leukocyte

(TRAP) kit and protocol (Sigma-Aldrich). The experiment was replicated (total combined group size of n=4/group), with data normalized within each experiment to identically treated marrow from treatment naïve mice (n=2/exp). For each group, normal osteoclasts (i.e., TRAP-positive cells w/ 3+ nuclei) and giant osteoclasts (i.e., TRAP-positive cells w/ 20+ nuclei) were quantified on a per well basis using bright field microscopy (Olympus BH2 microscope, 10-40X magnification).

4.3.5 Muscle Paralysis Induced Bone Loss Following TNF Inhibition

Murine p75-FC fusion protein (Amgen), a murine analog to the fusion protein etanercept, was used as an injectable TNFα inhibitor in this study [155]. Thirty-two mice were randomized into 4 treatment groups: Saline, BTxA, Saline + p75-FC fusion protein, and BTxA + p75-FC fusion protein. p75-FC was mixed in injectable phosphate-buffered saline (PBS) at a concentration of 1 mg/ml and administered subcutaneously at a maximum safe dose of 10 mg/ml every four days (beginning on day -4) [155]. On day 0, mice received either a BTxA or saline injection followed immediately by μCT scans on the proximal metaphysis and mid-diaphysis of the right tibia as described previously. Subsequent scans were obtained on day 12. Image analysis was performed identically to that describe in the TCRβδKO study.

4.3.6 Statistical Analysis

Multivariate (or univariate) analysis of variance was performed on all data from the flow cytometry and TCRβδKO studies. When significant main effect interactions were determined, pairwise comparisons with Tukey post-hoc analysis were performed. Differential gene regulation in the quantitative RT-PCR study was determined using planned comparison (i.e.,

gene expression on all days compared to Naïve mice) one-way ANOVAs with Fisher LSD post-hoc analysis. Finally, multiple one-way ANOVAs with Tukey post-hoc analysis were used to determine significant differences in the primary osteoclast culture and TNF inhibition data.

4.4 Results

4.4.1 CD4+ T Cells Are Acutely Expanded Following Muscle Paralysis

Flow cytometry revealed rapid alterations in tibia marrow cell populations in the proximal tibia metaphysis following muscle paralysis (Fig. 4.1). The percentage of CD4+ T cells within the bone marrow was elevated 25% within 24 hours of BTxA injection (1.47 ± 0.07% versus 1.14 ± 0.10% in Day 1 versus Naïve, respectively, $p<0.04$; Fig. 4.1B). However, CD8+ populations were not significantly altered within 24 hours (2.36 ± 0.21% versus 2.52 ± 0.35 in Day 1 versus Naïve, respectively, $p=0.71$; Fig. 4.1C). These alterations resulted in a significant increase in the ratio of CD4+/CD8+ T cells within the marrow (0.63 ± 0.04 versus 0.47 ± 0.04 in Day 1 versus Naïve, respectively, $p<0.03$; Fig. 4.1D). The overall T cell populations were not significantly altered (42.40 ± 2.91% versus 40.17 ± 1.78% in Day 1 versus Naïve, respectively, $p=0.54$; Fig. 4.1E).

4.4.2 T cell Deficiency Does Not Alter Bone Loss Following Muscle Paralysis

Given that T cell alterations were temporally consistent with bone loss induced by muscle paralysis, we explored whether mice with a TCRβδ deficit would demonstrate reduced bone loss following muscle paralysis. Baseline μCT imaging of the proximal tibia metaphysis (day 0) indicated that a subtle morphological phenotype was evident in TCRβδKO mice. While BV/TV, BV, Tb.N, and Tb.Sp were not significantly different compared to C57Bl/6 controls (Table 4.2),

Ec.Vol was decreased 12.8% and Tb.Th was elevated 4.6% in TCRβδKO mice (both $p<0.05$; Table 4.2). For that reason, traditional comparisons of BV/TV changes were used to detect differences in metaphyseal alterations between genotypes. Diaphyseal bone loss was determined by comparing experimental versus contralateral bone volumes in TCRβδKO mice only. For that reason, morphologic phenotyping at the diaphysis was not necessary.

T cell deficiency did not mitigate the overall magnitude of bone loss induced in the metaphysis following transient muscle paralysis. Analysis of variance revealed a significant timepoint main effect and timepoint:genotype interaction, but indicated that the genotype main effect was not significant. Post-hoc analysis confirmed that the magnitude of bone loss initiation on day 5 was significantly greater in TCRβδKO than in WT controls (-39.83 ± 2.76% versus -28.11 ± 2.66%, respectively, $p<0.04$; Fig. 4.2), while no significant differences could be detected between groups on day 12 (-78.85 ± 1.46% versus -87.39 ± 1.90%, $p>0.25$; Fig. 4.2) or day 22 (-70.65 ± 2.67% versus -80.15 ± 3.75%, $p>0.16$; Fig. 4.2). As well, *ex vivo* imaging of the tibia mid-diaphysis in the TCRβδKO mice identified significantly less cortical volume in the experimental versus contralateral limb (Table 4.3). This resulted from significant endocortical expansion (6.8% increase in Ec.Vol in Experimental versus Contralateral limbs, Table 4.3) without periosteal volume alterations (Table 4.3), a hallmark of cortical resorption in C57 mice exposed to muscle paralysis.

4.4.3 Inflammatory and Osteoclastogenic Genes Are Acutely Upregulated Following Muscle Paralysis

Temporal gene expression patterns within the whole tibia following muscle paralysis were consistent with inflammatory mediated osteoclastic pathway induction occurring by day 3

(Table 4.4). While none of the panel of 13 genes was significantly regulated 1 day following muscle paralysis (compared to Naïve controls), eight genes showed statistically significant regulation by day 3. Six genes were upregulated (TNF: 299%, DC-STAMP: 344%, OS-STAMP: 318%, IL-4: 243%, RANKL: 173% and OPG 321%, Table 4.4), while two were downregulated (CD44: -87%, and CD47: -88%, Table 4.4). Of these, only IL-4 remained significantly upregulated on day 7 (250%, Table 4.4). Additionally, another three genes (CD9, IL-1a and IL-1b; Table 4.4) became undetectable on day 3, and remained so on day 7, suggesting a potential downregulation over this time period. Of note, IL-6 gene expression was assayed but levels were undetectable in most samples and thus not reported.

4.4.4 The Osteoclastogenic Potential of Bone Marrow Is Altered by Muscle Paralysis

Temporally consistent with the gene expression alterations, the osteoclastic potential of the bone marrow was itself altered by day 3. Under the described culture conditions, marrow from naïve mice generated 96.75 ± 26.71 (mean ± s.e.) normal osteoclasts/well, which included 2.50 ± 0.96 giant osteoclasts/well (Fig. 4.3). Transient muscle paralysis did not alter the number of normal osteoclasts formed in marrow culture at any time point post-paralysis (Fig. 4.4A). In fact, there were non-significant decreases in normal osteoclast number at all post paralysis time points compared to naïve control cultures (range 13 to 41% decrease compared to naïve). However, the capacity to form giant osteoclasts was acutely upregulated 3 days following muscle paralysis, but returned to normal by day 7. Marrow harvested 3 days after BTxA injection produced 3.7 ± 0.5 times more giant osteoclasts than naïve control marrow (Fig. 4.4B, also significantly greater than Day 1 group).

4.4.5 TNF Inhibition Does Not Mute Bone Loss Following Muscle Paralysis

Prophylactic TNFα inhibition did not have a significant effect on the bone loss within 12 days following muscle paralysis. Within the trabecular bone of the proximal tibia metaphysis, there was no significant difference in BV/TV changes in BTxA mice with or without p75-FC treatment (-66.38 ± 3.47% versus -68.40 ± 1.98%, respectively, p=0.99; Fig. 4.5A). BV/TV alterations in these groups were significantly greater than in Saline animals with or without p75-FC treatment (-12.93 ± 7.39% and -15.94 ± 3.58%, respectively, all p<0.001; Fig. 4.5A). Within the cortical bone of the diaphysis, p75-FC mildly increased periosteal volume as observed from a statistically significant increase in Saline + p75-FC versus BTxA only groups (1.45 ± 0.34% versus -0.42 ± 0.32%, p<0.005; Fig. 4.5B) and a nearly-significant increase versus the Saline only group (0.14 ± 0.27%, p=0.065; Fig. 4.5B). The endocortical resorption response induced by transient muscle paralysis was also not altered by p75-FC treatment (7.05 ± 1.31% versus 8.61 ± 0.93%, respectively, p=0.705; Fig. 4.5C). Ec.Vol alterations in these groups were significantly greater than in Saline animals with or without p75-FC treatment (-0.31 ± 1.07% and –0.67 ± 0.71%, respectively, all p<0.001; Fig. 4.5C).

4.5 Discussion

By combining flow cytometry, quantitative RT-PCR and primary osteoclast culture with pharmacologic and genetic suppression of inflammatory responses, we were able to explore whether transient calf muscle paralysis creates a permissive osteoclastogenic environment within the tibia bone marrow through an inflammatory mediated process. Though observed inflammatory cell infiltration and pro-osteoclastogenic inflammatory gene expression were temporally consistent with inflammatory mediated bone loss, inhibiting this inflammatory

pathway was not sufficient to mitigate osteoclastic bone resorption induced by paralysis. However, during this process we discovered that enhanced osteoclast fusion might be a potential mechanism for the profound resorptive response observed *in vivo*.

Given that all osteoclastic bone resorption induced by muscle paralysis occurs within the marrow microenvironment, we first assessed whether inflammatory alterations in bone marrow occurred functionally upstream of elevated osteoclast activity (which is evident within 3 days in the metaphysis and around 6 days in the diaphysis, [61]). This was confirmed by CD4+ T cell expansion in the proximal metaphyseal marrow 24 hours following muscle paralysis and by pro-inflammatory gene regulation occurring within the whole marrow 72 hours following paralysis. However, genetic (TCRβδKO) and pharmacologic (TNFα via p75-FC) suppression of inflammatory pathways did not significantly alter bone resorption induced by muscle paralysis in the metaphysis or diaphysis. One potential explanation for these data was our finding that upregulation of osteoclastic fusions genes and marrow permissiveness to form giant osteoclasts occurred concurrent with, not subsequent to, inflammatory gene alterations.

These observations must be considered in the context of the limitations of our approach. In testing the osteoclastogenic potential of marrow following muscle paralysis, we examined the formation of osteoclasts (i.e., cells with 3+ nuclei) and giant osteoclasts (i.e., cells with 20+ nuclei) in culture. Though our initial discretization of osteoclast counts into normal (3+) and giant (20+) osteoclasts was based on previous reports [156-158], the cutoff of giant osteoclast size is somewhat arbitrary and is meant as an efficient way to measure an increase in overall osteoclast size. However, this technique cannot determine if the enhanced giant osteoclast formation observed 3 days after BTxA treatment is caused by a bimodal distribution of osteoclasts sizes (potentially suggesting different mechanisms in forming normal and giant

osteoclasts) or a smooth distribution in osteoclast size throughout the cell culture (suggesting an overall enhancement of cell fusion).

To address this limitation we performed a study in which osteoclast area was used as a surrogate measure for the number of nuclei per cell [159]. In this study we reanalyzed the distribution of osteoclast sizes in a sample of naïve and 3 days post-BTxA cultures (4 samples per group). This was accomplished by automated calculation of osteoclast cell area in a 10 mm^2 subsample of the overall culture area (composite of eighty 20x light microscopy images, Ziess) using custom ImageJ software (FIJI). We found that osteoclast size was smoothly distributed across cell populations in both naïve and Day 3 BTxA marrow (Fig. 4.6). However, Day 3 BTxA marrow skewed toward larger osteoclasts when compared to naïve marrow cultures. The average cell size in cultured Day 3 BTxA marrow was nearly 75% larger than in cultured naïve marrow (Fig. 4.6) and average cells were estimated to contain 6.1 nuclei versus 3.5 nuclei in naïve marrow (based on extrapolating the average size calculated for 3 nuclei osteoclasts). This finding suggests that alterations in giant cell formation observed previously were a result of enhanced cell fusion within the entire marrow culture. This pilot data may also explain an inconsistency between our *in vitro* data suggesting that overall osteoclast number does not increase after BTxA treatment, while a small but significant increase was previously observed *in vivo* [57]. As our *in vivo* osteoclast counts were estimated by stereologic cross-section sampling assuming equivalent cell size between groups, an increase in osteoclast size alone (as observed *in vitro*) would present as an increase in overall osteoclast number.

In two *in vivo* experiments, we implemented genetic or pharmacologic strategies to inhibit the inflammatory response with the expectation of blunting muscle paralysis induced bone loss. While both approaches have been successfully used to allay inflammatory bone loss

in other contexts, neither was effective in our model. Though these experiments provided strong data suggesting that inflammation alone does not mediate acute bone loss following muscle paralysis, the limitation inherent in these models should still be addressed. As with any non-conditional knockout mouse in which the alteration is known to effect bone tissue, phenotypic differences in skeletal morphology may confound potential comparisons with WT mice. This was observed in our TCRβδKO mice, as they had significantly smaller endocortical volumes in the metaphysis than WT counterparts. However, the bone volume fraction (BV/TV) between TCRβδKO and WT mice were nearly identical allowing us to directly compare the induced bone loss response across genotype even in the face of phenotypic bone difference. Though phenotypic bone changes are not observed in pharmacologic interventions, the unintended effect of TNFα inhibition on bone cell function was quantifiable. Observations that Saline + p75-FC treated animals had significant bone formation on the periosteal surface suggests that TNFα inhibition also elevates osteoblast activity, as reported by others [160, 161]. It is possible that transient elevation of osteoblastic function could mask an effect upon osteoclasts in the marrow. Our findings that endocortical and trabecular bone loss were not significantly altered versus untreated controls (even in light of increased osteoblast activity) serves to strengthen our conclusion that TNFα inhibition as accomplished by a maximum dosing regimen of p75-FC was not sufficient to mitigate bone loss following paralysis. However, this does not eliminate TNFα as a potential mediator of bone loss in this model. The possibility remains that the dose and dosing schedule of p75-FC was not sufficient to completely inhibit the profound bolus of TNFα expression observed following paralysis [162]. Further studies are needed, such as altering the dosing schedule of p75-FC, before the true role of TNFα in both giant osteoclast and inflammatory induction is elucidated in our model of transient muscle induced bone loss.

Our findings of acute inflammatory cell infiltration and inflammatory gene regulation in the marrow following muscle paralysis should also be interpreted under consideration of our experimental approaches and their application. Specifically, we chose to investigate the alteration of a small subset of potential inflammatory cells (CD4+ and CD8+ T cells). While our data does not provide an exhaustive description of inflammatory cell alterations in the marrow following muscle paralysis, the result allowed us to assess acute inflammatory cell infiltration of a cell type known to mediate bone cell responses. Similarly, we chose to quantify transcript levels of inflammatory genes, which does not necessarily represent alterations in protein levels of inflammatory cytokines in the marrow. Potential weaknesses in this approach could relate to complex translational regulation of cytokine production or the fact that bone cells known to actively modulate marrow cytokine levels, such as lining cells and osteocytes, are not flushed out with the marrow. This is one potential explanation to the upregulation of OPG transcripts in our study, which has not been observed previously at the protein level [57]. Even with these limitations, this data was temporally consistent with inflammatory pathway alterations mediating bone resorption in this model.

We detected upregulation of both inflammatory cells and inflammatory genes prior to/or coincident with initiation of bone resorption (occurring within 3 days at the earliest). Specifically, CD4+ T cell expansion was detected within the proximal metaphyseal marrow within 24 hours of muscle paralysis. Given that trabecular bone resorption following muscle paralysis first initiates adjacent to the growth plate, the co-localization of inflammatory cells known to mediate bone loss in other models was consistent with our initial hypothesis. The elevated CD4+:CD8+ ratio, which has been associated with osteoporosis, was also consistent with this thesis. As well, altered gene regulation within the marrow environment clearly

reflected an inflammatory response to muscle paralysis. Within 3 days of paralysis, seven genes with functional relevance to inflammation were altered versus naïve controls (TNF, CD44, CD47, IL-4, CD9, IL-1A and IL-1b). Given that bone resorption in the diaphysis occurs almost entirely within 6 to 13 days post-paralysis, the timing of inflammatory gene expression was consistent with inflammatory bone loss in this region as well. However our inability to mitigate bone resorption through pharmacologic and genetic means suggests that inflammatory alterations may be coincident to, and not causal of, bone resorption following muscle paralysis.

One possible explanation for this seemingly contradictory result is that the upstream stimulus that induces the inflammatory response in the marrow may itself be sufficient to drive the osteoclastic response with minimal contribution from the inflammatory cascade. Neuronal signaling represents one such signaling pathway capable of modulating both inflammatory responses and bone cell activity [163]. Given that bone marrow is highly innervated and that BTxA induces muscle paralysis through altered nerve signaling in the muscle, we have begun to explore if communication between these adjacent nerve fibers might control bone resorption. Two preliminary studies suggest this is a distinct possibility. We have shown that a peripheral nerve injury model induces a similar, but somewhat muted, pattern of bone loss to that observed following muscle paralysis [164]. Unlike our model of transient muscle paralysis, PNI induced bone resorption occurs without accompanied muscle loss or gait defects. Even more intriguing was our finding that mice with peripheral sensory defects have a dramatically muted bone loss response following muscle paralysis [58]. Taken together, these data suggest that neuronal control might modulate temporally coincident inflammatory and bone cell alterations, giving reason to our finding that blocking inflammation alone is not sufficient to block bone loss induced by paralysis.

Our data demonstrated that transient calf muscle paralysis rapidly altered the osteoclastogenic potential of bone marrow in the adjacent tibia. This observation was congruous with our previous studies and those of others [57, 165]. The timing in which marrow became permissive to osteoclastogenesis (day 3 after paralysis), coupled with the time needed to form functioning osteoclasts from precursor populations (around 5 days) is completely consistent with the onset of diaphyseal endocortical resorption following paralysis (which occurs in a window between days 6 and 13 post-paralysis), but occurs after the trabecular resorption is over 65% complete [49]. Surprisingly, however, our primary cell culture experiment indicated that the marrow was not predisposed to generate greater numbers of osteoclasts following muscle paralysis, but rather to generate many more giant osteoclasts. Giant osteoclasts are primarily associated with inflammatory pathologies and are capable of resorbing large volumes of bone mineral [143, 166-168]. Interestingly, a recent pilot study suggests one potential reason that p75-FC treatment was unsuccessful at minimizing bone loss *in vivo* may be its observed inability to significantly decrease giant cell formation in marrow harvest from p75-FC treated mice 3 days following paralysis (Fig. 4.7).

Several genes implicated in osteoclast fusion and giant osteoclast formation were upregulated concomitant with marrow permissiveness to giant osteoclast formation. Most notable was the gene expression of the essential protein for osteoclast fusion, DC-STAMP [20, 21, 169], as well as another common osteoclast fusion protein, OC-STAMP [170]. IL-4 has been shown to promote the formation of multinucleated giant cells from macrophage precursors through the overexpression of E-cadherin [171]. Other recent reports identified that upregulation of TNF in the absence of CD44 results in generation of highly resorbing giant osteoclast [168]. As TNF expression was profoundly elevated in our intact model, the downregulation of CD44 on

day 3 may also assist in enabling the observed generation of giant osteoclasts. If true, this mechanism would further suggest that p75-FC dosing or timing was not sufficient to completely block TNF expression in the marrow following paralysis.

Inflammatory mediation of giant osteoclast formation has been observed in other models of profound osteoclastic resorption, such as Paget's Disease of Bone (PDB) [172]. Specifically, PDB is a chronic disorder in which giant highly-resorbing osteoclasts cause abnormal breakdown of skeletal tissue. PDB has been linked to mutations in the p62 gene, an important intracellular modulator of RANKL induced osteoclastogenesis [173]. This mutation has been shown to cause an overexpression of p62 [174] and results in a hyper responsiveness of osteoclast precursors to both inflammatory cytokines and RANKL [175, 176]. Given that p62 expression is upregulated during neuronal degeneration and has been shown to have a protective effect against cell death [177-180], upregulation or dysregulation of p62 in an inflammatory marrow environment caused by neuronal mediated transient muscle paralysis represents a potential pathway of hyperosteoclastogenesis in our model. This is further supported by a reanalysis of our marrow samples identifying a nearly 147% increase in p62 levels in marrow harvested 3 days post BTxA versus naïve controls (3.9 ± 1.2 vs. 1.6 ± 0.1 fold expression relative to HPRT housekeeping gene).

Taken together, our data suggests that transient calf muscle paralysis induces acute inflammation within the marrow of the adjacent tibia that is temporally consistent with inflammatory mediated bone loss (Fig. 4.8). However, given our inability to alter bone resorption through the suppression of the immune pathway, this inflammatory response is potentially coincident to, and not causal of, the rapid bone resorption observed in this model. Most importantly, our data suggest that transient muscle paralysis predisposes bone marrow to

formation of giant osteoclasts within 3 days following muscle paralysis. The identification of this narrow temporal window of pro-osteoclast fusion provides a novel opportunity for optimal intervention in this bone loss pathology.

4.6 Conclusions of Dissertation Research

In Chapter 4, we have identified an inflammatory cascade in the medullary cavity of the tibia capable of mediating bone loss in our model. Specifically, inflammatory cell infiltration, enhanced osteoinflammatory and osteoclastic gene expression and altered permissiveness to osteoclastogenesis were sequentially identified with the marrow of the experimental tibia following muscle paralysis. However, attempts to pharmacologically and genetically intervene in the inflammatory process were not sufficient to mute the profound bone loss induced by transient muscle paralysis, potentially due to their inability to block giant osteoclast formation. As such, Chapter 5 sums up the findings and contributions of this dissertation and describes proposed and ongoing studies building off these findings to further elucidate the biological mechanisms of the profound bone loss following transient muscle paralysis.

4.7 Acknowledgements

We would like to thank Amgen Inc. for their donation of the p75-FC fusion protein and their guidance in the design of the corresponding experiment. Also, we would like to thank Kate Smigiel of the Campbell Laboratory at the Benaroya Research Institute for her assistance throughout the flow cytometry experiment.

Table 4.1: Primer sequences for RT-PCR analysis

Target	Forward (5'→3')	Reverse (5'→3')
HPRT	AGTGTTGGATACAGGCCAGAC	CGTGATTCAAATCCCTGAAGT
TNF	AGCCCCCAGTCTGTATCCTT	CTCCCTTTGCAGAACTCAGG
DC-STAMP	GCCGTTCTGTCGTGTGGCCT	GCGGAGTGGCAAGGCCGTAAA
OC-STAMP	ACCTCCGGTGGAGAGCGTGT	ACAGTCGTGGGGCGTGAAGC
CD9	GCCGCCGTCTGGGGCTATAC	TGCCACAGCAGTCCAACGCC
CD44	TCCAGGGGGAGTTCCCGCAC	CCGCGATGCAGACGGCAAGA
CD47	AAGCGCGATGCCATGGTGGG	AGTGTTGAAGGCCGTGCGGTT
CD81	TGGGGACGTTCTTCACCTGCCTT	GGGGGTGAGTATGTTGCCGCC
IL1a	GCAACGGGAAGATTCTGAAG	TGACAAACTTCTGCCTGACG
IL1b	GCCCATCCTCTGTGACTCAT	AGGCCACAGGTATTTTGTCG
IL4	GGTCTCAACCCCCAGCTAGT	GCCGATGATCTCTCTCAAGTGAT
IL11	CTGTGGGGACATGAACTGTG	CGTCAGCTGGGAATTTGTCT
RANKL	CCAAGATCTCTAACATGACG	CACCATCAGCTGAAGATAGT
OPG	CTGCCTGGGAAGAAGATCAG	TTGTGAAGCTGTGCAGGAAC

Table 4.2: Baseline trabecular morphology [mean ± s.e.]

	WT	TCRβδKO
Endocortical Volume,TV or Ec.Vol (mm^3)	1.59 ± 0.05	1.26± 0.02 *
Trabecular Bone Volume, BV (mm^3)	0.046 ± 0.002	0.037 ± 0.003
Bone Volume Fraction, BV/TV	0.029 ± 0.001	0.029 ± 0.002
Trabecular Number, Tb.N (#/mm)	2.78 ± 0.16	2.91 ± 0.14
Trabecular Thickness, Tb.Th (mm)	0.045 ± 0.001	0.041 ± 0.001 *
Trabecular Spacing, Tb.Sp (mm)	0.37 ± 0.02	0.35 ± 0.02

* Significantly different from WT ($p<0.05$)

Table 4.3: TCRβδKO diaphyseal morphology 22 days post paralysis [mean ± s.e.]

	Contralateral	Experimental
Periosteal Volume, Ps.Vol (mm^3)	0.96 ± 0.02	0.94 ± 0.01
Cortical Volume, Ct.Vol (mm^3)	0.53 ± 0.01	0.47 ± 0.01 *
Endocortical Volume, Ec.Vol (mm^3)	0.44 ± 0.01	0.47 ± 0.01 *

* Significantly different from contralateral ($p<0.03$)

Table 4.4: Relative mRNA expression in tibia following calf paralysis [mean ± s.e]

		Days after Botox injection		
	Untreated	Day 1	Day 3	Day 7
TNF	1.15 ± 0.30	1.87 ± 0.80	4.59 ± 0.80 ↑	2.81 ± 0.79
DC-STAMP	0.39 ± 0.11	0.66 ± 0.24	1.73 ± 0.41 ↑	1.10 ± 0.32
OC-STAMP	0.22 ± 0.06	0.32 ± 0.13	0.92 ± 0.24 ↑	0.47 ± 0.11
CD9	1.47 ± 0.48	1.23 ± 0.45	Undetectable	Undetectable
CD44	1.41 ± 0.43	1.04 ± 0.38	0.19 ± 0.11 ↓	0.95 ± 0.57
CD47	0.99 ± 0.23	0.91 ± 0.28	0.12 ± 0.06 ↓	0.48 ± 0.25
CD81	1.44 ± 0.54	0.98 ± 0.25	0.98 ± 0.15	1.10 ± 0.31
IL1a	0.05 ± 0.01	0.05 ± 0.02	Undetectable	Undetectable
IL1b	0.12 ± 0.04	0.13 ± 0.04	Undetectable	Undetectable
IL4	0.60 ± 0.13	0.72 ± 0.16	2.06 ± 0.38 ↑	2.10 ± 0.50 ↑
IL11	0.17 ± 0.04	0.16 ± 0.05	0.26 ± 0.07	0.21 ± 0.08
RANKL	0.80 ± 0.16	1.08 ± 0.29	2.18 ± 0.47 ↑	1.86 ± 0.57
OPG	0.38 ± 0.10	1.08 ± 0.60	1.60 ± 0.36 ↑	1.13 ± 0.39

Significant increase (↑) or decrease (↓) vs Untreated (all $p < 0.05$)
Undetectable = Unquantifiable expression in at least half the samples

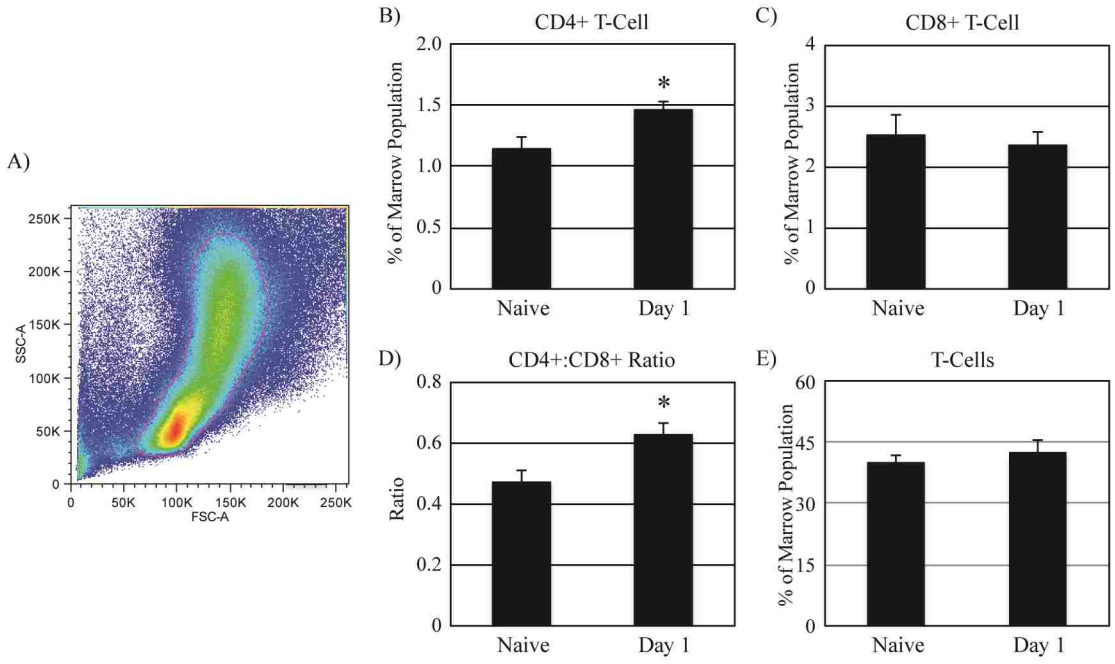

Figure 4.1: CD4+ T cell Expansion in the Marrow of the Proximal Metaphysis
Prior to assessing the frequencies of T cell populations within the bone marrow, cellular debris was removed from individual marrow sample analysis using traditional forward- (FSC) and side-scatter (SSC) gating (A). Within these gated samples, the percentage of CD4+ T cells in the bone marrow was significantly expanded 1 day following transient muscle paralysis (B, mean ± s.e., $p<0.04$), while the CD8+ populations remained unchanged (C, $p=0.71$). This resulted in a significant difference in the marrow CD4+:CD8+ ratio (D, $p<0.03$) even though the overall T cell population was not changed (E, $p=0.54$).

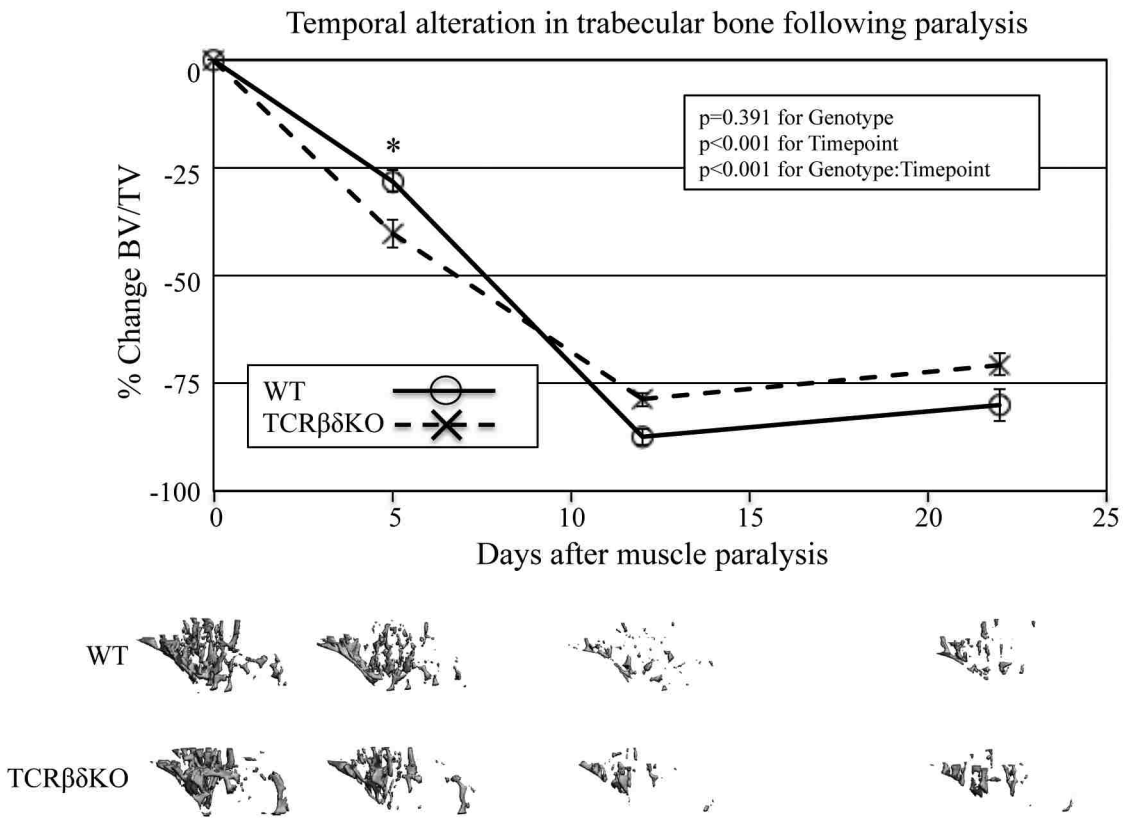

Figure 4.2: Bone Loss in TCRβδKO Mice
Trabecular bone resorption in the proximal metaphysis following muscle paralysis was not muted in TCRβδKO mice. Temporal BV/TV alterations in WT mice were consistent with previous studies in that bone loss initiated by day 5, reached its peak around day 12 and mildly recovered by day 22 (mean ± s.e.). When compared to WT controls, BV/TV alterations were enhanced in TCRβδKO mice on day 5 ($p<0.04$) but not significantly different on days 12 or 22 (all $p>0.16$).

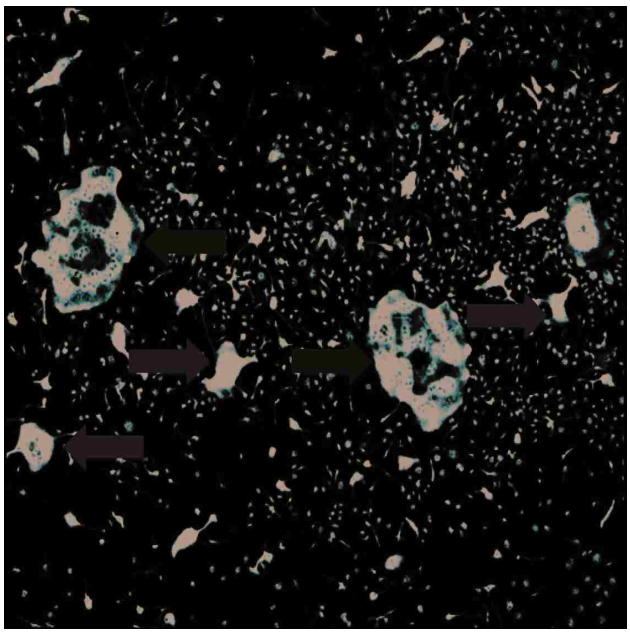

Figure 4.3: TRAP Stained Osteoclasts and Giant Osteoclasts
Sample cell culture image from bone marrow harvested 3 days after transient muscle paralysis and cultured for 8 additional days. Two giant osteoclasts can seen in this image (red arrows) with multiple smaller osteoclasts surrounding them (three are highlighted with green arrows).

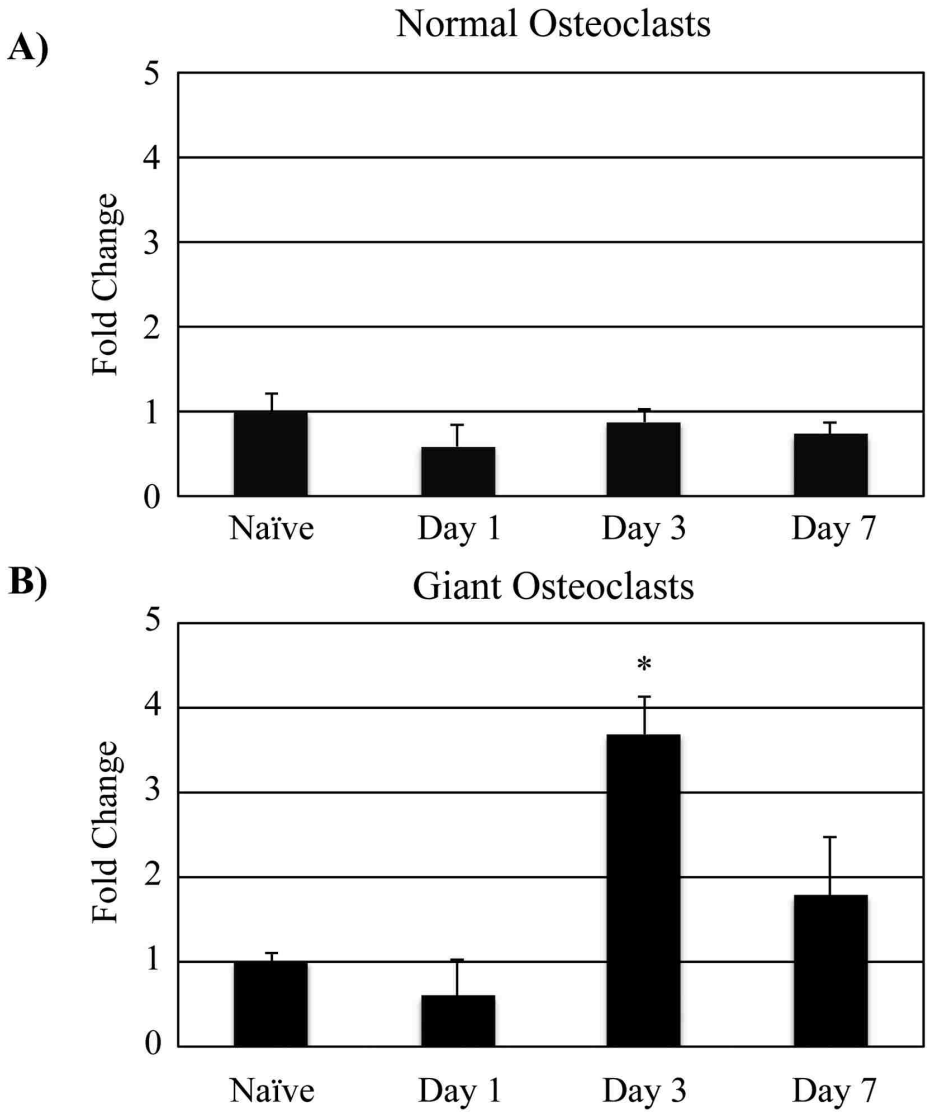

Figure 4.4: Osteoclastogenic Potential of Marrow
Transient muscle paralysis augmented the osteoclastic potential of tibial marrow through enhanced osteoclast fusion, but not increased osteoclast number. In whole tibia marrow cultured from Naïve mice and from mice at various time points following muscle paralysis, no significant differences were observed in the total number of osteoclasts (A, mean ± s.e., $p=0.52$). However, giant osteoclast formation was enhanced in marrow harvested 3 days following paralysis (B, * significantly greater than Naïve and Day 1 groups, all $p<0.01$)

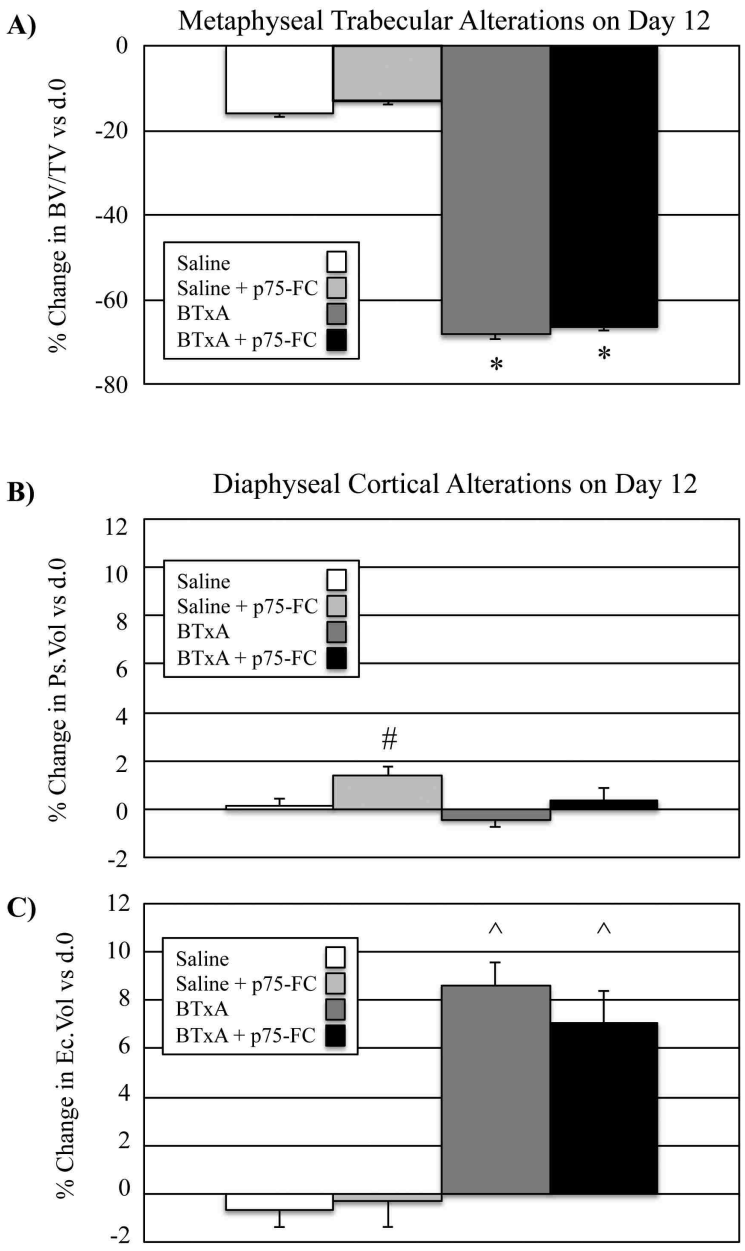

Figure 4.5: Bone Loss in p75-FC Treated Mice
Pharmacologic TNFα inhibition did not block metaphyseal trabecular bone or diaphyseal cortical bone resorption induced within twelve days of muscle paralysis. Animals having undergone prophylactic dosing with p75-FC protein had significantly elevated changes in proximal metaphyseal BV/TV following muscle paralysis compared to Saline and Saline + p75-FC groups (A, * $p<0.001$), but were statistically similar to BTxA only treated animals. In the tibia mid-diaphysis, p75-FC had a mild effect on osteoblast activity on the periosteal surface as seen by elevated Ps.Vol in Saline + p75-FC mice (B, # significant difference from BTxA only group, $p<0.004$). However, the endocortical expansion commonly associated with diaphyseal bone loss induced by muscle paralysis was not blunted by p75-FC dosing (C, ^ BTxA and BTxA + p75-FC were significantly different from Saline and Saline + p75-FC, $p<0.001$).

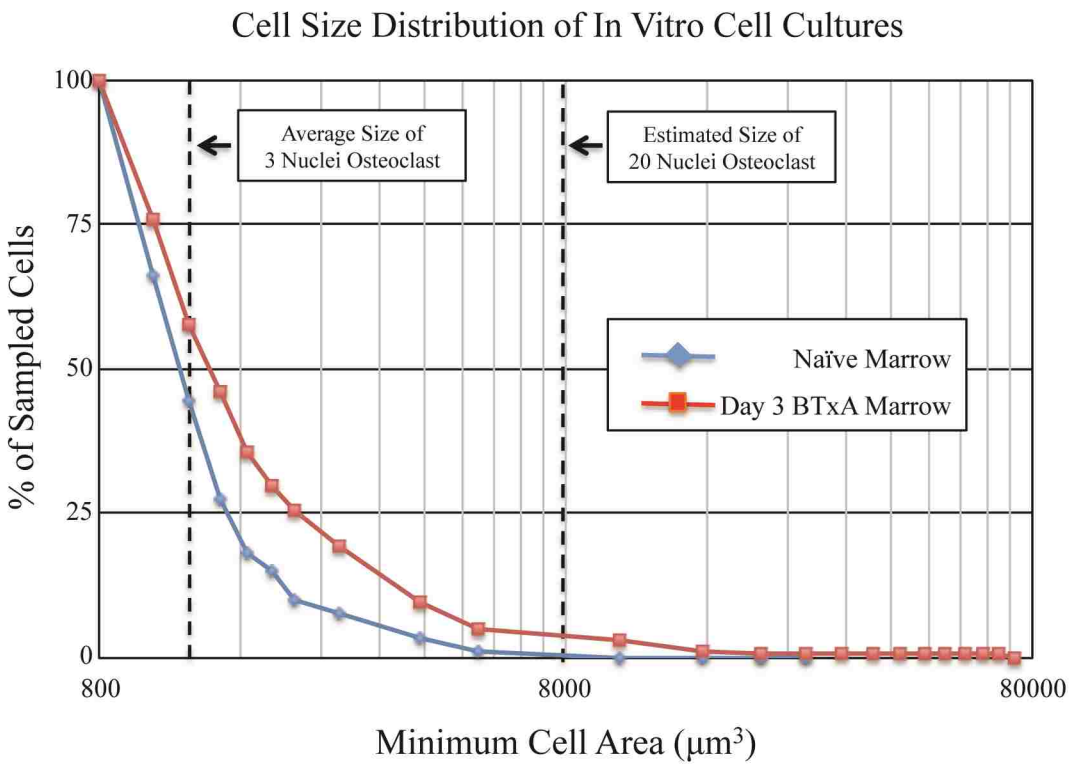

Figure 4.6: Distribution of Osteoclasts Size in Culture
For the purposes of this analysis, osteoclastic cells were identified as cell greater in size than the mean – s.d. of the average sized 3-nuclei osteoclast (1242 ± 452 μm^2). Osteoclast size in marrow harvested 3 days after BTxA injection was consistently larger in comparison to naïve marrow cultures.

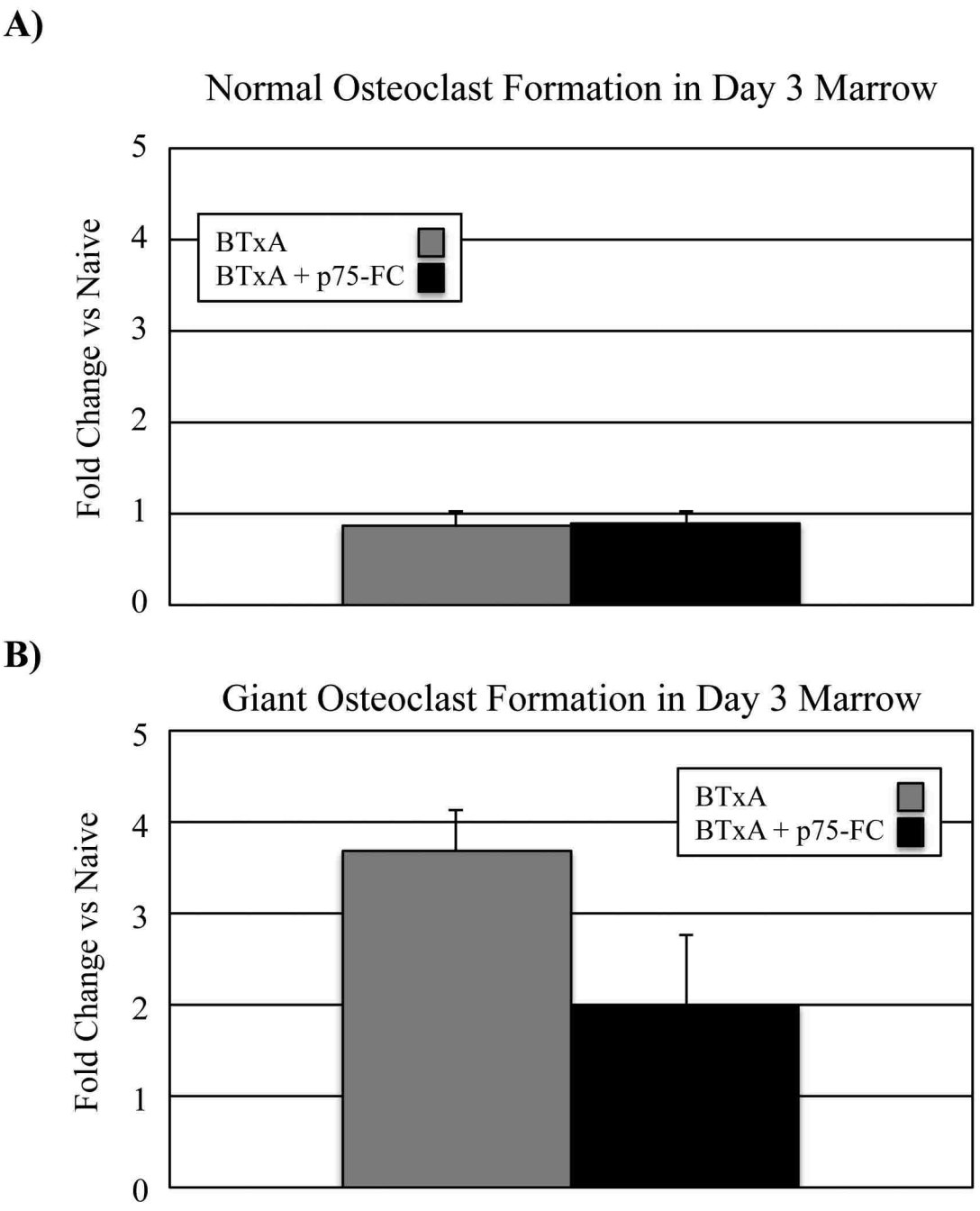

Figure 4.7: p75-FC Treatment and Giant Osteoclast Formation
When harvested 3 days after BTxA injection, marrow from p75-FC treated mice (n=6) showed no significant difference from untreated mice (n=4) in their ability to form normal osteoclast in bone marrow cultures (A, p=0.95). Similarly, p75-FC did not significantly decrease the marrow's potential to form giant osteoclasts on day 3 (B, p=0.14).

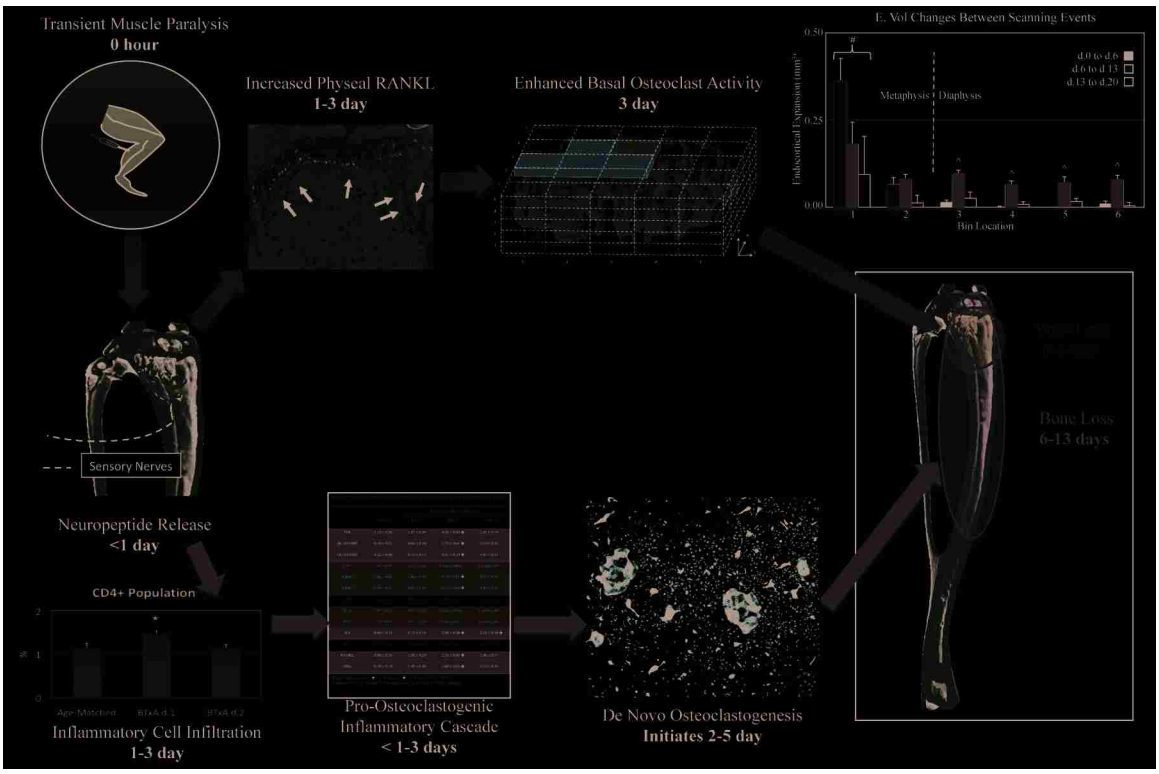

Figure 4.8: Inflammatory Mediated Bone Loss Cascade Temporally Consistent With Secondary Resorptive Event
The inflammatory cascade and altered osteoclastogenesis within tibia bone marrow was consistent with our hypothesis of inflammatory bone loss mediating the secondary osteoclastogenic event following muscle paralysis (green arrows). Specifically, inflammatory cell infiltration occurred upstream of both osteoinflammatory gene expression and altered marrow permissiveness to osteoclastogenesis. However, future experiments are still needed to clarify the importance of this pathway in mediating bone loss observed within 6-13 days post-paralysis.

Chapter 5: Conclusions

In this final chapter, the specific contributions of this research to broadening the understanding of bone physiology and bone metabolism are discussed, along with the impact of the developed μCT image registration techniques on the field of bone imaging. This chapter closes with future avenues of investigation made possible by leveraging the insights and techniques highlighted in the dissertation (Fig. 5.1).

5.1 Specific Contributions

As was discussed in Chapter 1, our model of transient muscle paralysis was initially designed to induce bone loss through mechanical disuse. Our findings of dramatically disproportional bone resorption in comparison to the mild gait defect in this model began a reshaping of how our field views muscle and bone interaction. It was traditionally believed that ground reaction forces during gait and bone forces engendered by muscle contraction were the primary determinants of muscle induced bone homeostasis [181, 182]. However, the work contained within this dissertation has added to a growing body of literature from our group and others suggesting that bone homeostasis is controlled in part through direct signaling between muscle, nerves and bone [183-185]. Beyond helping to clarify the role of muscle function on bone homeostasis, the imaging techniques developed throughout this dissertation hold potential to broadly contribute to non-invasively accessing bone adaptation (both catabolic bone loss and anabolic bone formation as discussed in Section 5.2.4). Specifically, we were able to show for the first time that μCT imaging registration could be used to quantify the three-dimensional nature of osteoclast activity in a model of profound bone resorption. We believe that similar techniques could be used throughout the bone-imaging field to enhance the utility of commonly

obtained μCT images. In fact, we have ourselves already expanded this technique to explore bone anabolism in a model of mechanical loading induced bone formation (Section 5.2.4).

Chapter 2 was focused upon the creation of a novel μCT image registration approach capable, for the first time to our knowledge, of quantifying significant three-dimensional bone resorption. Bone loss induced by transient muscle paralysis phenotypically occurs only on the endocortical bone surface (i.e., periosteal surface remains unchanged). The periosteal volume was not only used as a consistent image registration volume, but also allowed for quantification of image registration accuracy in tibia bone volumes that otherwise changed dramatically across the 21 day experiments. This differentiation from previous attempts to register serial μCT images through best-fit algorithms allowed us to move beyond qualitative assessment of bone resorption, and permitted quantitative determination of the locations of high osteoclast activity. This technique identified a complex, yet highly repeatable, pattern of endocortical bone resorption in the diaphysis following muscle paralysis. The location of bone resorption was not consistent with areas of greatest strain reduction secondary to transient muscle paralysis, further suggesting that mechanical disuse is not the primary driver of bone resorption in this model. However, we quantitatively determined that focal activation of osteoclastic resorption did not occur on bone surface with high basal osteoblast activity. These data suggests that the spatial pattern of bone loss observed in this experiment may be an accentuation of the resorptive aspect of normal cortical bone modeling drifts.

In Chapter 3, we determined the spatiotemporal dynamics of distinct osteoclastic resorption in the metaphyseal and diaphyseal compartments following muscle paralysis. This was accomplished by utilizing novel μCT imaging techniques including expanding our image registration approach to track alterations in the highly metabolically active trabecular bone

compartment. Though compartmental variations (e.g., metaphyseal versus diaphyseal compartments) in bone resorption are often identified in models of bone loss, the causal factors for these differences are rarely identified. This is in part due to a lack of experimental models and techniques that allow for a direct comparison of these spatially disparate responses. We were able to not only track osteoclastic activity throughout the metaphysis and the diaphysis in a single long bone, but also identify potential mechanisms governing these responses. Through the use of trabecular image registration, we determined that metaphyseal bone resorption following muscle paralysis initiates within 3 days of paralysis through enhancement of basal osteoclast function at the growth plate. Conversely, diaphyseal bone resorption occurs almost exclusively within 6 to 13 days post-paralysis. The timing coupled with the homogenous nature of bone resorption along the diaphyseal bone suggested *de novo* osteoclastogenesis was mediating the response in this compartment. The findings of this study provided a small temporal window in which bone loss is initiated and executed following paralysis. As well, the spatiotemporal bone loss patterns suggested specific mechanisms (i.e., enhanced osteoclastic activity and *de novo* osteoclastogenesis) by which they occurred. As such, this data leads directly to the hypothesis tested in Chapter 4.

In Chapter 4, we investigated whether transient muscle paralysis enhances bone marrow osteoclastogenesis through induction of inflammation in tibia bone marrow. This hypothesis originated not only from the timing and nature of bone loss identified in Chapter 3, but also the growing amount of literature suggesting inflammatory control of bone cell activity. Our studies identified an inflammatory cascade within the bone marrow following muscle paralysis that was temporally consistent with our hypothesis (especially *de novo* osteoclastogenesis in the diaphysis). Specifically, following paralysis we identified inflammatory cell infiltration within

24 hours, and an increase in osteoinflammatory gene expression and the osteoclastic potential of bone marrow within 72 hours. Given the time needed to form functioning osteoclasts *in vivo,* the observed alterations in bone marrow were completely consistent with the diaphyseal bone loss detected almost exclusively between days 6 and 13. However, we were unable to blunt bone resorption through genetic (T cell deficiency) or pharmacologic (anti-TNF) inhibition of the inflammatory pathway. Though the genetic inhibition study clearly eliminated T cells as the primary mediator of bone loss in this model, the pharmacologic TNF inhibition study was less definitive in ruling out a TNF mediated osteoclastogenic pathway in this model. For that reason future studies are planned to elucidate the role of the profound upregulation of marrow TNF expression in mediating transient muscle paralysis (Section 5.2.1).

The most intriguing contribution of the research contained within Chapter 4 was the identification of giant osteoclast formation as a potential mechanism of bone resorption following muscle paralysis. These findings were supported by a concurrent upregulation of fusion genes and genes with synergistic potential to enhance osteoclast fusion. These pagetic-like osteoclasts have not been previously identified in our model. This discovery has now opened a new avenue of research to determine the resorption potential of these giant osteoclasts (Section 5.2.2), as well as determining if monocyte fusion is a potential therapeutic target for blocking bone loss following muscle paralysis (Section 5.2.3). Most importantly, this finding has now led to a revision of our hypothesis of how bone resorption is achieved following muscle paralysis. We now believe that diaphyseal bone loss following transient muscle paralysis occurs through RANKL mediated formation of giant osteoclasts. Identifying if marrow inflammation is causal of, or coincident to, this process still needs to be determined (Fig. 5.1).

5.2 Future Research

Though the research described in the previous three chapters has given clarity to many aspects of bone loss induced by transient muscle paralysis, it has also provided provocative insights into new avenues of research. Described below are some of the questions that represent a logical progression of exploration into our model of transient muscle paralysis, as well as how these questions might be addressed experimentally. This section closes with a pilot project that applies our image registration approach to a model of bone anabolism.

5.2.1 Does TNFα Mediate Bone Loss Following Muscle Paralysis?

Throughout Chapter 4 we investigated if bone loss following muscle paralysis was mediated by inflammation. One focus of this research was determining if TNFα signaling was a critical mediator of this process, as it has been identified in other inflammatory bone loss models. We found that the timing of the profound upregulation of TNFα gene expression was consistent with a role in mediating bone loss following transient muscle paralysis. However, our attempt to pharmacologically block TNFα signaling was not sufficient to blunt bone loss in our model. Even though we used the maximum allowable dosing schedule of a powerful TNFα inhibitor, we lacked data that showed TNFα expression was completely blocked in the marrow. As such, we have planned a more definitive experiment as to the role of TNFα mediation of bone loss following paralysis.

We are now in the process of acquiring approval to transiently paralyze the calf muscle of TNF deficient mice (B6;129S6-*Tnf*^{tm1Gkl}/J from Jackson Laboratory). In this planned experiment, we will compare metaphyseal and diaphyseal bone morphology alterations following muscle paralysis in TNF deficient and wild type mice across our common observation

time points (i.e., days 5, 12, and 21). If the bone loss pattern observed is similar in these groups of mice, this will provide more definitive proof that TNFα is not mediating bone loss in our model. However, a finding of blunted bone loss in TNFα deficient mice will require further follow-up experiments. These experiments include determining how TNF deficiency alters both the gene expression patterns and giant osteoclast potential of the marrow following muscle paralysis. As well, we would also determine if altering the dosing schedule of p75-FC would be sufficient to reproduce the findings of blunted bone loss in TNF deficient mouse strains.

If TNFα signaling is not sufficient to mediate bone loss in our model, future experiments will focus on RANKL expressing cell type(s) as modulators of bone resorption. As we know that osteoclastic resorption following muscle paralysis is RANKL mediated, the temporal signature of RANKL signaling throughout the experimental tibia may provide clues into how our observed spatiotemporal pattern of bone loss is achieved (e.g., timing and cell types responsible for RANKL expression). Following muscle paralysis, we will harvest tibiae on days 1, 3 and 7 and quantify RANKL levels separately in the tibia marrow, the proximal tibia metaphyseal bone (including growth plate) and the diaphyseal cortical bone. Unlike our previous experiments in which we observed RANKL gene expression in the marrow only, this experimental will allow us to determine the potential role of matrix embedded (e.g., osteocytes and chondrocytes) and matrix adhered (e.g., osteoblasts and lining cells) cell types in controlling the RANKL mediated bone loss. This differentiation from previous experiments is necessary given the recent evidence that osteocytes and chondrocytes not only suppress osteoblast activity in other bone loss models through sclerostin signaling [186, 187], but also are highly efficient RANKL expressing cell types capable of inducing osteoclastic resorption [188, 189]. Further, osteocytes have been shown capable of actively recruiting osteoclasts to specific bone surfaces through apoptotic

mechanisms [190-192], suggesting that the osteocytic network itself holds potential to produce the spatially complex, yet repeatable, endocortical resorption pattern quantified in Chapter 2.

5.2.2 What Is the Resorptive Capacity of the Giant Osteoclasts?

Our findings of enhanced fusion gene expression and permissiveness of marrow to form giant osteoclasts represents an exciting potential mechanism responsible for the profound bone loss in our model. However, we have not yet determined the resorption potential of the giant osteoclasts observed in cell culture. This is an important next step because while the giant osteoclasts observed in Paget's disease are highly resorbing, others observed following long term bisphosphonate therapy have limited resorption potential [156].

To test the resorptive capacity of giant osteoclasts, we plan to utilize an *in vitro* model of quantifiable bone resorption designed by Cameron Rementer of the Giachelli Lab at the University of Washington [193]. Bone marrow will be harvested from mice 3 days following muscle paralysis (timepoint at which the permissiveness of giant osteoclast formation is significantly upregulated) as described previously (Section 4.4.4). This marrow will be seeded onto 5 mm murine calvarial disc biopsies and cultured as previously described (Section 4.3.4). *In vitro* bone resorption will be determined by comparing pre- and post- μCT of the calvarial volumes. An increase in bone resorption will be determined by comparing volume alterations to naïve mouse cultures. We expect that the resorptive potential of marrow harvested 3 days following muscle paralysis will be significantly greater than in naïve marrow cultures, suggesting that enhanced cell fusion following muscle paralysis is an important pathway in our model.

5.2.3 Is Cell Fusion a Therapeutic Target For Blocking Bone Loss Following Paralysis?

If giant osteoclasts are determined to be highly destructive to bone tissue in the above experiment, we will target cell fusion pathways as a prophylactic therapy for mitigating bone loss following muscle paralysis. Specifically, mice receiving BTxA induced paralysis will be treated with a cell fusion inhibitor, ketoconazole, prior to cell fusion gene upregulation identified previously [194, 195]. The effect of ketoconazole treatment will be identified through μCT imaging of the right tibia metaphysis and diaphysis on days 5,12 and 21 post-paralysis. If ketoconazole was effective at blocking bone loss in our model, this would be strong confirmation of the role of enhanced cell fusion as a necessary mechanism for paralysis induced bone loss. This finding would also lead to experiments determining specific signaling cascades responsible for this process, including investigations into DC-STAMP, OC-STAMP and p62.

5.2.4 Quantification of Site-Specific Bone Alterations in a Model of Bone Anabolism Using μCT Image Registration

The μCT image registration techniques developed in the previous chapters hold broad potential to enhance the utility of serial μCT imaging studies throughout the bone biology field. For example, in anabolic models such as mechanically induced bone formation, serial μCT images are generally used to describe gross alteration in bone tissue across time. However, defining how these gross alterations affect structural integrity of bone tissue is difficult as bone cell kinetics (both osteoblastic and osteoclastic) responsible for these changes are rarely homogenous [196-198]. For this reason, μCT imaging in these models must be coupled with resource intensive dynamic histomorphometric analysis of focal osteoblast activity (while ignoring osteoclast activity). If a serial μCT image registration approach could be applied in

these models, it could eliminate the need for histomorphometric analysis by providing a complete three-dimensional map of bone cell activity (both osteoblastic and osteoclastic).

Using our model of mechanical loading induced bone formation in the murine tibia [199], we have begun to investigate the temporal and spatial dynamics of bone alterations in aged mice (22 month) treated with and without cyclosporine. Cyclosporine is an immunosuppressant drug previously shown to recover bone mechanoresponsiveness at senescence when dosed appropriately [196]. In this study, aged animals were mechanically loaded on Monday, Wednesday, and Friday for 9 weeks. A 4.45 mm μCT scan of the tibia beginning 2.00 mm distal to the tibia-fibula junction and progressing proximally was obtained immediately prior to the initiation of loading (Week 0). Identical scans were obtained on Weeks 3, 6 and 9. In order to provide a standard comparison for bone alterations determined through image registration, mice received calcein labels on days 10 and 19 and alizarin on days 52 and 61 and were processed for dynamic histomorphometry analysis at the study termination date (Week 9).

Image registration of the serial scans was achieved using the periosteal volume of the distal 2.20 mm of the scan volume as the Image Registration Volume (IRV). This IRV was chosen for two reasons. Loading induced mechanical strains are minimal in this area, and thus are less likely to induce periosteal bone formation that would confound image registration accuracy [199]. As well, this volume encompasses the tibia-fibula junction, which provides a dramatic landmark for image registration alignment and comparisons. Quantitative analysis of the registered samples is still currently underway, but preliminary visual inspection of the registered bones is highly encouraging. Analysis of the IRV showed both a precise alignment of the periosteal volumes and the longitudinal location of the tibia-fibula junction across scans. We believe this allowed us to spatially track both bone formation and bone resorption across 9 weeks

in an area with high bone cell activity (Fig. 5.2). The most compelling evidence of the utility of this technique was the fact that bone formation/resorption after 9 weeks of loading was spatially consistent with the histomorphometric image at the same location within the same bone (Fig. 5.3). As dynamic histomorphometry is not a direct measurement of entire tissue level alterations and cannot detect bone resorption, this finding suggests image registration techniques could one day supplant dynamic histomorphometry as a measure of bone adaptation to anabolic stimuli. As this technique provides a digital representation of bone alterations, analysis of bone sections could be automated and determined across entire bone volumes greatly increasing the throughput and data collection in these studies.

5.3 Concluding Remarks

The goal of this dissertation was to identify origins of transient muscle paralysis-induced bone loss. Through novel μCT image registration techniques, we were able to enhance the spatiotemporal resolution at which bone alterations could be quantified. This technique can be expanded to explore focal bone alterations throughout the bone imaging field. Beyond this technical advancement, this dissertation provided biologic findings of the initiation and propagation of bone loss following muscle paralysis, which we believe helps clarify the effect of muscle function on bone homeostasis. Most importantly, this data identifies potential therapeutic targets to mitigate bone loss induced by a variety of neuromuscular pathologies.

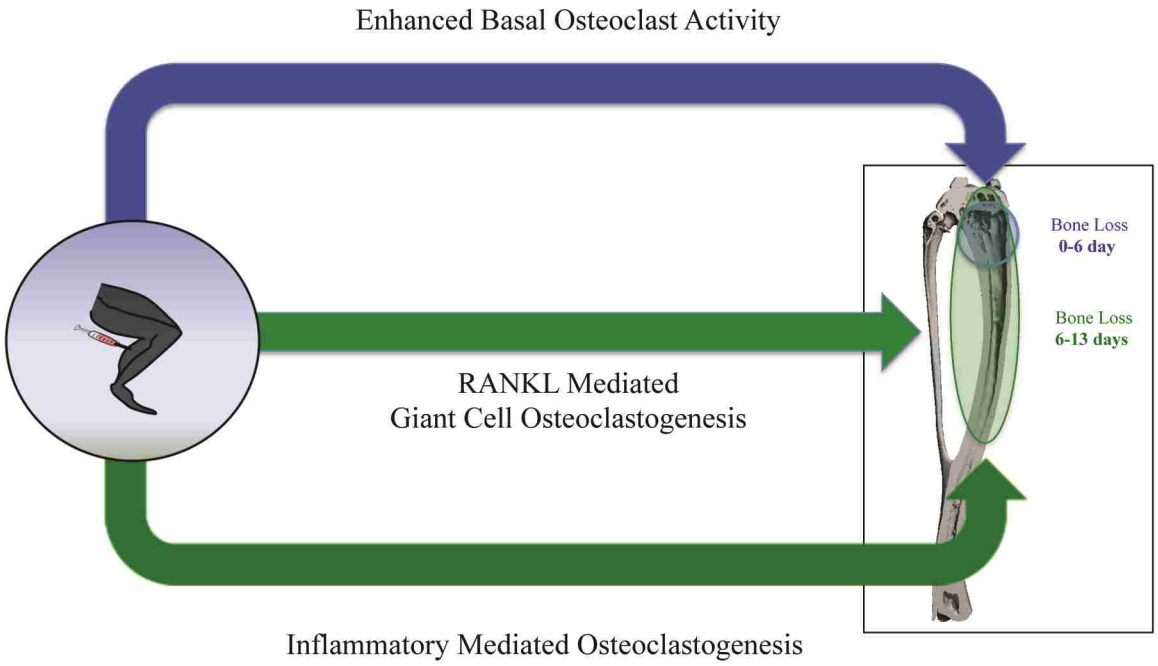

Figure 5.1: Current Understanding and Future Research
This dissertation helped define separate osteoclastic events induced by transient muscle paralysis, as well as provide potential mechanisms controlling these events. Enhanced activation of basal osteoclast function near the growth plate is likely the cause of trabecular bone loss observed within the first week of paralysis (Chapter 3, blue arrow). Though bone loss induced within the second week is temporally consistent with inflammatory mediated osteoclastogenesis (Chapter 4, bottom green arrow) further studies are needed to clarify a causal or coincident role of inflammation in this model (Section 5.2.2). Regardless of inflammatory mediation, the role of RANKL mediated giant osteoclast formation (Chapter 4, middle green line) represents an exciting new avenue of exploration into the potent resorptive response following paralysis (Section 5.2.3 and 5.2.4).

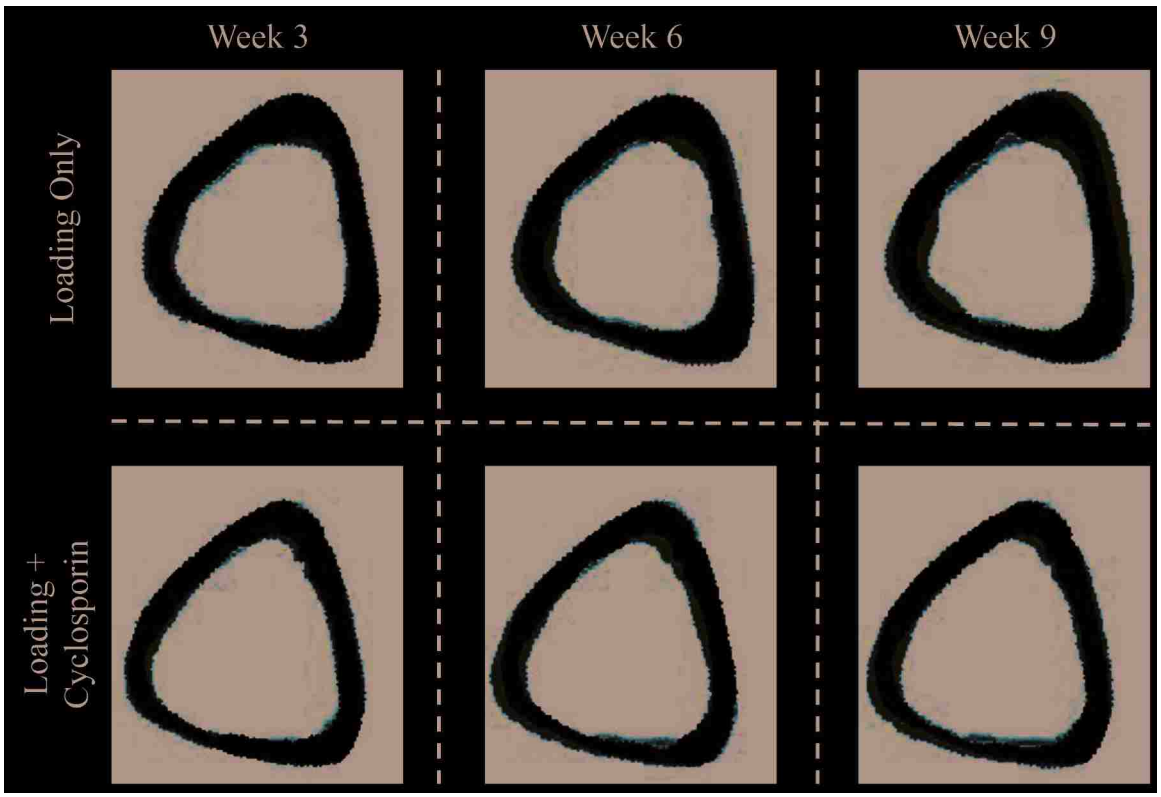

Figure 5.2: Spatiotemporal Alterations in Bone Morphology Following Mechanical Loading
Our image registration approach enabled detection of spatial and temporal alterations in bone formation (orange) and bone resorption (red). Above are examples of how these alterations progressed across 9 weeks in two groups of experimental animals at a 2-D location in the diaphysis generally used for dynamic histomorphometry.

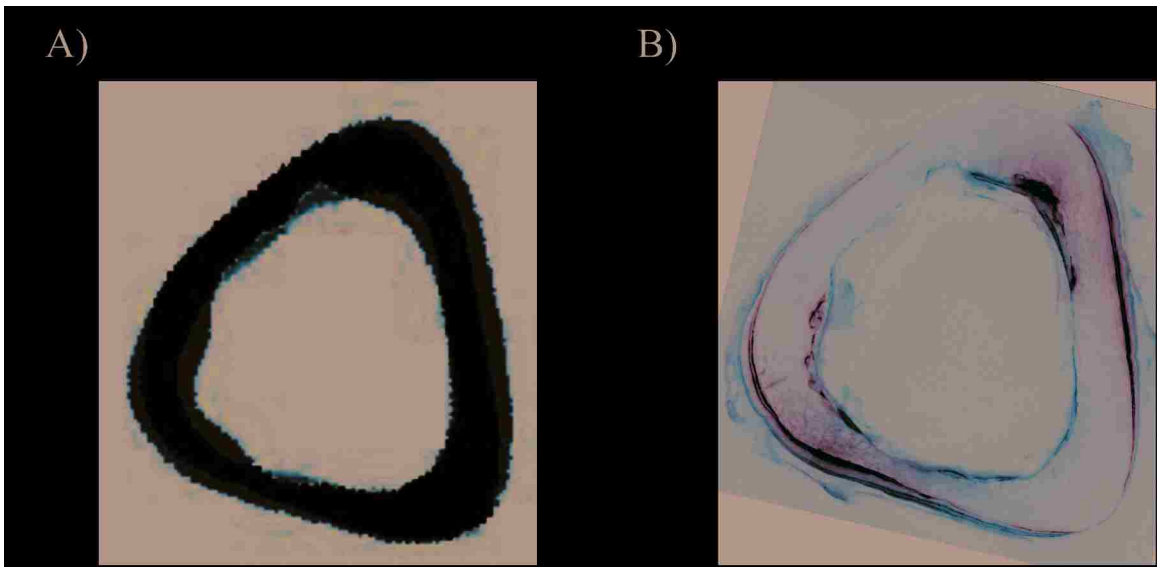

Figure 5.3: Comparison of Bone Adaptation Assayed With μCT Based Image Registration and Dynamic Histomorphometry
μCT image registration allowed for focal mapping of bone formation (A, orange) and bone resorption (A, red) occurring over 9 weeks of mechanical loading. The patterns of bone formation were highly similar to that observed in the histomorphometric section taken from the same location (B, Calcein-green and Alizarin-red), suggesting that image registration accuracy was sufficient to detect focal alterations in this model.

References

1. Motley RJ, Clements D, Evans WD, Crawley EO, Evans C, Rhodes J, and Compston JE. 1993. A four-year longitudinal study of bone loss in patients with inflammatory bowel disease. Bone Miner **23**(2): 95-104.
2. Shaw SR, Zernicke RF, Vailas AC, DeLuna D, Thomason DB, and Baldwin KM. 1987. Mechanical, morphological and biochemical adaptations of bone and muscle to hindlimb suspension and exercise. J Biomech **20**(3): 225-34.
3. Gough AK, Lilley J, Eyre S, Holder RL, and Emery P. 1994. Generalised bone loss in patients with early rheumatoid arthritis. Lancet **344**(8914): 23-7.
4. Lambers FM, Koch K, Kuhn G, Ruffoni D, Weigt C, Schulte FA, and Muller R. 2013. Trabecular bone adapts to long-term cyclic loading by increasing stiffness and normalization of dynamic morphometric rates. Bone **55**(2): 325-34.
5. J. W. 1892. *Das Gesetz der Transformation der Knochen*, ed. A Hirschwald. Berlin.
6. Kannegaard PN, van der Mark S, Eiken P, and Abrahamsen B. 2010. Excess mortality in men compared with women following a hip fracture. National analysis of comedications, comorbidity and survival. Age Ageing **39**(2): 203-9.
7. Haentjens P, Magaziner J, Colon-Emeric CS, Vanderschueren D, Milisen K, Velkeniers B, and Boonen S. 2010. Meta-analysis: excess mortality after hip fracture among older women and men. Ann Intern Med **152**(6): 380-90.
8. Heaney RP, Recker RR, and Saville PD. 1978. Menopausal changes in bone remodeling. J Lab Clin Med **92**(6): 964-70.
9. Fink HA, Ewing SK, Ensrud KE, Barrett-Connor E, Taylor BC, Cauley JA, and Orwoll ES. 2006. Association of testosterone and estradiol deficiency with osteoporosis and rapid bone loss in older men. J Clin Endocrinol Metab **91**(10): 3908-15.
10. Silverberg SJ, Shane E, de la Cruz L, Dempster DW, Feldman F, Seldin D, Jacobs TP, Siris ES, Cafferty M, Parisien MV, and et al. 1989. Skeletal disease in primary hyperparathyroidism. J Bone Miner Res **4**(3): 283-91.
11. Cao JJ, Gregoire BR, and Gao H. 2009. High-fat diet decreases cancellous bone mass but has no effect on cortical bone mass in the tibia in mice. Bone **44**(6): 1097-104.
12. Barrett-Connor E, Laughlin GA, Li H, Nielson CM, Wang PY, Dam TT, Cauley JA, Ensrud KE, Stefanick ML, Lau E, Hoffman AR, and Orwoll ES. 2012. The association of concurrent vitamin D and sex hormone deficiency with bone loss and fracture risk in older men: the osteoporotic fractures in men (MrOS) study. J Bone Miner Res **27**(11): 2306-13.
13. Ward KD and Klesges RC. 2001. A meta-analysis of the effects of cigarette smoking on bone mineral density. Calcif Tissue Int **68**(5): 259-70.
14. Haugeberg G, Conaghan PG, Quinn M, and Emery P. 2009. Bone loss in patients with active early rheumatoid arthritis: infliximab and methotrexate compared with methotrexate treatment alone. Explorative analysis from a 12-month randomised, double-blind, placebo-controlled study. Ann Rheum Dis **68**(12): 1898-901.
15. Romas E and Gillespie MT. 2006. Inflammation-induced bone loss: can it be prevented? Rheum Dis Clin North Am **32**(4): 759-73.
16. Yoshinaga Y, Ukai T, Abe Y, and Hara Y. 2007. Expression of receptor activator of nuclear factor kappa B ligand relates to inflammatory bone resorption, with or without occlusal trauma, in rats. J Periodontal Res **42**(5): 402-9.

17. Hattersley G, Owens J, Flanagan AM, and Chambers TJ. 1991. Macrophage colony stimulating factor (M-CSF) is essential for osteoclast formation in vitro. Biochem Biophys Res Commun **177**(1): 526-31.
18. Woo KM, Kim HM, and Ko JS. 2002. Macrophage colony-stimulating factor promotes the survival of osteoclast precursors by up-regulating Bcl-X(L). Exp Mol Med **34**(5): 340-6.
19. Biskobing DM, Fan X, and Rubin J. 1995. Characterization of MCSF-induced proliferation and subsequent osteoclast formation in murine marrow culture. J Bone Miner Res **10**(7): 1025-32.
20. Yagi M, Miyamoto T, Sawatani Y, Iwamoto K, Hosogane N, Fujita N, Morita K, Ninomiya K, Suzuki T, Miyamoto K, Oike Y, Takeya M, Toyama Y, and Suda T. 2005. DC-STAMP is essential for cell-cell fusion in osteoclasts and foreign body giant cells. J Exp Med **202**(3): 345-51.
21. Mensah KA, Ritchlin CT, and Schwarz EM. 2010. RANKL induces heterogeneous DC-STAMP(lo) and DC-STAMP(hi) osteoclast precursors of which the DC-STAMP(lo) precursors are the master fusogens. J Cell Physiol **223**(1): 76-83.
22. Anderson DM, Maraskovsky E, Billingsley WL, Dougall WC, Tometsko ME, Roux ER, Teepe MC, DuBose RF, Cosman D, and Galibert L. 1997. A homologue of the TNF receptor and its ligand enhance T-cell growth and dendritic-cell function. Nature **390**(6656): 175-9.
23. Wong BR, Rho J, Arron J, Robinson E, Orlinick J, Chao M, Kalachikov S, Cayani E, Bartlett FS, 3rd, Frankel WN, Lee SY, and Choi Y. 1997. TRANCE is a novel ligand of the tumor necrosis factor receptor family that activates c-Jun N-terminal kinase in T cells. J Biol Chem **272**(40): 25190-4.
24. Kong YY, Feige U, Sarosi I, Bolon B, Tafuri A, Morony S, Capparelli C, Li J, Elliott R, McCabe S, Wong T, Campagnuolo G, Moran E, Bogoch ER, Van G, Nguyen LT, Ohashi PS, Lacey DL, Fish E, Boyle WJ, and Penninger JM. 1999. Activated T cells regulate bone loss and joint destruction in adjuvant arthritis through osteoprotegerin ligand. Nature **402**(6759): 304-9.
25. Lacey DL, Timms E, Tan HL, Kelley MJ, Dunstan CR, Burgess T, Elliott R, Colombero A, Elliott G, Scully S, Hsu H, Sullivan J, Hawkins N, Davy E, Capparelli C, Eli A, Qian YX, Kaufman S, Sarosi I, Shalhoub V, Senaldi G, Guo J, Delaney J, and Boyle WJ. 1998. Osteoprotegerin ligand is a cytokine that regulates osteoclast differentiation and activation. Cell **93**(2): 165-76.
26. Takayanagi H, Kim S, Matsuo K, Suzuki H, Suzuki T, Sato K, Yokochi T, Oda H, Nakamura K, Ida N, Wagner EF, and Taniguchi T. 2002. RANKL maintains bone homeostasis through c-Fos-dependent induction of interferon-beta. Nature **416**(6882): 744-9.
27. Yasuda H, Shima N, Nakagawa N, Yamaguchi K, Kinosaki M, Mochizuki S, Tomoyasu A, Yano K, Goto M, Murakami A, Tsuda E, Morinaga T, Higashio K, Udagawa N, Takahashi N, and Suda T. 1998. Osteoclast differentiation factor is a ligand for osteoprotegerin/osteoclastogenesis-inhibitory factor and is identical to TRANCE/RANKL. Proc Natl Acad Sci U S A **95**(7): 3597-602.
28. Hofbauer LC and Schoppet M. 2004. Clinical implications of the osteoprotegerin/RANKL/RANK system for bone and vascular diseases. JAMA **292**(4): 490-5.

29. Cao J, Venton L, Sakata T, and Halloran BP. 2003. Expression of RANKL and OPG correlates with age-related bone loss in male C57BL/6 mice. J Bone Miner Res **18**(2): 270-7.
30. Nakashima T, Kobayashi Y, Yamasaki S, Kawakami A, Eguchi K, Sasaki H, and Sakai H. 2000. Protein expression and functional difference of membrane-bound and soluble receptor activator of NF-kappaB ligand: modulation of the expression by osteotropic factors and cytokines. Biochem Biophys Res Commun **275**(3): 768-75.
31. Brandstrom H, Bjorkman T, and Ljunggren O. 2001. Regulation of osteoprotegerin secretion from primary cultures of human bone marrow stromal cells. Biochem Biophys Res Commun **280**(3): 831-5.
32. Kong YY, Yoshida H, Sarosi I, Tan HL, Timms E, Capparelli C, Morony S, Oliveira-dos-Santos AJ, Van G, Itie A, Khoo W, Wakeham A, Dunstan CR, Lacey DL, Mak TW, Boyle WJ, and Penninger JM. 1999. OPGL is a key regulator of osteoclastogenesis, lymphocyte development and lymph-node organogenesis. Nature **397**(6717): 315-23.
33. Kim N, Odgren PR, Kim DK, Marks SC, Jr., and Choi Y. 2000. Diverse roles of the tumor necrosis factor family member TRANCE in skeletal physiology revealed by TRANCE deficiency and partial rescue by a lymphocyte-expressed TRANCE transgene. Proc Natl Acad Sci U S A **97**(20): 10905-10.
34. Bucay N, Sarosi I, Dunstan CR, Morony S, Tarpley J, Capparelli C, Scully S, Tan HL, Xu W, Lacey DL, Boyle WJ, and Simonet WS. 1998. osteoprotegerin-deficient mice develop early onset osteoporosis and arterial calcification. Genes Dev **12**(9): 1260-8.
35. Mizuno A, Amizuka N, Irie K, Murakami A, Fujise N, Kanno T, Sato Y, Nakagawa N, Yasuda H, Mochizuki S, Gomibuchi T, Yano K, Shima N, Washida N, Tsuda E, Morinaga T, Higashio K, and Ozawa H. 1998. Severe osteoporosis in mice lacking osteoclastogenesis inhibitory factor/osteoprotegerin. Biochem Biophys Res Commun **247**(3): 610-5.
36. Miyamoto T, Arai F, Ohneda O, Takagi K, Anderson DM, and Suda T. 2000. An adherent condition is required for formation of multinuclear osteoclasts in the presence of macrophage colony-stimulating factor and receptor activator of nuclear factor kappa B ligand. Blood **96**(13): 4335-43.
37. Hikita A, Yana I, Wakeyama H, Nakamura M, Kadono Y, Oshima Y, Nakamura K, Seiki M, and Tanaka S. 2006. Negative regulation of osteoclastogenesis by ectodomain shedding of receptor activator of NF-kappaB ligand. J Biol Chem **281**(48): 36846-55.
38. Lam J, Takeshita S, Barker JE, Kanagawa O, Ross FP, and Teitelbaum SL. 2000. TNF-alpha induces osteoclastogenesis by direct stimulation of macrophages exposed to permissive levels of RANK ligand. J Clin Invest **106**(12): 1481-8.
39. Wei S, Kitaura H, Zhou P, Ross FP, and Teitelbaum SL. 2005. IL-1 mediates TNF-induced osteoclastogenesis. J Clin Invest **115**(2): 282-90.
40. Hughes FJ and Howells GL. 1993. Interleukin-6 inhibits bone formation in vitro. Bone Miner **21**(1): 21-8.
41. Hayashida K, Ochi T, Fujimoto M, Owaki H, Shimaoka Y, Ono K, and Matsumoto K. 1992. Bone marrow changes in adjuvant-induced and collagen-induced arthritis. Interleukin-1 and interleukin-6 activity and abnormal myelopoiesis. Arthritis Rheum **35**(2): 241-5.

42. Cenci S, Weitzmann MN, Roggia C, Namba N, Novack D, Woodring J, and Pacifici R. 2000. Estrogen deficiency induces bone loss by enhancing T-cell production of TNF-alpha. J Clin Invest **106**(10): 1229-37.
43. Roggia C, Gao Y, Cenci S, Weitzmann MN, Toraldo G, Isaia G, and Pacifici R. 2001. Up-regulation of TNF-producing T cells in the bone marrow: a key mechanism by which estrogen deficiency induces bone loss in vivo. Proc Natl Acad Sci U S A **98**(24): 13960-5.
44. Morey ER. 1979. Spaceflight and Bone Turnover - Correlation with a New Rat Model of Weightlessness. Bioscience **29**(3): 168-172.
45. Colleran PN, Wilkerson MK, Bloomfield SA, Suva LJ, Turner RT, and Delp MD. 2000. Alterations in skeletal perfusion with simulated microgravity: a possible mechanism for bone remodeling. J Appl Physiol (1985) **89**(3): 1046-54.
46. Chapes SK, Mastro AM, Sonnenfeld G, and Berry WD. 1993. Antiorthostatic suspension as a model for the effects of spaceflight on the immune system. J Leukoc Biol **54**(3): 227-35.
47. Simske SJ, Guerra KM, Greenberg AR, and Luttges MW. 1992. The physical and mechanical effects of suspension-induced osteopenia on mouse long bones. J Biomech **25**(5): 489-99.
48. Warner SE, Sanford DA, Becker BA, Bain SD, Srinivasan S, and Gross TS. 2006. Botox induced muscle paralysis rapidly degrades bone. Bone **38**(2): 257-64.
49. Poliachik SL, Bain SD, Threet D, Huber P, and Gross TS. 2010. Transient muscle paralysis disrupts bone homeostasis by rapid degradation of bone morphology. Bone **46**(1): 18-23.
50. Grimston SK, Silva MJ, and Civitelli R. 2007. Bone loss after temporarily induced muscle paralysis by Botox is not fully recovered after 12 weeks. Ann N Y Acad Sci **1116**: 444-60.
51. Blouin S, Gallois Y, Moreau MF, Basle MF, and Chappard D. 2007. Disuse and orchidectomy have additional effects on bone loss in the aged male rat. Osteoporos Int **18**(1): 85-92.
52. Rauch F and Hamdy R. 2006. Effect of a single botulinum toxin injection on bone development in growing rabbits. J Musculoskelet Neuronal Interact **6**(3): 264-8.
53. Warden SJ, Galley MR, Richard JS, George LA, Dirks RC, Guildenbecher EA, Judd AM, Robling AG, and Fuchs RK. 2013. Reduced gravitational loading does not account for the skeletal effect of botulinum toxin-induced muscle inhibition suggesting a direct effect of muscle on bone. Bone **54**(1): 98-105.
54. Bloomfield SA, Allen MR, Hogan HA, and Delp MD. 2002. Site- and compartment-specific changes in bone with hindlimb unloading in mature adult rats. Bone **31**(1): 149-57.
55. Jamsa T, Koivukangas A, Ryhanen J, Jalovaara P, and Tuukkanen J. 1999. Femoral neck is a sensitive indicator of bone loss in immobilized hind limb of mouse. J Bone Miner Res **14**(10): 1708-13.
56. Damrongrungruang T, Kuroda S, Kondo H, Aoki K, Ohya K, and Kasugai S. 2004. A simple murine model for immobilization osteopenia. Clin Orthop Relat Res (425): 244-51.

57. Aliprantis AO, Stolina M, Kostenuik PJ, Poliachik SL, Warner SE, Bain SD, and Gross TS. 2012. Transient muscle paralysis degrades bone via rapid osteoclastogenesis. FASEB J **26**(3): 1110-8.
58. Bain SD, Poliachik SL, Threet D, Srinivasan S, and Gross TS. 2010. Trabecular bone homeostasis is modulated by neuromuscular proprioception. J Bone Min Res **25**(S1): SU106.
59. Bouxsein ML, Boyd SK, Christiansen BA, Guldberg RE, Jepsen KJ, and Muller R. 2010. Guidelines for assessment of bone microstructure in rodents using micro-computed tomography. J Bone Miner Res **25**(7): 1468-86.
60. Ausk BJ, Huber P, Poliachik SL, Bain SD, Srinivasan S, and Gross TS. 2012. Cortical bone resorption following muscle paralysis is spatially heterogeneous. Bone **50**(1): 14-22.
61. Ausk BJ, Huber P, Srinivasan S, Bain SD, Kwon RY, McNamara EA, Poliachik SL, Sybrowsky CL, and Gross TS. 2013. Metaphyseal and diaphyseal bone loss in the tibia following transient muscle paralysis are spatiotemporally distinct resorption events. Bone **57**(2): 413-422.
62. Amblard D, Lafage-Proust MH, Laib A, Thomas T, Ruegsegger P, Alexandre C, and Vico L. 2003. Tail suspension induces bone loss in skeletally mature mice in the C57BL/6J strain but not in the C3H/HeJ strain. J Bone Miner Res **18**(3): 561-9.
63. Gross TS, Damji AA, Judex S, Bray RC, and Zernicke RF. 1999. Bone hyperemia precedes disuse-induced intracortical bone resorption. J Appl Physiol **86**(1): 230-5.
64. Judex S, Garman R, Squire M, Busa B, Donahue LR, and Rubin C. 2004. Genetically linked site-specificity of disuse osteoporosis. J Bone Miner Res **19**(4): 607-13.
65. Marenzana M, De Souza RL, and Chenu C. 2007. Blockade of beta-adrenergic signaling does not influence the bone mechano-adaptive response in mice. Bone **41**(2): 206-15.
66. Robling AG, Niziolek PJ, Baldridge LA, Condon KW, Allen MR, Alam I, Mantila SM, Gluhak-Heinrich J, Bellido TM, Harris SE, and Turner CH. 2008. Mechanical stimulation of bone in vivo reduces osteocyte expression of Sost/sclerostin. J Biol Chem **283**(9): 5866-75.
67. Sugiyama T, Price JS, and Lanyon LE. Functional adaptation to mechanical loading in both cortical and cancellous bone is controlled locally and is confined to the loaded bones. Bone **46**(2): 314-21.
68. Waarsing JH, Day JS, van der Linden JC, Ederveen AG, Spanjers C, De Clerck N, Sasov A, Verhaar JA, and Weinans H. 2004. Detecting and tracking local changes in the tibiae of individual rats: a novel method to analyse longitudinal in vivo micro-CT data. Bone **34**(1): 163-9.
69. Waarsing JH, Day JS, Verhaar JA, Ederveen AG, and Weinans H. 2006. Bone loss dynamics result in trabecular alignment in aging and ovariectomized rats. J Orthop Res **24**(5): 926-35.
70. Gross TS and Rubin CT. 1995. Uniformity of resorptive bone loss induced by disuse. J Orthop Res **13**(5): 708-14.
71. Rüegsegger P, Koller B, and Müller R. 1996. A microtomographic system for the nondestructive evaluation of bone architecture. Calcif Tissue Int **58**(1): 24-9.
72. Stenstrom M, Olander B, Carlsson CA, Carlsson GA, Lehto-Axtelius D, and Hakanson R. 1998. The use of computed microtomography to monitor morphological changes in small animals. Appl Radiat Isot **49**(5-6): 565-70.

73. Boyd SK, Moser S, Kuhn M, Klinck RJ, Krauze PL, Müller R, and Gasser JA. 2006. Evaluation of three-dimensional image registration methodologies for in vivo micro-computed tomography. Ann Biomed Eng **34**(10): 1587-99.
74. Brouwers JE, Lambers FM, van Rietbergen B, Ito K, and Huiskes R. 2009. Comparison of bone loss induced by ovariectomy and neurectomy in rats analyzed by in vivo micro-CT. J Orthop Res **27**(11): 1521-7.
75. David V, Laroche N, Boudignon B, Lafage-Proust MH, Alexandre C, Ruegsegger P, and Vico L. 2003. Noninvasive in vivo monitoring of bone architecture alterations in hindlimb-unloaded female rats using novel three-dimensional microcomputed tomography. J Bone Miner Res **18**(9): 1622-31.
76. Warner SE, Srinivasan S, Kostenuik PJ, and Gross TS. 2006. RANKL inhibition prevents the loss of bone volume and bone strength caused by Botox induced muscle paralysis. 52nd Trans Orthop Res Soc. **31**: 189.
77. Morey-Holton ER and Globus RK. 2002. Hindlimb unloading rodent model: technical aspects. J Appl Physiol **92**(4): 1367-77.
78. Gross TS, Poliachik SL, Prasad J, and Bain SD. 2010. The effect of muscle dysfunction on bone mass and morphology. J Musculoskelet Neuronal Interact **10**(1): 25-34.
79. Stauber M and Muller R. 2008. Micro-computed tomography: a method for the non-destructive evaluation of the three-dimensional structure of biological specimens. Methods Mol Biol **455**: 273-92.
80. Sutton MA, Cheng MQ, Peters WH, Chao YJ, and Mcneill SR. 1986. Application of an Optimized Digital Correlation Method to Planar Deformation Analysis. Image and Vision Computing **4**(3): 143-150.
81. Verhulp E, van Rietbergen B, and Huiskes R. 2004. A three-dimensional digital image correlation technique for strain measurements in microstructures. Journal of Biomechanics **37**(9): 1313-1320.
82. Boutroy S, Bouxsein ML, Munoz F, and Delmas PD. 2005. In vivo assessment of trabecular bone microarchitecture by high-resolution peripheral quantitative computed tomography. J Clin Endocrinol Metab **90**(12): 6508-15.
83. Ausk BJ, Huber P, Srinivasan S, and Gross TS. 2007. Focal bone loss in mice with transient muscle paralysis. J Bone Min Res **22**(S1): S267.
84. Srinivasan S, Agans SC, King KA, Moy NY, Poliachik SL, and Gross TS. 2003. Enabling bone formation in the aged skeleton via rest-inserted mechanical loading. Bone **33**(6): 946-55.
85. Srinivasan S, Ausk BJ, Poliachik SL, Warner SE, Richardson TS, and Gross TS. 2007. Rest-inserted loading rapidly amplifies the response of bone to small increases in strain and load cycles. J Appl Physiol **102**(5): 1945-52.
86. Lang T, LeBlanc A, Evans H, Lu Y, Genant H, and Yu A. 2004. Cortical and trabecular bone mineral loss from the spine and hip in long-duration spaceflight. J Bone Miner Res **19**(6): 1006-12.
87. Bain SD and Rubin CT. 1990. Metabolic modulation of disuse osteopenia: endocrine-dependent site specificity of bone remodeling. J Bone Miner Res **5**(10): 1069-75.
88. Vico L, Collet P, Guignandon A, Lafage-Proust MH, Thomas T, Rehaillia M, and Alexandre C. 2000. Effects of long-term microgravity exposure on cancellous and cortical weight-bearing bones of cosmonauts. Lancet **355**(9215): 1607-11.

89. Nishiyama KK, Campbell GM, Klinck RJ, and Boyd SK. 2010. Reproducibility of bone micro-architecture measurements in rodents by in vivo micro-computed tomography is maximized with three-dimensional image registration. Bone **46**(1): 155-161.
90. Moustafa A, Sugiyama T, Saxon LK, Zaman G, Sunters A, Armstrong VJ, Javaheri B, Lanyon LE, and Price JS. 2009. The mouse fibula as a suitable bone for the study of functional adaptation to mechanical loading. Bone **44**(5): 930-5.
91. Jee WSS. 1989.The skeletal tissues, in Cell and Tissue Biology: A Textbook of Histology, L Weiss, Editor. Urban and Schwartzenberg: Baltimore. p. 211-259.
92. Frost HM. 1964. The laws of bone structure. The Henry Ford Hospital surgical monographs. Springfield, Ill.,: C.C. Thomas. xiii, 167 p.
93. Lee KC, Maxwell A, and Lanyon LE. 2002. Validation of a technique for studying functional adaptation of the mouse ulna in response to mechanical loading. Bone **31**(3): 407-12.
94. Klinck RJ, Campbell GM, and Boyd SK. 2008. Radiation effects on bone architecture in mice and rats resulting from in vivo micro-computed tomography scanning. Med Eng Phys **30**(7): 888-95.
95. Ausk BJ, Huber P, Srinivasan S, Bain SD, and Gross TS. 2011. Initiation of trabecular bone resorption following transient muscle paralysis is site specific. in *2011 Orthopaedic Research Society Annual Meeting*. Long Beach, CA: Abstract #2260.
96. Chamay A and Tschantz P. 1972. Mechanical influences in bone remodeling. Experimental research on Wolff's law. J Biomech **5**(2): 173-80.
97. Goodship AE, Lanyon LE, and McFie H. 1979. Functional adaptation of bone to increased stress. An experimental study. J Bone Joint Surg Am **61**(4): 539-46.
98. Frost HM. 1987. Bone "mass" and the "mechanostat": a proposal. Anat Rec **219**(1): 1-9.
99. Prasad J, Wiater BP, Nork SE, Bain SD, and Gross TS. 2010. Characterizing gait induced normal strains in a murine tibia cortical bone defect model. J Biomech **43**(14): 2765-70.
100. Frost HM. 1982. Mechanical determinants of bone modeling. Metab Bone Dis Relat Res **4**(4): 217-29.
101. Zeng QQ, Jee WS, Bigornia AE, King JG, Jr., D'Souza SM, Li XJ, Ma YF, and Wechter WJ. 1996. Time responses of cancellous and cortical bones to sciatic neurectomy in growing female rats. Bone **19**(1): 13-21.
102. Han ZH, Palnitkar S, Rao DS, Nelson D, and Parfitt AM. 1997. Effects of ethnicity and age or menopause on the remodeling and turnover of iliac bone: implications for mechanisms of bone loss. J Bone Miner Res **12**(4): 498-508.
103. Ahlborg HG, Johnell O, Turner CH, Rannevik G, and Karlsson MK. 2003. Bone loss and bone size after menopause. N Engl J Med **349**(4): 327-34.
104. Globus RK, Bikle DD, and Morey-Holton E. 1986. The temporal response of bone to unloading. Endocrinology **118**(2): 733-42.
105. Tuukkanen J, Wallmark B, Jalovaara P, Takala T, Sjogren S, and Vaananen K. 1991. Changes induced in growing rat bone by immobilization and remobilization. Bone **12**(2): 113-8.
106. Wronski TJ, Walsh CC, and Ignaszewski LA. 1986. Histologic evidence for osteopenia and increased bone turnover in ovariectomized rats. Bone **7**(2): 119-23.
107. Bloomfield SA. 1997. Changes in musculoskeletal structure and function with prolonged bed rest. Med Sci Sports Exerc **29**(2): 197-206.

108. Krolner B and Toft B. 1983. Vertebral bone loss: an unheeded side effect of therapeutic bed rest. Clin Sci (Lond) **64**(5): 537-40.
109. Szejnfeld VL, Monier-Faugere MC, Bognar BJ, Ferraz MB, and Malluche HH. 1997. Systemic osteopenia and mineralization defect in patients with ankylosing spondylitis. J Rheumatol **24**(4): 683-8.
110. Dinca M, Fries W, Luisetto G, Peccolo F, Bottega F, Leone L, Naccarato R, and Martin A. 1999. Evolution of osteopenia in inflammatory bowel disease. Am J Gastroenterol **94**(5): 1292-7.
111. Parfitt AM. 1984. Age-related structural changes in trabecular and cortical bone: cellular mechanisms and biomechanical consequences. Calcif Tissue Int **36 Suppl 1**: S123-8.
112. Mazess RB. 1982. On aging bone loss. Clin Orthop Relat Res (165): 239-52.
113. Meier DE, Orwoll ES, and Jones JM. 1984. Marked disparity between trabecular and cortical bone loss with age in healthy men. Measurement by vertebral computed tomography and radial photon absorptiometry. Ann Intern Med **101**(5): 605-12.
114. Hefferan TE, Evans GL, Lotinun S, Zhang M, Morey-Holton E, and Turner RT. 2003. Effect of gender on bone turnover in adult rats during simulated weightlessness. J Appl Physiol **95**(5): 1775-80.
115. Riggs BL, Melton Iii LJ, 3rd, Robb RA, Camp JJ, Atkinson EJ, Peterson JM, Rouleau PA, McCollough CH, Bouxsein ML, and Khosla S. 2004. Population-based study of age and sex differences in bone volumetric density, size, geometry, and structure at different skeletal sites. J Bone Miner Res **19**(12): 1945-54.
116. Schulte FA, Lambers FM, Kuhn G, and Muller R. 2011. In vivo micro-computed tomography allows direct three-dimensional quantification of both bone formation and bone resorption parameters using time-lapsed imaging. Bone **48**(3): 433-42.
117. Jaworski ZF and Lok E. 1972. The rate of osteoclastic bone erosion in Haversian remodeling sites of adult dog's rib. Calcif Tissue Res **10**(2): 103-12.
118. Parfitt AM. 1983.The physiologic and clinical significance of bone histomorphometric data., in Bone Histomorphometry: Techniques and Interpretations., RR Recker, Editor. CRC Press: Boca Raton, FL. p. 143-224.
119. Jiang SD, Shen C, Jiang LS, and Dai LY. 2007. Differences of bone mass and bone structure in osteopenic rat models caused by spinal cord injury and ovariectomy. Osteoporos Int **18**(6): 743-50.
120. Li W, Kezele I, Collins DL, Zijdenbos A, Keyak J, Kornak J, Koyama A, Saeed I, Leblanc A, Harris T, Lu Y, and Lang T. 2007. Voxel-based modeling and quantification of the proximal femur using inter-subject registration of quantitative CT images. Bone **41**(5): 888-95.
121. Li W, Sode M, Saeed I, and Lang T. 2006. Automated registration of hip and spine for longitudinal QCT studies: integration with 3D densitometric and structural analysis. Bone **38**(2): 273-9.
122. Brouwers JE, van Rietbergen B, Huiskes R, and Ito K. 2009. Effects of PTH treatment on tibial bone of ovariectomized rats assessed by in vivo micro-CT. Osteoporos Int **20**(11): 1823-35.
123. De Souza RL, Matsuura M, Eckstein F, Rawlinson SC, Lanyon LE, and Pitsillides AA. 2005. Non-invasive axial loading of mouse tibiae increases cortical bone formation and modifies trabecular organization: a new model to study cortical and cancellous compartments in a single loaded element. Bone **37**(6): 810-8.

124. Foldes J, Parfitt AM, Shih MS, Rao DS, and Kleerekoper M. 1991. Structural and geometric changes in iliac bone: relationship to normal aging and osteoporosis. J Bone Miner Res **6**(7): 759-66.
125. Zioupos P, Cook RB, and Hutchinson JR. 2008. Some basic relationships between density values in cancellous and cortical bone. J Biomech **41**(9): 1961-8.
126. Turner CH, Hsieh YF, Muller R, Bouxsein ML, Baylink DJ, Rosen CJ, Grynpas MD, Donahue LR, and Beamer WG. 2000. Genetic regulation of cortical and trabecular bone strength and microstructure in inbred strains of mice. J Bone Miner Res **15**(6): 1126-31.
127. Kilborn SH, Trudel G, and Uhthoff H. 2002. Review of growth plate closure compared with age at sexual maturity and lifespan in laboratory animals. Contemp Top Lab Anim Sci **41**(5): 21-6.
128. Lynch ME, Main RP, Xu Q, Walsh DJ, Schaffler MB, Wright TM, and van der Meulen MC. 2010. Cancellous bone adaptation to tibial compression is not sex dependent in growing mice. J Appl Physiol **109**(3): 685-91.
129. Takahashi N, Udagawa N, and Suda T. 1999. A new member of tumor necrosis factor ligand family, ODF/OPGL/TRANCE/RANKL, regulates osteoclast differentiation and function. Biochem Biophys Res Commun **256**(3): 449-55.
130. Collin-Osdoby P, Yu X, Zheng H, and Osdoby P. 2003. RANKL-mediated osteoclast formation from murine RAW 264.7 cells. Methods Mol Med **80**: 153-66.
131. Tinkler SM, Williams DM, and Johnson NW. 1981. Osteoclast formation in response to intraperitoneal injection of 1 alpha-hydroxycholecalciferol in mice. J Anat **133**(Pt 1): 91-7.
132. Grano M, Mori G, Minielli V, Barou O, Colucci S, Giannelli G, Alexandre C, Zallone AZ, and Vico L. 2002. Rat hindlimb unloading by tail suspension reduces osteoblast differentiation, induces IL-6 secretion, and increases bone resorption in ex vivo cultures. Calcif Tissue Int **70**(3): 176-85.
133. Weinreb M, Rodan GA, and Thompson DD. 1991. Depression of osteoblastic activity in immobilized limbs of suckling rats. J Bone Miner Res **6**(7): 725-31.
134. Grimston SK, Goldberg DB, Watkins M, Brodt MD, Silva MJ, and Civitelli R. 2011. Connexin43 deficiency reduces the sensitivity of cortical bone to the effects of muscle paralysis. J Bone Miner Res **26**(9): 2151-60.
135. Manske SL, Boyd SK, and Zernicke RF. 2010. Muscle and bone follow similar temporal patterns of recovery from muscle-induced disuse due to botulinum toxin injection. Bone **46**(1): 24-31.
136. Adamopoulos IE and Bowman EP. 2008. Immune regulation of bone loss by Th17 cells. Arthritis Res Ther **10**(5): 225.
137. Colburn NT, Zaal KJ, Wang F, and Tuan RS. 2009. A role for gamma/delta T cells in a mouse model of fracture healing. Arthritis Rheum **60**(6): 1694-703.
138. Yoshitake F, Itoh S, Narita H, Ishihara K, and Ebisu S. 2008. Interleukin-6 directly inhibits osteoclast differentiation by suppressing receptor activator of NF-kappaB signaling pathways. J Biol Chem **283**(17): 11535-40.
139. Buckland-Wright JC and Walker SR. 1987. Incidence and size of erosions in the wrist and hand of rheumatoid patients: a quantitative microfocal radiographic study. Ann Rheum Dis **46**(6): 463-7.

140. Roux C, Abitbol V, Chaussade S, Kolta S, Guillemant S, Dougados M, Amor B, and Couturier D. 1995. Bone loss in patients with inflammatory bowel disease: a prospective study. Osteoporos Int **5**(3): 156-60.
141. Dimai HP, Domej W, Leb G, and Lau KH. 2001. Bone loss in patients with untreated chronic obstructive pulmonary disease is mediated by an increase in bone resorption associated with hypercapnia. J Bone Miner Res **16**(11): 2132-41.
142. Cosman F, Nieves J, Komar L, Ferrer G, Herbert J, Formica C, Shen V, and Lindsay R. 1998. Fracture history and bone loss in patients with MS. Neurology **51**(4): 1161-5.
143. Kuratani T, Nagata K, Kukita T, Hotokebuchi T, Nakasima A, and Iijima T. 1998. Induction of abundant osteoclast-like multinucleated giant cells in adjuvant arthritic rats with accompanying disordered high bone turnover. Histol Histopathol **13**(3): 751-9.
144. Assuma R, Oates T, Cochran D, Amar S, and Graves DT. 1998. IL-1 and TNF antagonists inhibit the inflammatory response and bone loss in experimental periodontitis. J Immunol **160**(1): 403-9.
145. Josien R, Wong BR, Li HL, Steinman RM, and Choi Y. 1999. TRANCE, a TNF family member, is differentially expressed on T cell subsets and induces cytokine production in dendritic cells. J Immunol **162**(5): 2562-8.
146. Kawai T, Matsuyama T, Hosokawa Y, Makihira S, Seki M, Karimbux NY, Goncalves RB, Valverde P, Dibart S, Li YP, Miranda LA, Ernst CW, Izumi Y, and Taubman MA. 2006. B and T lymphocytes are the primary sources of RANKL in the bone resorptive lesion of periodontal disease. Am J Pathol **169**(3): 987-98.
147. Tunyogi-Csapo M, Kis-Toth K, Radacs M, Farkas B, Jacobs JJ, Finnegan A, Mikecz K, and Glant TT. 2008. Cytokine-controlled RANKL and osteoprotegerin expression by human and mouse synovial fibroblasts: fibroblast-mediated pathologic bone resorption. Arthritis Rheum **58**(8): 2397-408.
148. Hashizume M, Hayakawa N, and Mihara M. 2008. IL-6 trans-signalling directly induces RANKL on fibroblast-like synovial cells and is involved in RANKL induction by TNF-alpha and IL-17. Rheumatology (Oxford) **47**(11): 1635-40.
149. Charatcharoenwitthaya N, Khosla S, Atkinson EJ, McCready LK, and Riggs BL. 2007. Effect of blockade of TNF-alpha and interleukin-1 action on bone resorption in early postmenopausal women. J Bone Miner Res **22**(5): 724-9.
150. Saidenberg-Kermanac'h N, Corrado A, Lemeiter D, deVernejoul MC, Boissier MC, and Cohen-Solal ME. 2004. TNF-alpha antibodies and osteoprotegerin decrease systemic bone loss associated with inflammation through distinct mechanisms in collagen-induced arthritis. Bone **35**(5): 1200-7.
151. Worton LE, Gardiner EM, Bain SD, and Gross TS. 2011. Transient muscle paralysis increases the osteoclastogenic differentiation potential of marrow. in *Orthopaedic Research Society*. Long Beach, CA.
152. Lee SK, Gardner AE, Kalinowski JF, Jastrzebski SL, and Lorenzo JA. 2006. RANKL-stimulated osteoclast-like cell formation in vitro is partially dependent on endogenous interleukin-1 production. Bone **38**(5): 678-85.
153. Mombaerts P, Clarke AR, Rudnicki MA, Iacomini J, Itohara S, Lafaille JJ, Wang L, Ichikawa Y, Jaenisch R, Hooper ML, and et al. 1992. Mutations in T-cell antigen receptor genes alpha and beta block thymocyte development at different stages. Nature **360**(6401): 225-31.

154. Silver N, Cotroneo E, Proctor G, Osailan S, Paterson KL, and Carpenter GH. 2008. Selection of housekeeping genes for gene expression studies in the adult rat submandibular gland under normal, inflamed, atrophic and regenerative states. BMC Mol Biol **9**: 64.
155. Filler SG, Solis NV, Guo J, Doellgast G, Ruiz-Garcia A, and Pan WJ. 2007. Pharmacokinetics of murine p75-Fc fusion protein and MP6-XT22 anti-murine TNF-alpha mAb in mice. J Investig Dermatol Symp Proc **12**(1): 52-6.
156. Weinstein RS, Roberson PK, and Manolagas SC. 2009. Giant osteoclast formation and long-term oral bisphosphonate therapy. N Engl J Med **360**(1): 53-62.
157. Roodman GD and Windle JJ. 2005. Paget disease of bone. J Clin Invest **115**(2): 200-8.
158. Shishido-Hara Y, Kurata A, Fujiwara M, Itoh H, Imoto S, and Kamma H. 2010. Two cases of breast carcinoma with osteoclastic giant cells: are the osteoclastic giant cells pro-tumoural differentiation of macrophages? Diagn Pathol **5**: 55.
159. Escudero ND and Mandalunis PM. 2012. Influence of bisphosphonate treatment on medullary macrophages and osteoclasts: an experimental study. Bone Marrow Res **2012**: 526236.
160. Gilbert L, He X, Farmer P, Boden S, Kozlowski M, Rubin J, and Nanes MS. 2000. Inhibition of osteoblast differentiation by tumor necrosis factor-alpha. Endocrinology **141**(11): 3956-64.
161. Pedersen SJ, Chiowchanwisawakit P, Lambert RG, Ostergaard M, and Maksymowych WP. 2011. Resolution of inflammation following treatment of ankylosing spondylitis is associated with new bone formation. J Rheumatol **38**(7): 1349-54.
162. Hu YL, Kim HY, Kohno T, and Khare SD. 2007. Pharmacodynamic effects of the murine p75-Fc fusion protein in mice. J Investig Dermatol Symp Proc **12**(1): 50-1.
163. Fukuda T, Takeda S, Xu R, Ochi H, Sunamura S, Sato T, Shibata S, Yoshida Y, Gu Z, Kimura A, Ma C, Xu C, Bando W, Fujita K, Shinomiya K, Hirai T, Asou Y, Enomoto M, Okano H, Okawa A, and Itoh H. 2013. Sema3A regulates bone-mass accrual through sensory innervations. Nature **497**(7450): 490-3.
164. Bain SD, Rothenberg A, Poliachik SL, Ausk BJ, and Gross TS. 2011. Bone loss following peripheral nerve injury in mice is rapid and profound. Trans Ortho Res Soc **36**: 392.
165. Marchand-Libouban H, Le Drevo MA, and Chappard D. 2013. Disuse induced by Botulinum toxin affects the bone marrow expression profile of bone genes leading to a rapid bone loss. J Musculoskelet Neuronal Interact **13**(1): 27-36.
166. Muzylak M, Price JS, and Horton MA. 2006. Hypoxia induces giant osteoclast formation and extensive bone resorption in the cat. Calcif Tissue Int **79**(5): 301-9.
167. da Costa CE, Annels NE, Faaij CM, Forsyth RG, Hogendoorn PC, and Egeler RM. 2005. Presence of osteoclast-like multinucleated giant cells in the bone and nonostotic lesions of Langerhans cell histiocytosis. J Exp Med **201**(5): 687-93.
168. Hayer S, Steiner G, Gortz B, Reiter E, Tohidast-Akrad M, Amling M, Hoffmann O, Redlich K, Zwerina J, Skriner K, Hilberg F, Wagner EF, Smolen JS, and Schett G. 2005. CD44 is a determinant of inflammatory bone loss. J Exp Med **201**(6): 903-14.
169. Sanecka A, Ansems M, Prosser AC, Danielski K, Warner K, den Brok MH, Jansen BJ, Eleveld-Trancikova D, and Adema GJ. 2011. DC-STAMP knock-down deregulates cytokine production and T-cell stimulatory capacity of LPS-matured dendritic cells. BMC Immunol **12**: 57.

170. Miyamoto H, Suzuki T, Miyauchi Y, Iwasaki R, Kobayashi T, Sato Y, Miyamoto K, Hoshi H, Hashimoto K, Yoshida S, Hao W, Mori T, Kanagawa H, Katsuyama E, Fujie A, Morioka H, Matsumoto M, Chiba K, Takeya M, Toyama Y, and Miyamoto T. 2012. Osteoclast stimulatory transmembrane protein and dendritic cell-specific transmembrane protein cooperatively modulate cell-cell fusion to form osteoclasts and foreign body giant cells. J Bone Miner Res **27**(6): 1289-97.
171. Moreno JL, Mikhailenko I, Tondravi MM, and Keegan AD. 2007. IL-4 promotes the formation of multinucleated giant cells from macrophage precursors by a STAT6-dependent, homotypic mechanism: contribution of E-cadherin. J Leukoc Biol **82**(6): 1542-53.
172. Ehrlich LA and Roodman GD. 2005. The role of immune cells and inflammatory cytokines in Paget's disease and multiple myeloma. Immunol Rev **208**: 252-66.
173. McManus S and Roux S. 2012. The adaptor protein p62/SQSTM1 in osteoclast signaling pathways. J Mol Signal **7**: 1.
174. Chamoux E, Couture J, Bisson M, Morissette J, Brown JP, and Roux S. 2009. The p62 P392L mutation linked to Paget's disease induces activation of human osteoclasts. Mol Endocrinol **23**(10): 1668-80.
175. Roodman GD, Kurihara N, Ohsaki Y, Kukita A, Hosking D, Demulder A, Smith JF, and Singer FR. 1992. Interleukin 6. A potential autocrine/paracrine factor in Paget's disease of bone. J Clin Invest **89**(1): 46-52.
176. Kurihara N, Hiruma Y, Zhou H, Subler MA, Dempster DW, Singer FR, Reddy SV, Gruber HE, Windle JJ, and Roodman GD. 2007. Mutation of the sequestosome 1 (p62) gene increases osteoclastogenesis but does not induce Paget disease. J Clin Invest **117**(1): 133-42.
177. Tanabe F, Yone K, Kawabata N, Sakakima H, Matsuda F, Ishidou Y, Maeda S, Abematsu M, Komiya S, and Setoguchi T. 2011. Accumulation of p62 in degenerated spinal cord under chronic mechanical compression: functional analysis of p62 and autophagy in hypoxic neuronal cells. Autophagy **7**(12): 1462-71.
178. Kuusisto E, Suuronen T, and Salminen A. 2001. Ubiquitin-binding protein p62 expression is induced during apoptosis and proteasomal inhibition in neuronal cells. Biochem Biophys Res Commun **280**(1): 223-8.
179. Bjorkoy G, Lamark T, Brech A, Outzen H, Perander M, Overvatn A, Stenmark H, and Johansen T. 2005. p62/SQSTM1 forms protein aggregates degraded by autophagy and has a protective effect on huntingtin-induced cell death. J Cell Biol **171**(4): 603-14.
180. Paine MG, Babu JR, Seibenhener ML, and Wooten MW. 2005. Evidence for p62 aggregate formation: role in cell survival. FEBS Lett **579**(22): 5029-34.
181. Vailas AC, Deluna DM, Lewis LL, Curwin SL, Roy RR, and Alford EK. 1988. Adaptation of bone and tendon to prolonged hindlimb suspension in rats. J Appl Physiol (1985) **65**(1): 373-6.
182. Schiessl H, Frost HM, and Jee WS. 1998. Estrogen and bone-muscle strength and mass relationships. Bone **22**(1): 1-6.
183. Brotto L, Silswal N, Touchberry C, Parelkar N, Craig R, Hall T, Loghry M, Shen J, Qu CK, Bonewald L, Johnson M, Wacker M, Andresen J, and Brotto M. 2010. Evidence for pathophysiological crosstalk between bones, cardiac, skeletal and smooth muscles. Faseb Journal **24**.

184. Jahn K, Lara-Castillo N, Brotto L, Mo CL, Johnson ML, Brotto M, and Bonewald LF. 2012. Skeletal muscle secreted factors prevent glucocorticoid-induced osteocyte apoptosis through activation of beta-catenin. Eur Cell Mater **24**: 197-209; discussion 209-10.
185. Qin W, Sun L, Cao J, Peng Y, Collier L, Wu Y, Creasey G, Li J, Qin Y, Jarvis J, Bauman WA, Zaidi M, and Cardozo C. 2013. The central nervous system (CNS)-independent anti-bone-resorptive activity of muscle contraction and the underlying molecular and cellular signatures. J Biol Chem **288**(19): 13511-21.
186. Bonewald LF. 2011. The amazing osteocyte. J Bone Miner Res **26**(2): 229-38.
187. Kusu N, Laurikkala J, Imanishi M, Usui H, Konishi M, Miyake A, Thesleff I, and Itoh N. 2003. Sclerostin is a novel secreted osteoclast-derived bone morphogenetic protein antagonist with unique ligand specificity. J Biol Chem **278**(26): 24113-7.
188. Nakashima T, Hayashi M, Fukunaga T, Kurata K, Oh-Hora M, Feng JQ, Bonewald LF, Kodama T, Wutz A, Wagner EF, Penninger JM, and Takayanagi H. 2011. Evidence for osteocyte regulation of bone homeostasis through RANKL expression. Nat Med **17**(10): 1231-4.
189. Xiong J, Onal M, Jilka RL, Weinstein RS, Manolagas SC, and O'Brien CA. 2011. Matrix-embedded cells control osteoclast formation. Nat Med **17**(10): 1235-41.
190. Aguirre JI, Plotkin LI, Stewart SA, Weinstein RS, Parfitt AM, Manolagas SC, and Bellido T. 2006. Osteocyte apoptosis is induced by weightlessness in mice and precedes osteoclast recruitment and bone loss. J Bone Miner Res **21**(4): 605-15.
191. Verborgt O, Gibson GJ, and Schaffler MB. 2000. Loss of osteocyte integrity in association with microdamage and bone remodeling after fatigue in vivo. J Bone Miner Res **15**(1): 60-7.
192. Tatsumi S, Ishii K, Amizuka N, Li M, Kobayashi T, Kohno K, Ito M, Takeshita S, and Ikeda K. 2007. Targeted ablation of osteocytes induces osteoporosis with defective mechanotransduction. Cell Metab **5**(6): 464-75.
193. Rementer CW, Wu M, Ausk BJ, Gross TS, and Giachelli CM. 2013. Developing models of ectopic calcification for testing an osteoclast cell therapy. in *Biomedical Engineering Society Annual Meeting*. Seattle, WA.
194. Fan X, Biskobing DM, Bain S, and Rubin J. 1996. Ketoconazole and phorbol myristate acetate regulate osteoclast precursor fusion in primary murine marrow culture. J Bone Miner Res **11**(9): 1274-80.
195. Anderson JE and Blaschke TF. 1986. Ketoconazole inhibits cyclosporine metabolism in vivo in mice. J Pharmacol Exp Ther **236**(3): 671-4.
196. Srinivasan S, Ausk BJ, Prasad J, Threet D, Bain SD, Richardson TS, and Gross TS. 2010. Rescuing loading induced bone formation at senescence. PLoS Comput Biol **6**(9).
197. Hankenson KD, Ausk BJ, Bain SD, Bornstein P, Gross TS, and Srinivasan S. 2006. Mice lacking thrombospondin 2 show an atypical pattern of endocortical and periosteal bone formation in response to mechanical loading. Bone **38**(3): 310-6.
198. Kotha SP, Hsieh YF, Strigel RM, Muller R, and Silva MJ. 2004. Experimental and finite element analysis of the rat ulnar loading model-correlations between strain and bone formation following fatigue loading. J Biomech **37**(4): 541-8.
199. Gross TS, Srinivasan S, Liu CC, Clemens TL, and Bain SD. 2002. Noninvasive loading of the murine tibia: an in vivo model for the study of mechanotransduction. J Bone Miner Res **17**(3): 493-501.